January 2013

Reconfigurable Low Profile Antennas Using Tunable High Impedance Surfaces

David Cure
University of South Florida, dcure@mail.usf.edu

Reconfigurable Low Profile Antennas Using Tunable High Impedance Surfaces

by

David Cure

A dissertation submitted in partial fulfillment
of the requirements for the degree of
Doctor of Philosophy
Department of Electrical Engineering
College of Engineering
University of South Florida

Major Professor: Thomas M. Weller, Ph.D.
Félix A. Miranda, Ph.D.
Gokhan Mumcu, Ph.D.
Stephen Saddow, Ph.D.
Nathan Crane, Ph.D.

Date of Approval:
June 25, 2013

Keywords: Frequency selective surface (FSS), barium strontium titanate, flexible antennas, liquid crystal polymer (LCP), polydimethylsiloxane (PDMS)

DEDICATION

To Jade, my favorite monosyllable

to thank to the three ladies of my life, my mother Arinda for her endless love and dedication, and my wife Luz and beloved daughter Jade for educating and teaching me to be a better person every day.

TABLE OF CONTENTS

LIST OF TABLES

LIST OF FIGURES

ABSTRACT

This dissertation shows a detailed investigation on reconfigurable low profile antennas using tunable high impedance surfaces (HIS). The specific class of HIS used in this dissertation is called a frequency selective surface (FSS). This type of periodic structure is fabricated to create artificial magnetic conductors (AMCs) that exhibit properties similar to perfect magnetic conductors (PMCs). The antennas are intended for radiometric sensing applications in the biomedical field. For the particular sensing application of interest in this dissertation, the performance of the antenna sub-system is the most critical aspect of the radiometer design where characteristics such as small size, light weight, conformability, simple integration, adjustment in response to adverse environmental loading, and the ability to block external radio frequency interference to maximize the detection sensitivity are desirable.

The antenna designs in this dissertation are based on broadband dipole antennas over a tunable FSS to extend the usable frequency range. The main features of these antennas are the use of an FSS that does not include via connections to ground, their low profile and potentially conformal nature, high front-to-back radiation pattern ratio, and the ability to dynamically adjust the center frequency. The reduction of interlayer wiring on the tunable FSS minimizes the fabrication complexity and facilitates the use of flexible substrates.

This dissertation aims to advance the state of the art in low profile tunable planar antennas. It shows a qualitative comparison between antennas backed with different unit cell geometries. It demonstrates the feasibility to use either semiconductor or ferroelectric thin film varactor-based tunable FSS to allow adjustment in the antenna frequency in response to

environment loading in the near-field. Additionally, it illustrates how the coupling between antenna and HIS, and the impact of the varactor losses affect the antenna performance and it shows solutions to compensate these adverse effects. Novel hybrid manufacturing approaches to achieve flexibility on electrically thick antennas that could be transitioned to thin-film microelectronics are also presented.

The semiconductor and ferroelectric varactor-based tunable low profile antennas demonstrated tunability from 2.2 GHz to 2.65 GHz with instantaneous bandwidths greater than 50 MHz within the tuning range. The antennas had maximum thicknesses of $\lambda/45$ at the central frequency and front to back-lobe radiation ratios of approximately 15dB. They also showed impedance match improvement in the presence of a Human Core Model (HCM) phantom at close proximity distances of the order of 10-20 mm. In addition, the use of thin film ferroelectric Barium Strontium Titanate (BST) varactors in the FSS layer enabled an antenna that had smaller size, lower cost and less weight compared to the commercially available options.

The challenging problems of fabricating robust flexible antennas are also addressed and novel solutions are proposed. Two different types of flexible antennas were designed and built. A series of flexible microstrip antennas with slotted grounds which demonstrated to be robust and have 42% less mass than typically used technologies (e.g., microstrip antennas fabricated on Rogers® RT6010, RT/duroid® 5880, etc.); and flexible ferroelectric based tunable low profile antennas that showed tunability from 2.42 GHz to 2.66 GHz using overlapping metallic plates instead of a continuous ground plane. The bending test results demonstrated that, by placing cuts on the ground plane or using overlapping metallic layers that resemble fish scales, it was possible to create highly conductive surfaces that were extremely flexible even when attached to other

solid materials. These new approaches were used to overcome limitations commonly encountered in the design of antennas that are intended for use on non-flat surfaces.

The material presented in this dissertation represents the first investigation of reconfigurable low profile antennas using tunable high impedance surfaces where the desired electromagnetic performance as well as additional relevant features such as robustness, low weight, low cost and low complexity were demonstrated.

.

CHAPTER 1: INTRODUCTION

1.1. Overview

This dissertation presents a detailed investigation of reconfigurable low profile antennas using tunable high impedance surfaces (HIS). The antennas are intended for biomedical applications in which they may be worn comfortably by patients for extended periods of time. Accordingly, features such as robustness, light weight, and the ability to conform to non-planar surfaces are highly desirable. Other important requirements of the antenna design are the ability to adjust the frequency and impedance matching to compensate for the variable nature of the interface between the sensor and subject under test as well as the ability to suppress external radio frequency interference to maximize the detection sensitivity. Typically used approaches, based on microstrip patch elements on relatively thick, low-permittivity substrates, result in increased bandwidth and efficiency. However, flexibility decreases dramatically. The work presented in this dissertation introduces new advances in the state of the art for low profile antennas to develop reconfigurable compact HIS antenna. Additionally, it applies these advances in realizing a conformal, self-compensating radiating surface with the goal of improving passive radiometric biomedical sensing.

1.2. Motivation

In collaboration with NASA Glenn Research Center (GRC) and Raytheon, University of South Florida (USF) has been investigating the use of passive radiometric sensors for astronaut health monitoring during extended space flight [1]. Since astronauts on long-duration missions will not be able to return quickly to Earth, new methods of remote medical diagnosis are

necessary. The goal is to develop credit card-sized radiometers that can be integrated into the space suit, with an emphasis on identifying and mitigating the problems associated with close proximity sensing. The same devices can be tailored for use by the military, emergency response personnel, athletes, and in any other application which may involve physical stress over extended periods of time. The research herein will specifically address new solutions for low profile, conformal antennas that allow the antenna properties to be adjusted in response to adverse environmental loading.

1.3. Existing Technology

Relevant existing technologies will be summarized in two sections. The first section presents a brief background on the state of art of low profile tunable antennas. The second section covers flexible antennas.

1.3.1. Low Profile Tunable Antennas

Low profile antennas are desirable for wireless applications. The overall height of this type of antenna is usually less than one tenth of the operating wavelength [2]- [22]. Among the choices for antennas satisfying the above criteria are various forms of microstrip patch antennas. Standard, single-layer patches are typically narrow-band [2] and tuning approaches usually involve devices that are exposed on the outer surface [3], [4], contrary to the embedded solution that is desired in the envisioned radiometric application. Multi-layer patches may offer instantaneous bandwidth covering the frequency range of interest (e.g., [5]). However the thickness of multi-layer patches conflicts with the desire to achieve a flexible, low profile design.

Another typical approach to design low profile antennas consists of placing a horizontal dipole in close proximity to a ground plane. As the antenna gets closer to the electric conductor, the reverse image current cancels out its radiation and degrades the return loss performance. The

2

ground interference issue can be resolved by introducing a textured periodic surface above the ground plane that alters its electromagnetic characteristics [6]-[9]. This structure is known as a high impedance surface (HIS), a frequency-selective surface (FSS) or an electromagnetic band gap (EBG) structure. It operates in a similar fashion as two-dimensional photonic crystals to prevent the propagation of RF surface currents within the band-gap [6]. However, these dipole-type antennas above HIS ground planes tend to have a narrowband performance [2], [7]-[10]. By integrating semiconductor diodes into the surface pattern of the HIS the usable frequency range can be extended. In [13] and [14] a broad tunability range is obtained for an antenna and FSS with thicknesses of $\sim\lambda/25$ and $\sim\lambda/15$, respectively. The approaches used in [13] and [14] required the use of vias to block RF leakage onto the bias lines which increase the fabrication complexity and limits the potential use of flexible substrates for future designs.

Furthermore, the cost, size and robustness of the tunable devices are all important design constraints to enable the development of low profile tunable antennas for biomedical radiometric sensing [21]. In comparison to the semiconductor devices, ferroelectric barium strontium titanite (BST) is relatively simple and inexpensive to process; for the custom-designed interdigital varactors used in this dissertation, only a BST thin film and subsequent electrode-layer deposition are needed. BST can also be deposited onto a ceramic substrate (in this case Al_2O_3) which provides a compact, rigid platform that prevents damage under possible flexing of the thin antenna. In contrast, due to the fragile nature of semiconductor materials such as GaAs and silicon, external plastic or ceramic packages are typically needed to ensure the integrity of the devices and can significantly increase the footprint. Despite the potential advantages of BST varactors, their electronic properties may have yet to match those of semiconductor devices. However, it is still relevant to assess how the aforementioned tradeoffs affect the performance of

the antenna under study. None of the works previously referenced in this section have investigated the use of ferroelectric varactors in low profile tunable antenna applications.

1.3.2. Flexible Antennas

In recent years interest in flexible antennas has increased considerably. Antennas that can be manufactured in a flat state and are flexible enough to conform to non-planar shapes are useful in the biomedical, communications, and defense/security industries. Typically, microwave antennas are made by assembling multiple layers of different materials. Some of these layers are made of metal; generally the backside of the antenna is a metal ground plane and the top side is a metal radiating element. Sandwiched between the metal layers is some kind of non-conducting, insulating material (the substrate). Previous researchers have developed flexible antennas by reducing the thickness of a single substrate layer or by using only one metal layer [23]-[33]. However, these antennas are narrowband and do not meet the requirements of the intended application. In most cases, the antenna performs better as the thickness of the insulating material increases [29]. This is especially true for low profile antennas where the electrical performance (i.e., matching, gain, efficiency, bandwidth, etc.) improves as the antenna thickness increases. On the other hand from a mechanical standpoint, flexibility improves with thickness reduction. Stiffness increases with the cube of substrate thickness and stress increases linearly with thickness limiting the amount of deflection before the antenna permanently deforms or breaks. Thus, there is a conflict between improving the antenna performance by increasing the substrate thickness and improving its flexibility by decreasing the thickness. This leaves the mechanical and electrical challenges to create lightweight and flexible microwave antennas that can be worn comfortably by patients for extended periods of time unaddressed which is an aspect that will be discussed further in this dissertation.

As discussed above, it is of interest to enable the development of flexible, multilayer stack, low profile antennas for biomedical radiometric sensing where the sensor may be embedded in uniforms, prosthetic devices, or other body-worn protection [21]. For this type of electromagnetic sensing, reduction in the back lobes of the radiation pattern is important in order to maximize the detection sensitivity and thus the use of a backing ground-plane is appropriate. However, the two metal layers limit flexibility since the top (radiator) and bottom (ground) copper layers have the highest modulus of elasticity in the antenna structure and are the farthest materials from the neutral bending axis. For this reason the composite structure will most likely fail at either the top or bottom copper layers. Additionally, when these different layers are bonded together the structure tends to become rigid, even if the metal layers are thin and the insulator itself is a flexible material.

To succeed in fabricating this type of antenna, new manufacturing techniques need to be developed. Recent publications on flexible antenna design have demonstrated the use of ultra-thin layers of polydimethylsiloxane (PDMS) (20 to 200 μm) as a possible approach to designing flexible electronics and MEMS devices [35]-[40]. One of the advantages of PDMS is its bio-compatibility. Unfortunately, its inherent hydrophobic properties prevent this material from adhering easily to others (e.g. liquid crystal polymer (LCP), copper, etc.) which creates the need to explore for viable solutions. The following are current alternatives that have been used to fabricate flexible antennas:

- In [41]-[42] epoxy-based negative photoresist SU-8 was treated with (3-Aminopropyl)triethoxysilane (APTES) and plasma etching to create an intermediate layer and bond two or more layers of PDMS. The antennas were ultra-thin (200 μm). The metal

5

deposition requires the use of sacrificial layers which increases the complexity of the process.

- In [28] a thin SU-8/PMDS flexible antenna was fabricated using metal deposition on sacrificial layers which were later transferred to the PDMS to keep it from high temperature stress. The antenna had an initial thickness of 0.5 mm. However, difficulties in soldering the subminiature version A (SMA) connector to the ground of the patch required that an FR-4 epoxy-based laminate board be placed below the patch as a support, making the antenna semi rigid and increasing its thickness to 2.1 mm.

- In [36] a patch antenna was encapsulated in a PDMS/LCP substrate avoiding the use of transferring layers or metal deposition. The encapsulation releases the metal layers from maximum stress and strain, as they are not anymore the farthest layers from the neutral axis. The latter approach increases the antenna profile, degrades its performance, and does not provide a permanent solution to the LCP/PDMS adhesion problem as eventually air bubbles appear between the layers and the LCP is delaminated.

- In [35] the PDMS was mixed with ceramic powder to create a blended polymer–ceramic which was used to investigate the performance of metal epoxy-printed patch antennas. The brittle nature of metal epoxy makes this approach susceptible to cracks.

This dissertation aims to provide solutions and a path towards future design to address the problems imposed by the close proximity of the radiometric sensor as discussed in this section. Section 1.4 provides a summary of the contributions accomplished through the research and designs presented herein.

1.4.   Contributions

This dissertation aims to advance the fundamental knowledge in low profile tunable planar antennas. Herein the contributions of a series of antenna architectures to the state of art are highlighted. The first generation of antennas, using Jerusalem crosses (JC) as the FSS structure [10], showed a fractional bandwidth of 1.41%. The need to increase the bandwidth motivated research into alternative FSS structures. Square Patches (SP) were selected as an alternative because of the inherently broadband response and a new series of antennas were designed and fabricated. The second generation of antennas showed an increase in the fractional bandwidth from 1.4% to 2.68% when a SP-FSS (non-tunable symmetrical HIS) was used as a cell structure [43]. The antennas had thickness of $\lambda/50$. These designs were the first low profile antennas to demonstrate adequate performance for substrate thicknesses lower than $\lambda/30$ [8]-[13]. This comparison showed the influence of the unit cell geometry on the performance of a low profile antenna [43], [44].

A third generation using discrete capacitors was designed. The major contribution of this design was demonstrating comparable performance between a non-loaded and a capacitively-loaded FSS with a significant reduction in the number of cells and/or cell geometry size. The total antenna area was reduced by 12% [45]. It also demonstrated that the provision of discrete capacitive loads reduced the FSS susceptibility to fabrication tolerances based on placement of a fixed grid capacitance. The antenna with discrete capacitors showed a fractional bandwidth of 9.2% for a thickness of $\sim\lambda/40$. These results represent an improvement over previous publications which showed fractional bandwidths of 5% for thicknesses of $\lambda/30$ [11]- [14].

Tunable low profile antennas, the fourth and fifth generations, were designed using a non-uniformly biased varactor-tuned frequency selective surface (FSS) [21], [46]- [47]. These

investigations illustrate how the coupling between antenna and HIS and the varactors losses affect the antenna performance. These designs showed frequency tunability from 2.2 GHz to 2.6 GHz, reduction in the back lobes of the radiation pattern, and frequency adjustment in response to adverse environmental loading, demonstrating the potential use of these types of antennas for radiometric sensing applications.

This dissertation advances the state of the art of thin, frequency-tunable planar antenna design; investigates the integration of high-quality ferroelectric thin-film devices into flexible, multi-layer polymer substrates; and applies these advances in realizing a conformal, self-compensating radiating surface. It is the first demonstration of a BST varactor based flexible low profile tunable antenna. The fabrication, modeling, and integration of BST chips was demonstrated initially using commercially available substrates in [46] and later using in-house fabricated flexible material in [48].

The challenging problems of fabricating robust flexible antennas are also addressed and novel solutions are proposed. Hybrid manufacturing approaches to achieve flexibility on electrically thick antennas that could be transitioned to thin-film microelectronics were developed in [48], [49]. These new approaches were used to overcome limitations commonly encountered in the design of antennas that are intended for use on non-flat surfaces. These approaches demonstrated to be promising methods to fabricate flexible antennas. The work was enabled by a new process to bond polydimethylsiloxane (PDMS) and liquid crystal polymer (LCP) layers using SU-8 and (3-Aminopropyl)triethoxysilane (APTES) as intermediate layers[1].

Finally, other contributions of this dissertation are in the electromagnetic modeling field. A novel quasi-static analysis for the asymmetric tunable unit cell was presented in [21] where it

---

[1] Developed by Abhishek Dey from the center for wireless and microwave information systems at University of South Florida.

was shown how the current edge effect affects the model prediction on this type of tunable FSS. Furthermore, a modified equation to calculate the full capacitance of coplanar waveguide (CPW) structures that improves the accuracy of the conformal mapping-based model is presented in [50].

1.5.   Dissertation Organization

This dissertation is organized into six chapters, with 1 and 6 corresponding to the introduction and conclusion, respectively. Chapter 2 shows the theory and background relevant to understanding the challenges on designing low profile tunable antennas. Chapters 3 through 5 describe various types of antenna designs and the main contributions of this dissertation. All mathematical development of some equations, programs and copyright permissions can be found in the appendices section.

Chapter 2 presents a review on theory and concepts related to the design of low profile antennas. First, a review on some of the challenges when a horizontal dipole is placed in close proximity to an electric conductor is discussed. The theory of surface waves and high impedance surfaces (HIS) is presented within the context of the principle of operation of the type of antennas under study. Finally, an overview on the concept of designing low profile tunable antennas using HIS, is given.

Chapter 3 discusses the design of non-tunable low profile antennas. It explains the design of the different elements within this multilayer structure, the broadband planar radiation, the balun, and the HIS. The effects of the metal backing on the antenna performance are also discussed. Finally, chapter 3 compares the impact of using square patches versus Jerusalem Crosses as unit cell geometries for the presented design on the antenna performance and the advantages of using discrete capacitors.

Chapter 4 discusses the design of tunable low profile antennas. A complete theoretical and experimental study of a low profile, 2.4 GHz dipole antenna that uses a frequency selective surface (FSS) with semiconductor varactor-tuned unit cells is detailed. Furthermore, similar of a study on a 2.4 GHz low profile dipole antenna that uses a frequency selective surface (FSS) with interdigital barium strontium titanate (BST) varactor-tuned unit cells is carried out. The antennas are placed in close proximity of a Human Core Model (HCM) phantom and their performance evaluated and compared to each other.

Chapter 5 presents the development and design of flexible BST-based low profile flexible antennas. Here, a fabrication process for flexible electrically-thick LCP/PDMS microstrip antennas is explained in detail. Additionally, the design and fabrication of flexible low profile antennas is also explained and a comparison among the different antennas is carried out. Novel fabrication techniques to realize and fabricate flexible robust antennas are also shown.

CHAPTER 2: BACKGROUND REVIEW

2.1.   Introduction

This chapter presents a review on the theory related to electric conductors in close proximity to a horizontal antenna. A review on high impedance surfaces (HIS) theory and some properties such as surface wave propagation and reflection phase characteristics is also presented.   Methods to analyze and design these structures as well as some of the approaches and work done by other authors are also discussed.

2.2.   Horizontal Antennas Above a Ground Plane

Low profile antennas are of great interest for wireless applications due to their potential advantages on size, weight, and power (SWaP). Their overall height, which is usually less than one tenth of the operating wavelength, makes these antennas a good choice when conformability and portability are desired [51]. To maintain acceptable performance, one typical approach is to place the antenna nearby an electrical conductor that serves as a ground plane. The presence of the ground plane improves the antenna gain by 3 dB and serves as electromagnetic shielding [6], [52]. However, if the antenna is too close to the ground plane the coupling effect between ground and the antenna, in addition to the image current cancellation effects, results in poor radiation efficiency. To address this problem, the antenna can be separated from the ground plane a by distance of $\lambda/4$, where λ is the wavelength corresponding to the frequency of operation of the antenna [6]. The tradeoff is that the overall height of the antenna increases.

To illustrate the limitations on performance by an antenna in close proximity to an electric conductor, consider the case of a horizontal dipole above a ground plane at a height h as

shown in Figure 2.1. Assuming that the ground plane is a perfect electric conductor (PEC), then the tangential component of the electrical field must be zero at its surface [53]. Thus, to enforce the boundary condition, the reflected wave must have a phase reversal of 180° at the antenna. A detailed explanation is given in [54] and the above statement is demonstrated using a method of images where, as the distance from a dipole antenna to ground (h) increases, the effect of mutual coupling decreases and its radiation resistance approaches that of the free space value. Figure 2.2 shows a comparison of the reflection scattering parameter (S_{11}) of a 2.5 GHz broadband dipole in free space, at a distance $\lambda/25$ from a PEC and at a distance $\lambda/4$ from a PEC. The simulations performed using Ansoft's High Frequency Structural Simulator (HFSS) demonstrate the improvement on the return loss as the antenna separates and decouples from the ground plane.
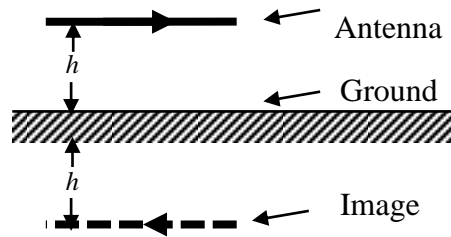
Figure 2.1: Horizontal antenna above a ground plane at distance h.
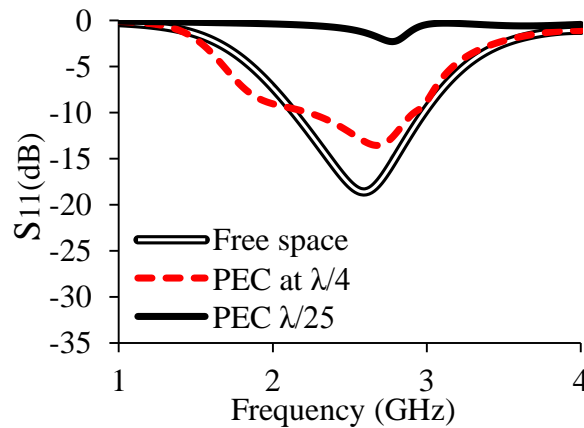
Figure 2.2: S_{11} comparison of a dipole antenna in free space, at a distance $h=\lambda/25$ from a PEC and at a distance $h=\lambda/4$ from a PEC.

12

2.3.   Surface Waves

Surface waves are electromagnetic waves that are bound to the interface between two materials. These waves decay with a distance from the interface and they are classified either as transverse magnetic (TM) or transverse electric (TE) waves. The type of surface wave is defined by the properties of the surface in which it is propagating. Consider a wave propagating in a surface of impedance Z_s and decaying away from it with decay constant α as shown in Figure 2.3. If the propagating surface is inductive, then TM waves can exist and its surface impedance Z_s is given by (2.1)
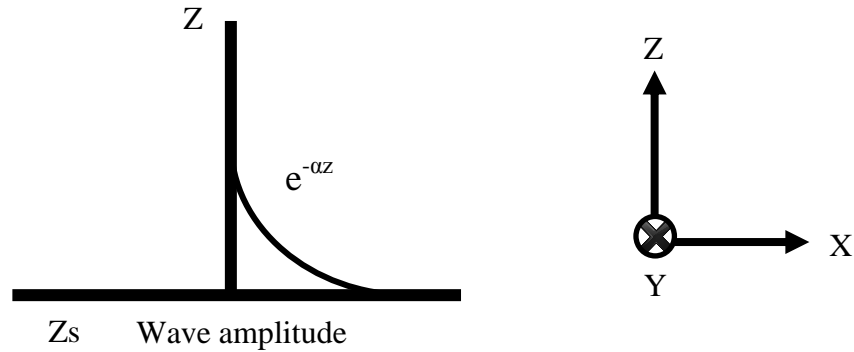
Figure 2.3: Surface wave bound to a surface propagating in the X direction and decaying into the surrounding space with a decay constant α in the Z direction. (Reprinted with permission from [9] according John Wiley & Sons permissions policy see Appendix G, section G.1).

$$Z_s = \frac{j\alpha}{\omega\varepsilon}$$
(2.1)

Conversely, if the surface is capacitive, then TE waves can exist with surface impedance Z_s given by (2.2)

$$Z_s = \frac{-j\omega\mu}{\alpha}$$
(2.2)

13

where μ and ε are the permittivity and permeability of the surrounding materials and ω is the angular frequency of the wave. Due to the fact that metals are slightly inductive, these only support TM surface waves. At microwave frequencies, these TM surface waves are simply the ordinary surface currents bounded weakly to the surface. For the case of a horizontal antenna in close proximity to an infinite flat and smooth ground plane, the surface wave will simply decay exponentially with a decay constant α. However, if the ground plane is finite, these surface currents propagate to the edge and the ground plane and can then radiate. This phenomenon causes undesired ripples in the radiation pattern which may degrade the antenna performance [52], [55]. Besides, if multiple antennas are sharing the same ground plane, these waves can produce coupling between them. To prevent the propagation of these types of waves, a new type of periodic structure called a high impedance surface (HIS) structure has been developed.
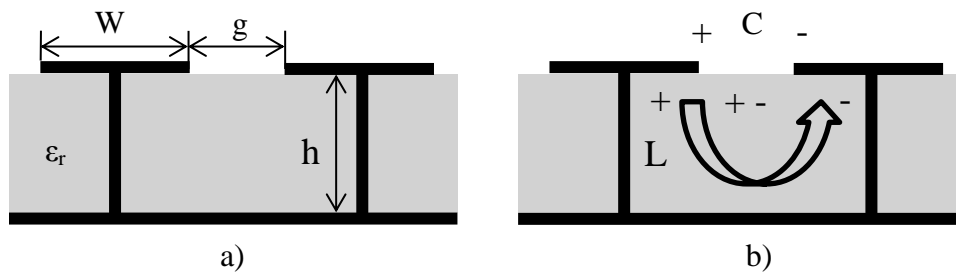
Figure 2.4: a) EBG parameters and b) LC model of a mushroom like EBG structure. (Reprinted with permission from [51] according to Cambridge University Press permissions policies-see Appendix G, section G.2).

2.4.   High Impedance Surfaces

In recent years metamaterials have been used in the field of electromagnetics. The term is used to define materials with properties and characteristics that cannot be found in nature. In [51], materials are classified based on their properties as double negative material (DNG), left-handed (LH), negative refractive index (NRI), artificial magnetic conductors (AMC), soft and hard surfaces, magneto materials, and high impedance surfaces (HIS). Some materials exhibit

properties associated with more than one of the above classifications (e.g., the DNG material always shows NRI and LH properties). The metamaterials of interest in this dissertation are HIS which are manufactured material with large surface impedance for the TE and the TM modes.

One of the most widely used structures in the antenna field is the mushroom-like electromagnetic band-gap structure (EBG). This type of structure exhibits properties of HIS and AMC. If the incident wave is a surface wave ($k_x^2 + k_y^2 \leq k_0^2$, k_z^2 is imaginary), the EBG provides a surface wave bandgap, within which it does not support bound surface waves of either transverse magnetic (TM) or transverse electric (TE) polarization [52]. If the incident wave is a planar wave ($k_x^2 + k_y^2 \leq k_0^2$, k_z^2 is real), the EBG reflects back an impinging wave more in phase than out of phase (with a phase shift of zero rather than 180 degrees) similar as with a perfect magnetic conductor (PMC). In this material the tangential component of the magnetic field must vanish next to its surface. In addition the magnetic and electric conductivity in the surface are infinity and zero, respectively. This material does not exist in nature but may be approximated by using these corrugated surfaces. In the above expressions k_0 is the free space wavenumber and k_x, k_y, k_z are wavenumbers in the x, y and z directions of Figure 2.3, respectively. The mushroom-like EBG geometry depicted in Figure 2.4a consists of a metallic patch connected to ground through a shorting via [6]-[9]. If the periodicity of the unit cell is small compared to the operating wavelength, then the material can be analyzed as an effective medium. Thus, the EBG can be modeled with an equivalent lumped LC element in which the width of the patch (W), gap separation between patches (g), height of the substrate (h) and dielectric constant (ε_r) are some of the most important design parameters. The capacitance C is defined in the model shown in Figure 2.4b as the effective sheet capacitance between patches and the inductance L as the sheet

inductance. The surface impedance is calculated from the parallel resonant LC circuit using the expression (2.3)

$$Z_s = \frac{j\omega L}{1 - \omega^2 LC} \tag{2.3}$$

The resonant frequency can then be calculated by equating the denominator from (2.3) to zero

$$f_r = \frac{1}{2\pi\sqrt{LC}} \tag{2.4}$$

From equation (2.3), it can be determined that for frequencies below resonance, the surface is inductive and supports TM waves. Above the resonance frequency, the surface is capacitive and supports TE waves. At the resonance frequency the impedance is very high with respect to the impedance of free space for a range of frequencies and the material does not support TE or TM surface waves.
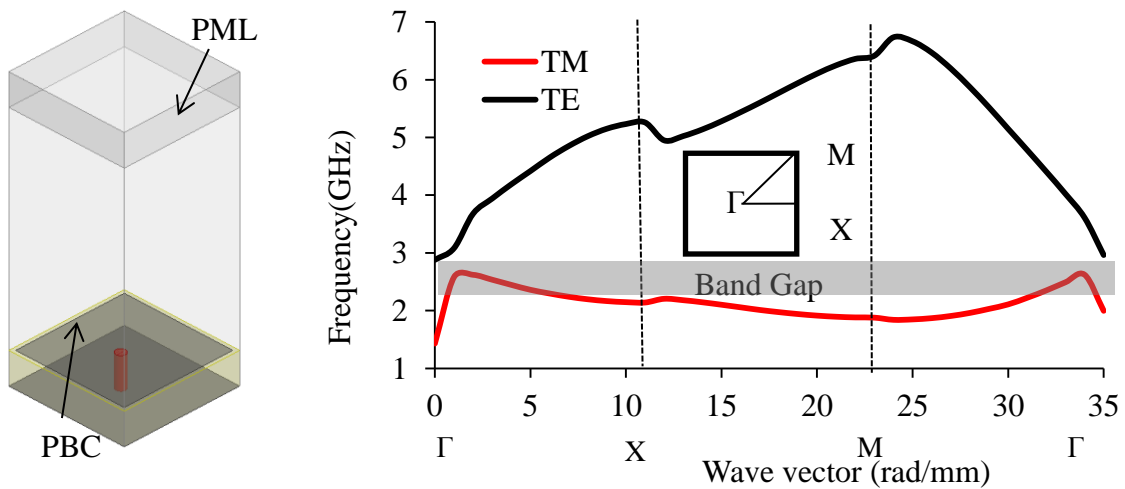
Figure 2.5: a) EBG unit cell (W = 8mm, g= 0.2 mm and h = 2.5mm) and b) dispersion diagram.of an EBG unit cell structure that exhibits a surface wave bandgap.

16
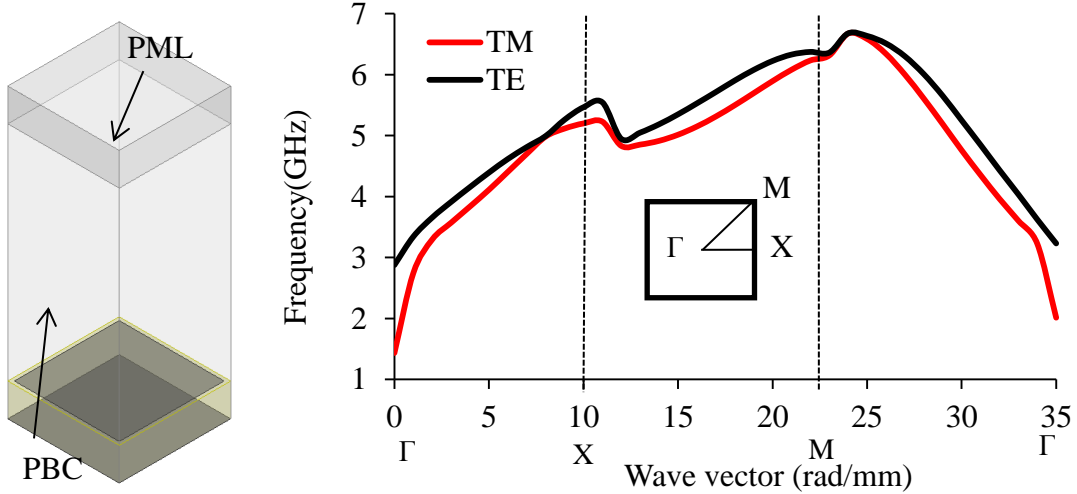
Figure 2.6: a) FSS unit cell (W = 8mm, g = 0.2 mm and h =2.5mm) and b) dispersion diagram of a FSS unit cell structure that does not exhibit a surface wave bandgap.

To analyze the surface wave properties of these structures, dispersion diagrams are used as they provide accurate plots to visualize them. To obtain the dispersion diagram, a full wave simulation is performed to determine the wavenumber. For a periodic structure such as EBG, the field distribution of the surface wave is also periodic. Thus, a unit cell can be simulated with the appropriate periodic boundary conditions (PBC) and perfectly matched layers (PMLs). Figure 2.5 shows an EBG unit cell and the dispersion diagram of the EBG structure characterized using Ansoft HFSS. The vertical axis shows the frequency and the horizontal axis represents vector quantities. Γ, X and M represent propagation vectors in the Brillouin zone [51]. Note that in mushroom like EBG structure a surface wave bandgap exists in the frequency range from 2.4 to 3 GHz, which means that inside this band the surface waves will be suppressed. In contrast if the vias are removed from the structure, a surface wave bandgap does not exist and the TM mode will propagate in the frequency range from 2.4 GHz to 3 GHz. This type of structure with no via is usually referred as a frequency selective surface (FSS). Figure 2.6 shows an FSS unit cell with no vias, and the dispersion diagram of the FSS structure where a surface wave bandgap does not

exist. The HISs used in this dissertation do not have vias and thus the radiation pattern can be affected by the existence of surface waves; however the absence of vias facilitates the potential use of flexible substrates.

To analyze plane wave incidence properties, the reflection coefficient magnitude and phase plots are used. The phase of the reflection coefficient is an important parameter to evaluate the performance of FSS structures. Figure 2.7 shows the reflection coefficient phases at normal incidence of the EBG and FSS unit cells in Figure 2.5 and Figure 2.6. When the impedance of the FSS surface is low, the reflection coefficient phase is $\pm 180°$ and when the impedance of the surface is high, the reflection coefficient phase is close to zero degrees. The fact that the image currents on the FSS are more in-phase than out-of-phase when the reflection coefficient angle falls between $\pm 90°$, has been used to date as the criterion by which the "bandwidth" of the FSS is defined (grey shadowed region in Figure 2.7). However, a more rigorous criterion for designing purposes would be to consider the bandwidth of the FSS between $\pm 45°$ (green region). The magnitude of the reflection coefficient is shown in Figure 2.8. The optimum reflection coefficient is $\left| 1 \right| \llcorner 0°$ because the reflected wave is added constructively to the incident wave at the antenna layer. In terms of antenna design criterion, the magnitude of the reflection coefficient is usually required to be $> \left| 0.8 \right|$, which corresponds to the minimum value for effective FSS operation. Note that the presence or absence of vias has little effect on the reflection coefficient plots. In summary, an FSS structure (no vias) has similar reflection phase as the EBG structure (with vias), but it does not have a frequency band gap in the dispersion diagram to suppress surface waves. In the following section an overview on the concept of designing low profile tunable antennas using HIS is provided.
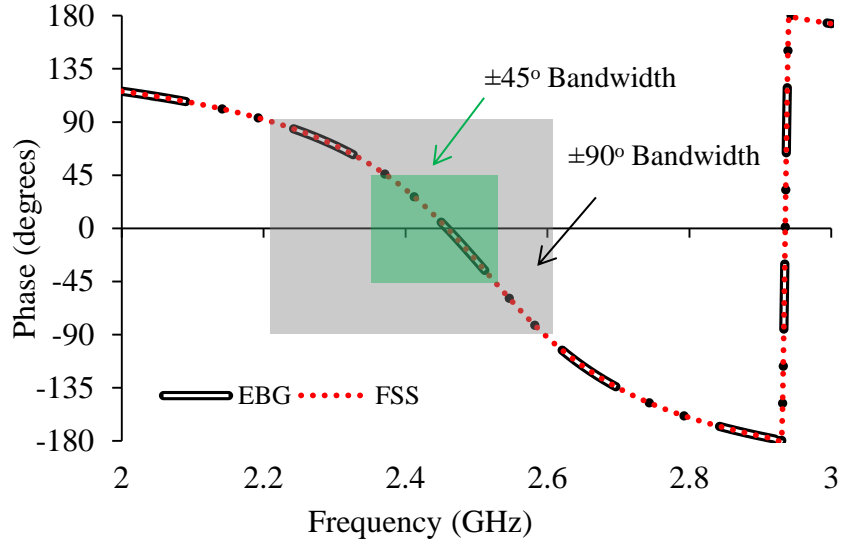
Figure 2.7: Reflection coefficient phases for an EBG and FSS structures shown in Figure 2.5 and Figure 2.6.
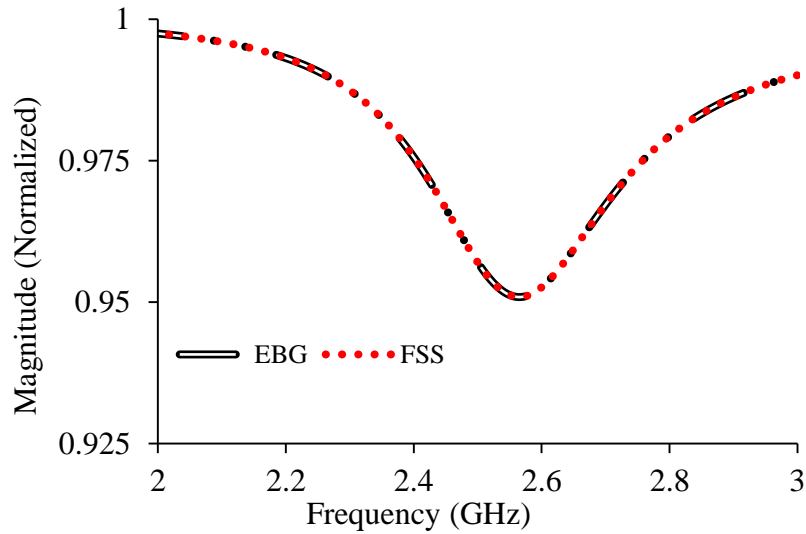
Figure 2.8: Reflection coefficient magnitudes for an EBG and FSS structures in Figure 2.5 and Figure 2.6.

2.5.   Low Profile Tunable Dipole Antennas Using High Impedance Surfaces

In section 2.2 a horizontal dipole was placed in close proximity (at a distance $\lambda/25$) to a PEC and it was explained that the direction of the image current is opposite to that of the original, resulting in a very poor return loss. In [8], simulations demonstrated that by replacing the PEC below the dipole by a PMC, the return loss improves as the latter has reflection

coefficient phase of 0°. Unfortunately, the PMC surface is an ideal surface that does not exist in nature. However, it is possible to replace the PEC by an HIS, which exhibits properties similar to the PMC within a certain frequency band (see Figure 2.9). These structures are typically used as the back reflector for antennas to reduce back side lobes, improve gain, increase efficiency and minimize coupling between radiating element of arrays. The antenna electrical performance (i.e. matching, gain, efficiency, bandwidth, etc.) is highly influenced by the type of geometry, dimensions, substrate height and material of the HIS. Figure 2.10a shows the reflection coefficient phase and magnitude of a square patch based HIS. The width of the patch (W), gap separation between patches (g), height of the substrate (h) and dielectric constant (ε_r) of the unit cell were optimized to operate at a central frequency of 2.45 GHz. The $\pm 90^o$ and $\pm 45^o$ bandwidths of the reflection coefficient phase are ~400 MHz and 200 MHz, respectively. The magnitude is 0.9 which is higher than the design criterion. From Figure 2.10b, it is observed that the dipole exhibits a return loss better than 10 dB from 2.35 to 2.55 GHz. which agrees with the results for the reflection coefficient phase obtained from the plane-wave model at the 45° boundaries.
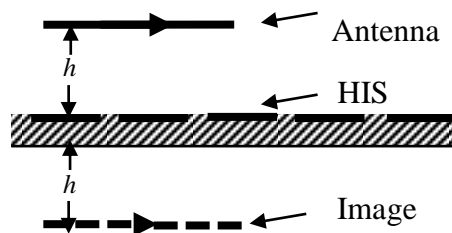
Figure 2.9: Horizontal antenna above an HIS at distance h.

To extend the frequency range of this type of antennas, the resonance frequency of the high-impedance surface can be tuned. This can be performed by changing the sheet capacitance, the sheet inductance, or both. Changes in inductance require either changes on the thickness of

the substrate or using magnetic materials since the inductance depends on permeability and height of the substrate. However, without magnetic active materials the inductance is difficult to tune. On the other hand, to change the sheet capacitance the geometry of the periodic structure can be modified or tunable lumped capacitors can be added between metal patches.
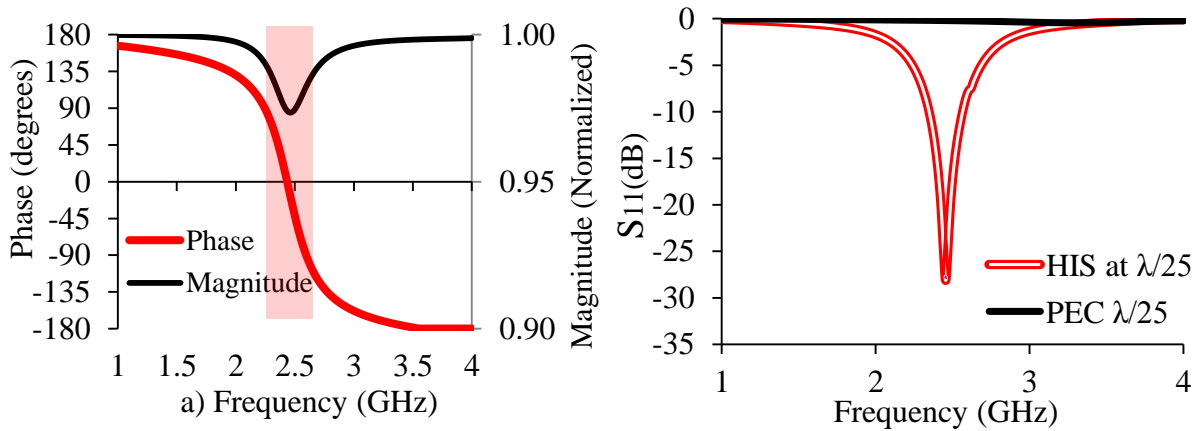
Figure 2.10: a) Reflection coefficient phase (degrees) and magnitude (normalized). b)S_{11} comparison of a dipole antenna at a distance $h= \lambda/25$ from a PEC and from an HIS.
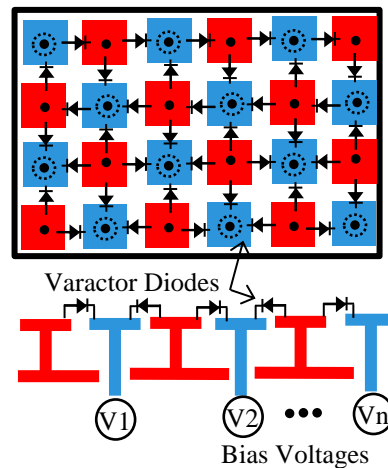
Figure 2.11: An electronically tunable HIS with varactor between adjacent unit cells and vias to bias them. (Reprinted with permission from [9] according to John Wiley & Sons permissions policy- see Appendix G, section G.1).

21
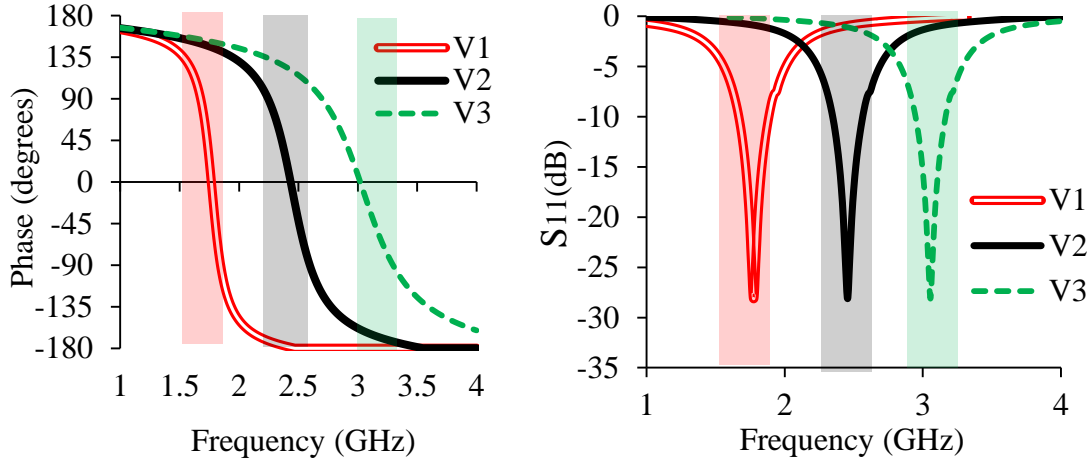
Figure 2.12: a) S_{11} phase of an electronically tunable HIS for different bias voltage on the varactors. b) S_{11} magnitude of a dipole antenna over and an electronically tunable HIS separated from the antenna by $\lambda/25$, for different biasvoltage on the varactors ($V_1 < V_2 < V_3$).

Figure 2.11 shows a tunable HIS. The varactors are placed between adjacent metal plates in opposite directions in each alternate row. To supply DC bias to the diodes, holes are drilled and vias are placed in the metallic structure. Half of the vias are grounded, and the other half is connected to a voltage control network. When a voltage is applied to the bias lines the effective capacitance of the varactors changes, adjusting the sheet capacitance and tuning the resonance frequency. For a low input voltage the capacitance is high, and for a high input voltage the capacitance is low. Figure 2.12 depicts the phase and magnitude (dB) of S_{11} of a horizontal dipole placed at a distance $\lambda/25$ from a tunable HIS. The simulations demonstrate frequency tuning on the phase and return loss. As the voltage increases, the capacitance decreases and the resonance frequency of the dipole increases in accordance to equation (2.4).

2.6.   Conclusion

In this review, supporting information has been detailed which will facilitate the understanding of concepts presented later in this dissertation. The adverse effect of having a horizontal dipole in close proximity to an electric conductor has been explained. A summary on

22

the theory of HIS and their properties have been presented. Finally, an overview on the concept of low profile tunable antennas using HIS was shown. In the following chapter design considerations, fabrication methodology, and results of broadband horizontal dipole over an HIS are presented.

CHAPTER 3: END-LOADED PLANAR OPEN SLEEVE DIPOLE BACKED BY STATIC

HIGH IMPEDANCE SURFACES (HIS)

3.1.   Introduction

This chapter presents the design and results of low profile tunable antennas backed by non-tunable or static HIS. The antennas developed in this chapter consist of three layers. The first layer is a broadband radiator, the second layer is the HIS, and the third is a feed layer. Initially, the designs of the broadband planar radiator and the feed layer chosen for this work are explained. Subsequently, the design of different antennas using different non-tunable unit cells is presented. The goal of this chapter is to compare the performance of antennas using different unit cell geometries and to show the methodology used by the author to design low profile antennas.

3.2.   End-Loaded Planar Open Sleeve Dipole

3.2.1. End-Loaded Planar Open Sleeve Dipole Selection

In this section a planar broadband antenna is designed. The desired frequency of operation for the preliminary work is the 2.4 GHz industrial, scientific and medical (ISM) band. This frequency was selected for the initial tests not only because of the aforementioned relevance but also because of the availability of instrumentation and facilities to perform in-house measurements.

Based on the design criterion of high bandwidth, various types of planar broadband antennas were considered and compared against each other. Among this group of antennas the following design types are referenced in this section: microstrip antennas with coplanar resonator

and gap-coupled parasitic patches, triple-layer triangular patch antenna, and E-shaped patch antennas.

Microstrip antennas are being considered in a great deal of design applications due to their unique advantages, especially their low weight, low complexity and low cost fabrication. A narrow bandwidth is a major disadvantage of microstrip antennas for practical applications. One technique that is currently being implemented to achieve bandwidth enhancements (broadband) for microstrip antennas is the use of gap-coupled parasitic patches [56]. By using additional patches directly coupled to the radiation or non-radiating edges of a broadband rectangular microstrip antenna can be achieved [57]. However, there is one main disadvantage to these broadband configurations in that the overall planar size of the antenna increases [4], [57].

Another type of broadband antenna is the triple-layer triangular patch antenna. This type of antenna consists of three layers, each containing a triangular patch of different sizes. In comparison to other types of patch antennas, the triangular patch offers a considerable increment on the fractional bandwidth (~33%) as demonstrated in [5]. In addition, the triple layer triangular patch antenna provides a relatively small patch size (30mm-50mm at 2 GHz). Unfortunately, the implementation of a multilayer structure imposes a height constraint which affects low profile and conformal characteristics.

A third type of broadband antenna considered is the E-shaped patch antenna. The main advantage introduced by the E-Shaped patch antenna is a wide bandwidth, which could exceed 30% [58]. Nevertheless, the dimensions of the antenna are still large for many applications such as human health monitoring or unmanned aerial vehicles. An improvement to the large size in [58] is provided by [59]- [60], offering a compact broadband E-shaped patch antenna exhibiting 30% of the area of a conventional design [58], but with only of 12.6% fractional bandwidth.

In comparison to the planar elements discussed above, the ELPOSD antenna is best suited for applications requiring broadband compact radiators due to the simplicity of its design (single layer), wide bandwidth (~25%) [61], flexibility, and conformability.

3.2.2. End-Loaded Planar Open Sleeve Dipole Design

The radiator preferred for this work consists of a broadband dipole, the end loaded planar open sleeve dipole (ELPOSD), printed on a thin dielectric material ($\varepsilon_r = 10.2$). The ELPOSD presents itself as one of the best candidates due to the various parameters within this configuration which offer a tunable antenna and a wider operating bandwidth [61].

The ELPOSD configuration consists of a printed dipole that is loaded with two parallel sleeves, and has parasitic capacitive loading at the ends of the dipole arms, as shown in Figure 3.1. The loading elements offer design miniaturization while the parasitic sleeves contribute with a wider bandwidth [61]. This antenna is usually fed by two wires coming from the output of a low profile balun as demonstrated in [62].
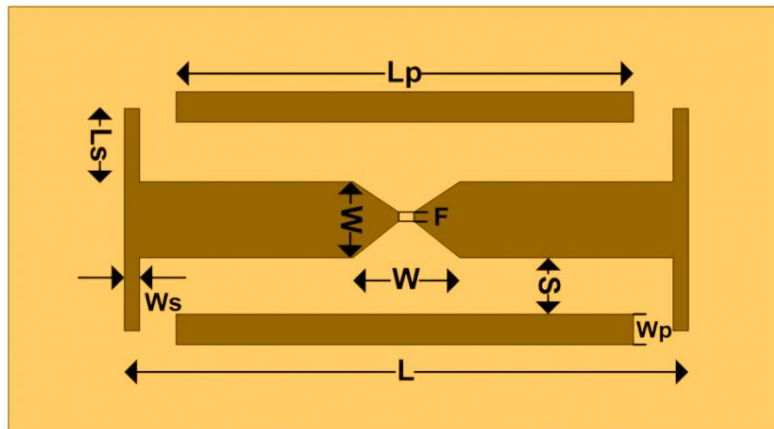
Figure 3.1: ELPOSD geometry.

The ELPOSD antenna type selected for this work provides several design parameters that can be varied to achieve a wider range of voltage standing wave radio (VSWR) performance and

26

operating bandwidth with negligible change in the radiation patterns [63]. A list of the parameters for the ELPOSD antenna is shown below and detailed in Figure 3.1:

- L and W = Length and Width of the Dipole

- W = length of the dipole feed

- L_p and W_p = Length and Width of the Parasitic element

- S = Space between the tapered feed and parasitic

- L_s and W_s = Length and width of end-load stub length

- F = width of the tapered dipole feed

The ELPOSD was first simulated without metal backing (Figure 3.2) and considering ideal 50Ω feed lines to determine preliminary antenna operation. The ELPOSD was designed to operate within the range of 2 GHz to 3 GHz using a 1.27 mm-thick Rogers® RT6010 substrate with a dielectric constant of 10.2. The ELPOSD parameters were optimized using Ansoft's High Frequency Structural Simulator (HFSS). The impact of these parameters on the antenna performance is explained in detail in [61]. The bandwidth of the antenna will be affected by the length of the dipole (L), parasitic elements (L_p) and the coupling between these two (S). The overall size of the ELPOSD in Figure 3.2 is 56 x 40.3 mm^2. The respective size for each parameter is listed in Table 3.1.
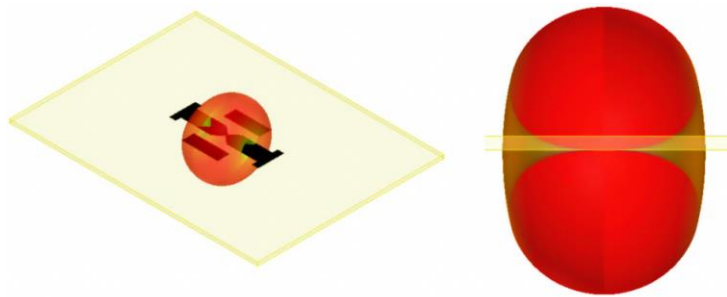
Figure 3.2: 3-D view of the radiation pattern of ELPOSD in free space at 2.5 GHz with no ground plane (left). Isometric view of the ELPOSD and its radiation pattern view and right: front view of the radiation pattern (right).

27

Table 3.1: Antenna dimensions for ELPOSD from Figure 3.1.

Length of Dipole (**L**)	35 mm
Dipole Width (**W**)	19 mm
End-Loaded Lengths (**Ls**)	1.99 mm
End-Loaded Width (**Ws**)	2.35 mm
Parasitic Element Lengths (**Lp**)	11 mm
Parasitic Element Width (**Wp**)	19 mm
Element Spacing (**S**)	1.5 mm
Dipole Feed Width (**F**)	0.6 mm
Substrate Dielectric Constant (**ε_r**)	10.2
Substrate Loss Tangent (**tanδ**)	0.0023
Substrate Thickness (**h**)	1.27 mm

The S_{11} simulation of the ELPOSD shown in Figure 3.3, demonstrated a bandwidth extending from 2.0 GHz to 3.0 GHz (1000 MHz or 41%) using the 10 dB bandwidth criterion. The gain versus frequency plot, Figure 3.4, shows the gain increasing as the frequency increases. The recorded gain at 2.4 GHz is ~2 dB.
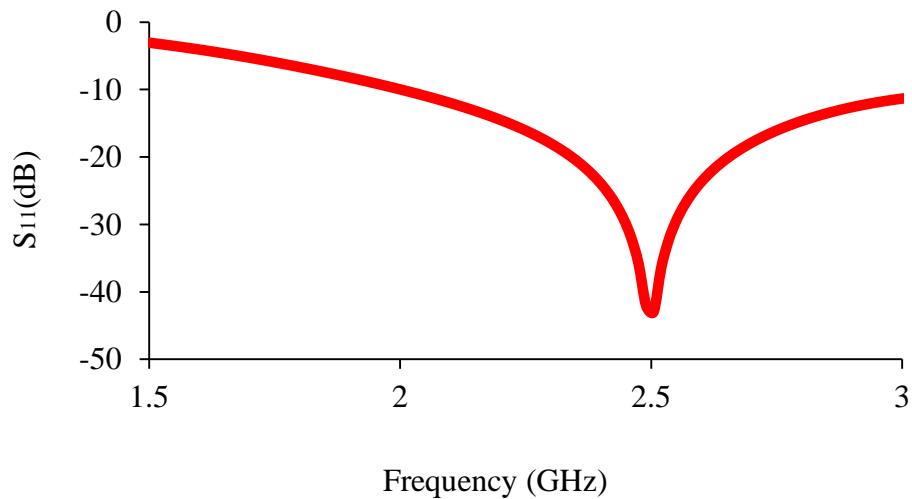
Figure 3.3: S_{11} for the ELPOSD with no metal backing.
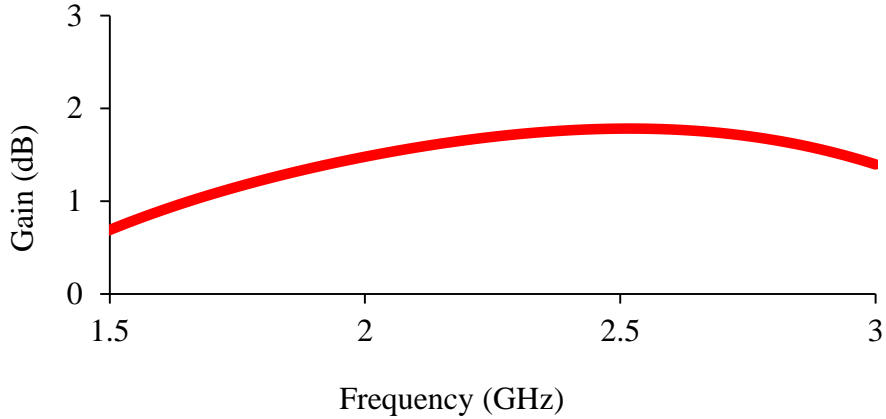
Figure 3.4: Gain vs. Frequency for ELPOSD with no metal backing.

3.2.3. Balun Design

The balun serves a transition between the unbalanced line (microstrip) to the balanced lines (Coplanar stiplines-CPS). A detailed explanation of the design and the excitation modes are given in [62]-[64]. In [62] a microstrip to CPS transition line was designed to operate at a central frequency of 2.4 GHz connecting the CPS lines to a Yagi-Uda radiator in the same layer and using a substrate with dielectric constant of 10.2 and thickness of 2.54 mm; herein the balun was optimized to operate within the range of 2 GHz to 3 GHz using a 1.27 mm-thick Rogers[®] RT6010 substrate with a dielectric constant of 10.2. The CPS lines of the balun are connected to the ELPOSD (located in a different layer) using two wire transmission lines. Figure 3.5 shows the two vias connecting the ELPOSD to the balun.

The two wire lines were designed to have an impedance of 50Ω. The two-wire transmission line model shown in Figure 3.6 and the formulas in Table 3.2 were used given the fact that the length of the vias (~3.81mm) is a considerable fraction of the guided wavelength. A 22 AWG wire (0.64 mm diameter) was used to connect the balun to the ELPOSD; therefore, the distance between center to center of the vias was chosen to be 1.5 mm to achieve 50-ohm characteristic impedance for a dielectric constant of 10.2.

29
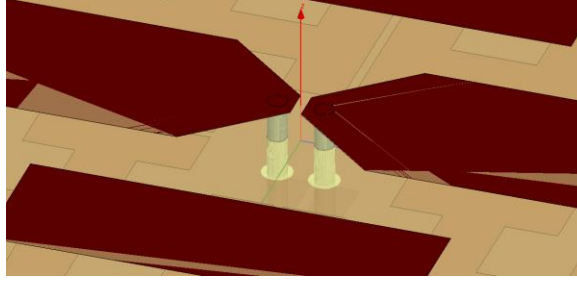
Figure 3.5: Vias connecting the ELPOSD to the balun.
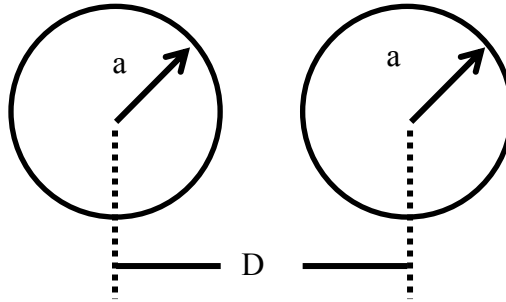
Figure 3.6: Two wire transmission lines parameters.

Table 3.2: Two wire transmission lines parameters.

Inductance	$\dfrac{\mu}{\pi}\cosh^{-1}\left(\dfrac{D}{2a}\right)$
Capacitance	$C = \dfrac{\pi\varepsilon'}{\cosh^{-1}\left(\dfrac{D}{2a}\right)}$
Resistance	$R = \dfrac{R_s}{\pi a}$
Conductance	$G = \dfrac{\pi\omega\varepsilon''}{\cosh^{-1}\left(\dfrac{D}{2a}\right)}$
Impedance	$Z_0 = \sqrt{\dfrac{R + j\omega L}{G + J\omega C}}$

Simulation of the microstrip-to-CPS transition and the vias was performed using Ansoft's HFSS. The dimensions of the balun were optimized to achieve an optimum performance around 2.45 GHz. The results in Figure 3.7 demonstrate a good input match to the microstrip section and

30

maximum power transfer through the microstrip line to the vias. Figure 3.8 shows S_{11} and S_{21} of the structure with a central frequency at ~2.5 GHz. The dimensions for the microstrip to CPS balun are listed on Table 3.3.
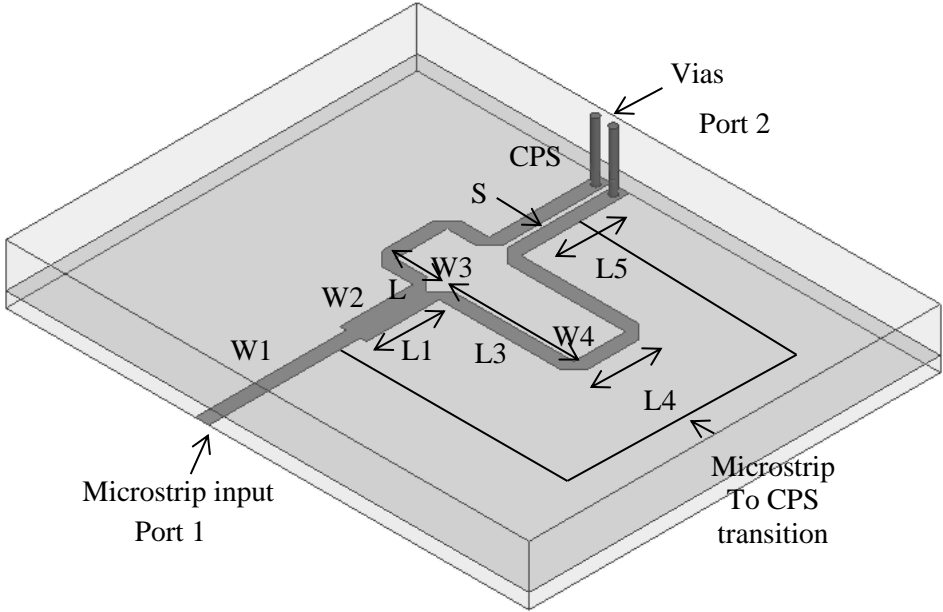
Figure 3.7: Microstrip to CPS transition and the two wire vias simulated in Ansoft HFSS.
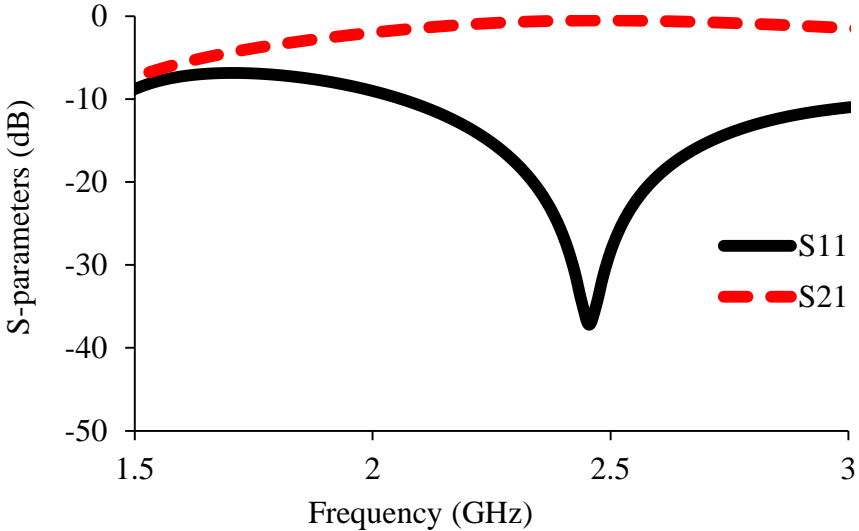
Figure 3.8: S_{11} and S_{21} for the baluns and vias.

Table 3.3: Dimensions for microstrip to CPS transition.

Antenna Element	Dimensions (mm)
Microstrip Width (W1)	1.167
Length of 0.25λ transformer (L1)	6.191
Width of 0.25λ transformer (W2)	2.24
T-junction delay, L3-L2 = 0.25λg	12.95-4.3=8.62
Width on T-junction (W3 = W4)	1.167
Length on T-junction (L4)	5.54
Length on T-junction/CPS (L5)	9.2
T and CPS coupled section (S)	0.378
Height of substrate layer (H)	1.27

3.3.   Low Profile Antenna Backed by a Non-Tunable HIS

In this section the development of a series of low profile non-tunable antennas backed with HIS using different unit cell geometries are presented. A comparison between the different types of antennas is also shown.

3.3.1. Jerusalem Cross

In this section a low-profile planar antenna operating at 2.45 GHz with uni-directional radiation is presented. The approach herein was to integrate and ELPOSD into a multi-layer substrate that includes a back ground-plane and an intervening high-impedance, frequency selective surface (FSS) layer. The Jerusalem Cross frequency selective surface (JC-FSS) geometry was selected for the FSS layer, due to its wide angular stability and the potential for convenient frequency tuning and substrate thickness reduction. Previous authors have investigated the combination of an ELPOSD with patch-type electronic band-gap (EBG) layers [14], [65].

A JC-FSS cell consists of a pair of center-connected crossed dipoles terminated with end loading plates, and in the presented design this metal pattern is sandwiched between two dielectric layers. A ground plane is present at the bottom surface. The inclusion of the superstrate in the derivation of the FSS affects its performance by adding capacitance from the grid, due to the increased value for the effective permittivity. The JC-FSS can be effectively modeled by a parallel resonant LC circuit as shown in Figure 3.9. The LC model consists of the parallel combination of the self-resonant grid impedance (Z_g) which represents a strip, with the grounded dielectric slab impedance (Z_d). The resonant frequency can then be calculated by equating the denominator from (3.1) to zero.

$$ f_{r(\omega)} = \frac{1}{2\pi \sqrt{(L_d + L_g)(C_g)}} \tag{3.1} $$

The initial dimensions for the JC-FSS are obtained by implementing the closed form equations from [66] to get initial cell dimensions. From here, the JC-FSS is brought into Ansoft HFSS and optimized for zero phase reversal for the reflection coefficient (Γ) at 2.45 GHz. Figure 3.10 shows the resulting dimensions for the optimized FSS. As noted above, the dielectric layers above and below the JC-FSS have a relative permittivity of 10.2 and a thickness of 1.27 mm. As demonstrated by [67], a high dielectric constant is preferred for low resonant frequencies to achieve better angular stability. Also, a small gap between crosses contributes more edge capacitance (C_g) which increases the equivalent surface impedance and reduces the size of the unit cells; the gap dimension used here was 0.32 mm. Having larger substrate heights and higher values of the dielectric constant, also contributes to achieving miniaturization of the unit cell. In this case, height and planar size reduction is obtained by capacitive and dielectric loading.

33
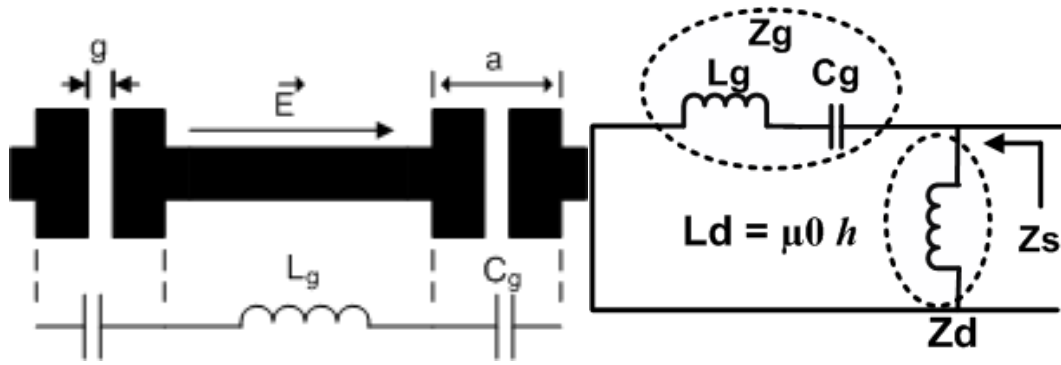
Figure 3.9: Equivalent circuit for the self-resonant grid (left) and series combination of the self-resonant grid with the dielectric slab impedance (right) of a JC unit cell.
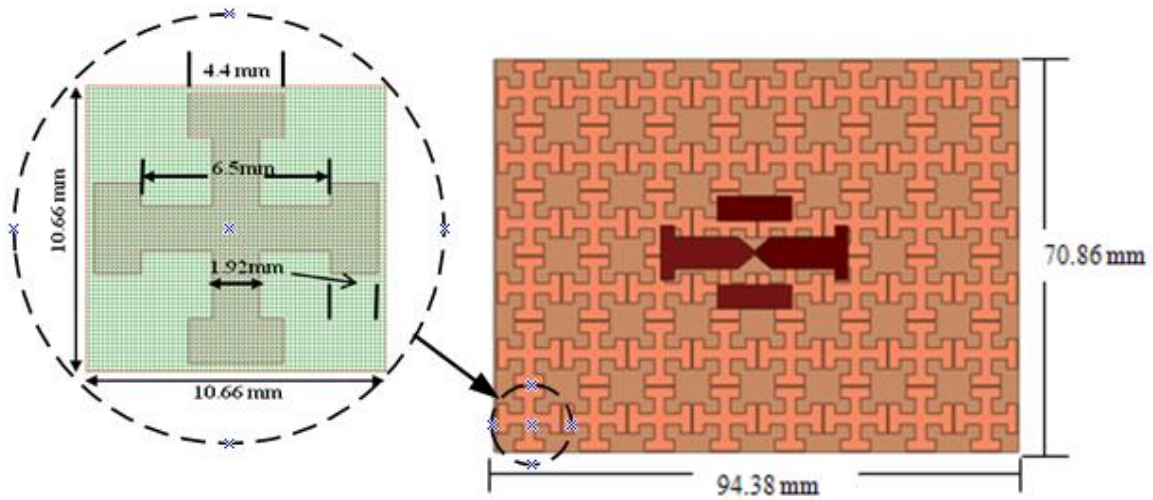
Figure 3.10: ELPOSD over a JC-FSS Layer.

The simulated E-plane and H-plane radiation patterns at 2.45 GHz for the ELPOSD are plotted in Figure 3.11(a) and Figure 3.11(b), respectively. The corresponding measured radiation patterns are shown in Figure 3.11(c) and Figure 3.11(d). The measured gain is ~3.5 dB and the front-to-back ratio is 15dB. The measured return loss is ~30dB at 2.45 GHz (Figure 3.12) demonstrating a 10 dB return loss bandwidth of 30 MHz.

34
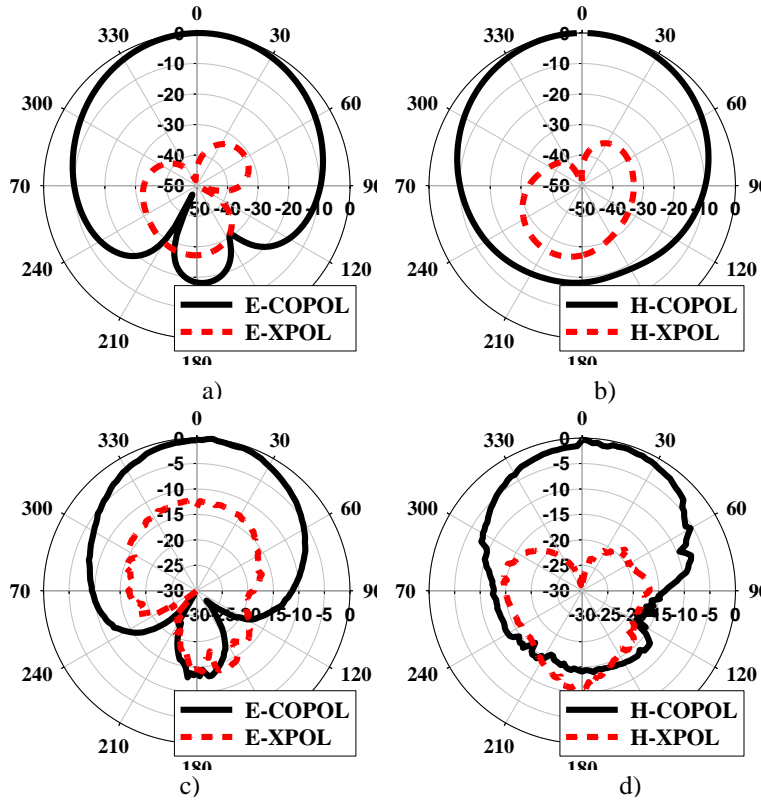
Figure 3.11: Simulated (a, b) and Measured (c, d) E-plane and H-plane radiation pattern for the ELPOSD at 2.45 GHz over the JC-FSS.
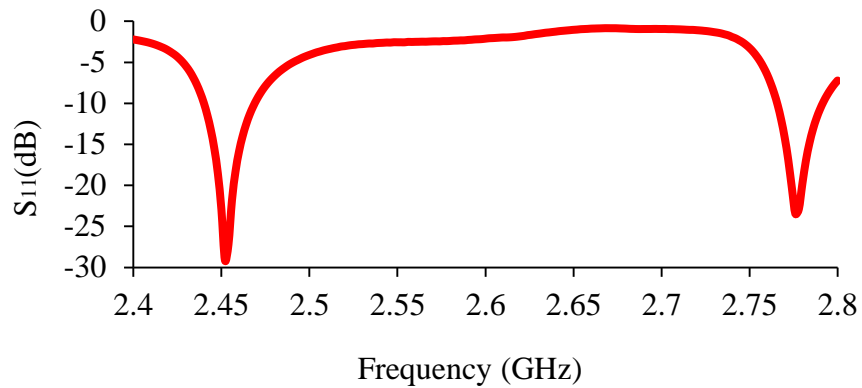
Figure 3.12: Measured S_{11} for the ELPOSD over the JC-FSS.

3.3.2. Square Patch

In the following section a comparison of the simulated performance between JC and square patch (SP) unit cells is shown, along with the design and fabrication of four antennas

backed by different FSS structures. It was observed that the return loss of the antenna is better behaved (i.e., with less ripples across the frequency range) for the SP-FSS than for the JC-FSS. For both FSS designs, increasing the number of unit cells improves the fractional bandwidth. The number of unit cells was increased from 48 to 80 for the JC-FSS and from 24 to 48 for the SP-FSS. Due to the larger size of the SP unit cell compared to that of the JC unit cell, a larger increment in the overall area was obtained for the SP design when increasing the number of unit cells. Thus a compromise between bandwidth and physical footprint is needed when deciding upon the FSS design.

Similar to the JC-FSS, the SP-FSS can also be modeled by a parallel LC circuit using the same equations as before; however the grid impedance will be dominated by the grid capacitance (C_g) as shown in Figure 3.13. Due to the SP-FSS having less grid inductance, the size of the patch needs to be increased in order to achieve lower resonance frequencies (3.1).
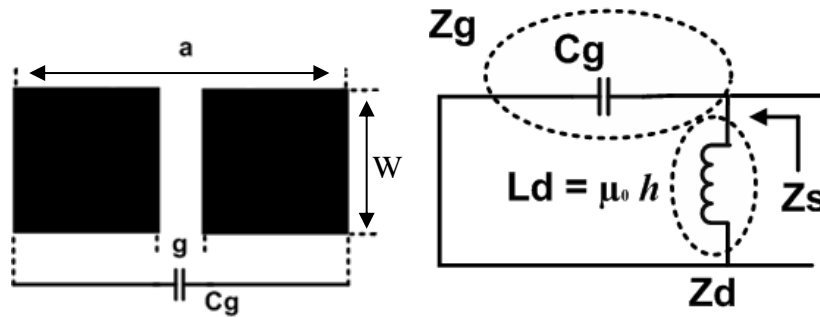
Figure 3.13: Equivalent circuit for the self-resonant grid (left) and series combination of the self-resonant grid with the dielectric slab impedance (right) of a SP unit cell.

The phase of the reflection coefficient is an important parameter to evaluate the performance of FSS structures. Figure 3.14 shows the reflection coefficient phases of the SP and JC unit cells. When the impedance of the FSS surface is low, the reflection phase is +/- 180° and when the impedance of the surface is high, the reflection phase is close to zero degrees. The fact

36

that the image currents on the FSS are more in-phase than out-of-phase when the reflection angle falls between ±90°, has been used to date as the criterion by which the "bandwidth" of the FSS was defined. However, a more rigorous criterion would be to consider the bandwidth of the FSS between ±45°. Equation (3.2), derived in detail in [66], gives the bandwidth over which the phase of the reflection coefficient falls between ± 45° (A detailed derivation of these formulas is shown in Appendix A and Appendix B).

$$BW = \frac{\pi}{4\eta_0} \sqrt{\frac{(L_d + L_g)}{C_g}} \times \left(\frac{L_d}{L_d + L_g}\right)^2 \qquad (3.2)$$

The results in Table 3.4 show an improvement of 75% in fractional bandwidth (%BW) by using the SP instead of the JC geometry on a 1.27 mm substrate thickness. However, a unit cell size reduction of 22% for the JC with respect the SP is achieved.
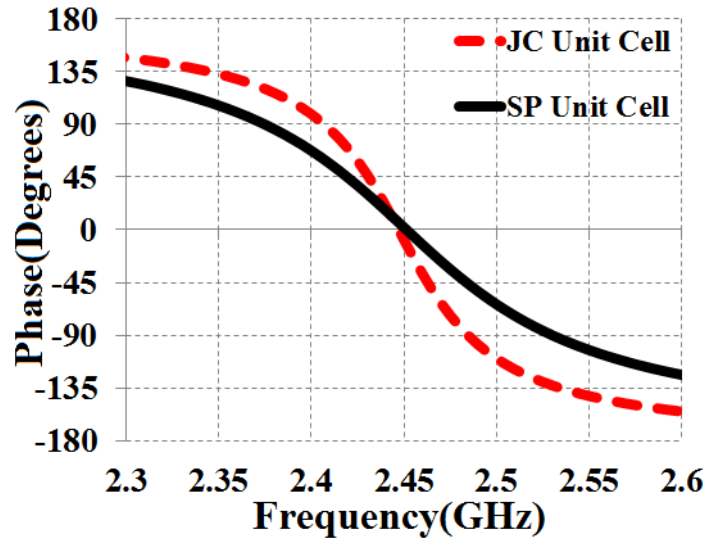
Figure 3.14: Reflection coefficient phase for a representative SP FSS and JC FSS.

The magnitude of the reflection coefficient is shown in Figure 3.15. The optimum reflection coefficient is $\lvert 1 \rvert \llcorner 0^0$ because the reflected wave is added constructively to the incident wave at the antenna layer. In terms of a design criterion, the magnitude of the reflection coefficient is usually required to be $> \lvert 0.8 \rvert$, which corresponds to the minimum value for effective FSS operation [66]. The SP has higher values in the magnitude of the reflection coefficient than the JC as indicated in Table 3.4.
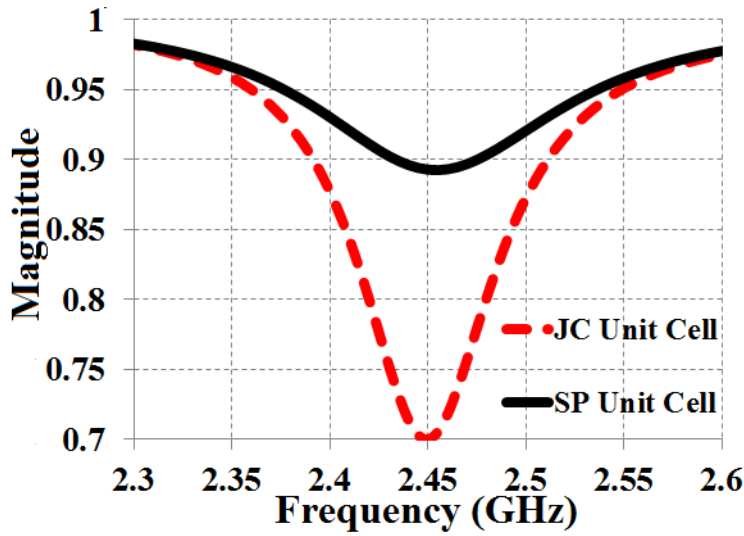
Figure 3.15 -Reflection coefficient magnitude for a representative SP FSS and JC FSS.

Table 3.4: Comparison between SP and JC unit cells.

Cell type	SP	JC
Substrate thickness t (mm)	1.27	1.27
Unit Cell Length (mm)	15.1	11.76
Unit Cell Length reduction (%)	----	22
Unit Cell Area (mm^2)	228	131.3
Unit Cell Area reduction (%)	----	42.2
Unit cell BW (%) (±90°)	2.45	1.43
Min $\lvert \Gamma \rvert$	0.9	0.7

3.3.2.1. Materials and Fabrication

Two different antennas were designed (design A and design B) using a 1.27 mm-thick Rogers® RT6010 substrate, with a dielectric constant of 10.2, that is supported by the FSS layer of the same thickness and dielectric constant. Design A uses a JC-FSS layer and Design B a SP-FSS. The dipole and balun were optimized to be within the range of 2 GHz to 3 GHz, and their dimensions were kept the same for both designs. The height (h) for each substrate is relatively thick (1.27mm) in order to increase the inductance (L_d) of the equivalent surface impedance Figure 3.13. The resulting total antenna thickness (excluding the feed layer) is ~λ/50.

3.3.2.2. Design A – JC-FSS Layer

The JC-FSS layer was designed at a center frequency of 2.45 GHz. The total unit cell length is 11.76 mm. Figure 3.16 shows the resulting dimension for the JC-FSS and ELPOSD. The blue crosses correspond to the initial antenna design which is backed by 48 unit cells, and the red crosses were added to represent the increase in the number of cells to 80. When a unit cell is designed, periodic boundary conditions and PML, which takes in account an infinite number of cells, are assumed [6]. The behavior of the actual antenna therefore approaches the ideal performance as the number of unit cells is increased. The simulation results in Figure 3.17 show that by adding 32 cells, the fractional bandwidth is increased from 0.8 % to 1.87% (Table 3.5); however the area increases by 66%.
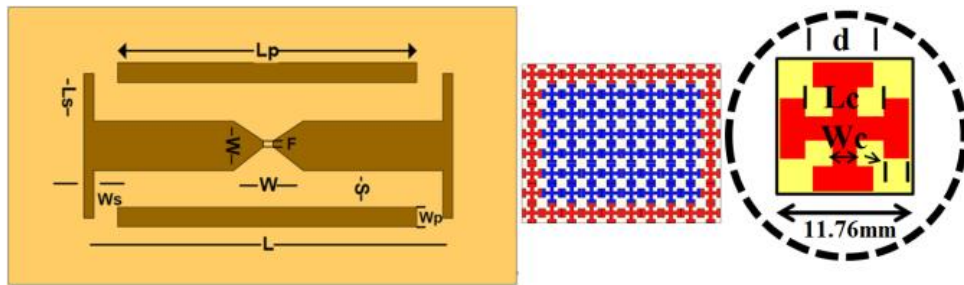
Figure 3.16: ELPOSD geometry backed by a JC-FSS (L=35, Lp=11, Ls=1.99, W=19, Wp=10, Ws=2.35, S=1.5, F=0.6 (mm)). Cell Size 11.76 mm, d=5.35, Lc=7.5 mm, Wc=1.98 (mm).
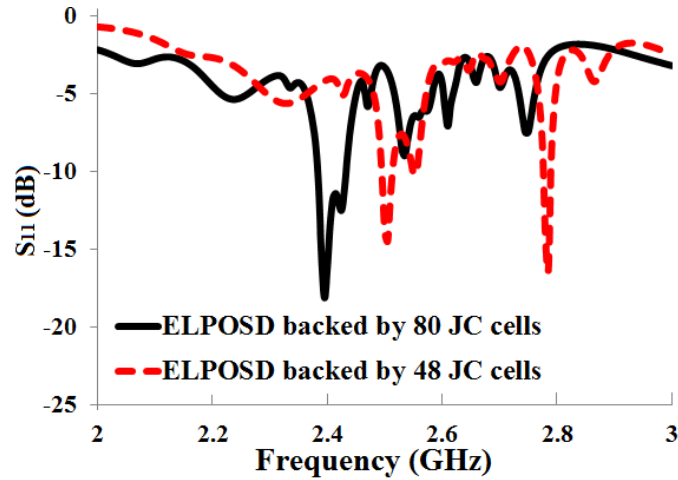
Figure 3.17: Simulated S_{11} of the antenna when backed by a JC-FSS using 48 and 80 cells.

Table 3.5: ELPOSD backed by JC-FSS.

Unit cells	Planar Dimensions (mm)	Area (mm^2)	Simulated BW (%)	Area Increment (%)
48	95x71	6745	0.8	-
24	118x95	11210	1.87	66

3.3.2.3.   Design B – SP-FSS Layer

The SP has a length of 14 mm. The distance *a* between adjacent elements was selected to be 0.9 mm to avoid shorting the vias in the feedline transition. The size of the ground planes for the JC and SP FSS are approximately equal. Figure 3.18 shows the resulting dimensions for the SP-FSS and ELPOSD. The blue crosses correspond to the initial antenna design when backed by 24 unit cells and the red crosses were added to represent the increase of the number of cells to 48.

The simulation results in Figure 3.19 show that by increasing the number of cells, the fractional bandwidth increased from 0.78 % to 2.62 % (Table 3.6). With the increase in the number of cells, the return loss improves. The two resonances formed when the antenna is

40

backed by 24 cells, at 2.55 GHz and 2.73 GHz are brought together creating a deeper and more broadband resonance at 2.65 GHz.
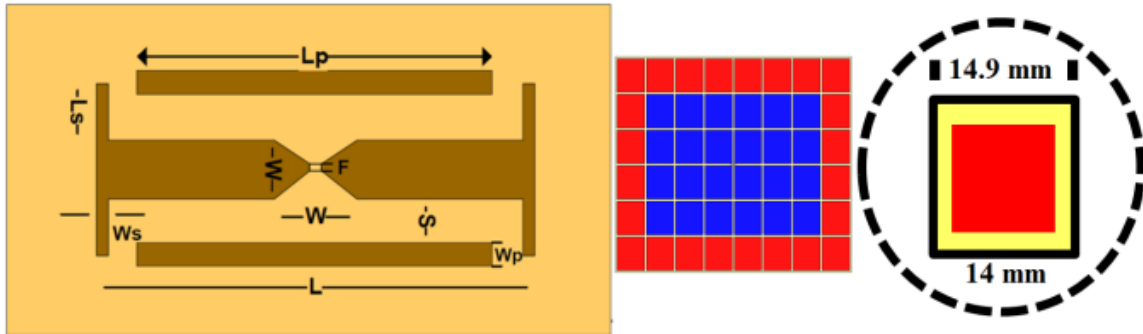
Figure 3.18: ELPOSD geometry backed by a SP-FSS (L=35, Lp=11, Ls=1.99, W=19, Wp=10, Ws=2.35, S=1.5, F=0.6 (mm)). Cell size 14.9 mm.
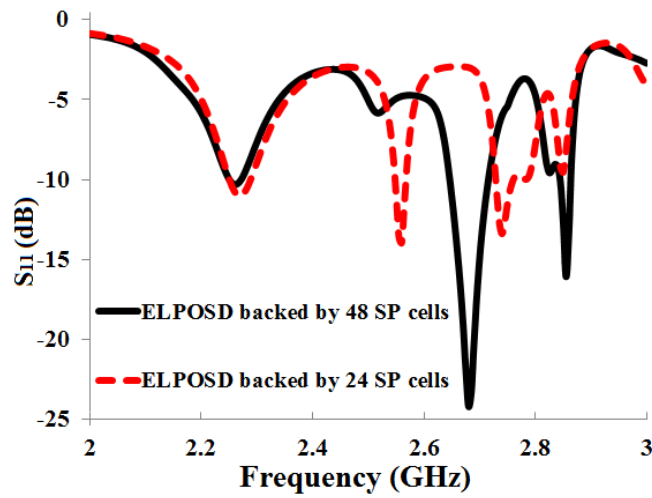
Figure 3.19: Simulated S_{11} of the ELPOSD when backed by an SP-FSS using 24 and 48 unit cells.

Table 3.6: ELPOSD backed by SP-FSS

Unit cells	Planar Dimensions (mm)	Area (mm^2)	Simulated BW (%)	Area Increment (%)
24	90x60	5400	0.8	-
48	120x90	10800	2.62	66

In Figure 3.20 and Figure 3.21 the measured performance is compared with the simulations. The return loss of the antenna shows fewer ripples when using the SP-FSS in comparison with the JC-FSS. This improvement can be attributed to the higher reflection coefficient magnitude provided by the SP FSS.
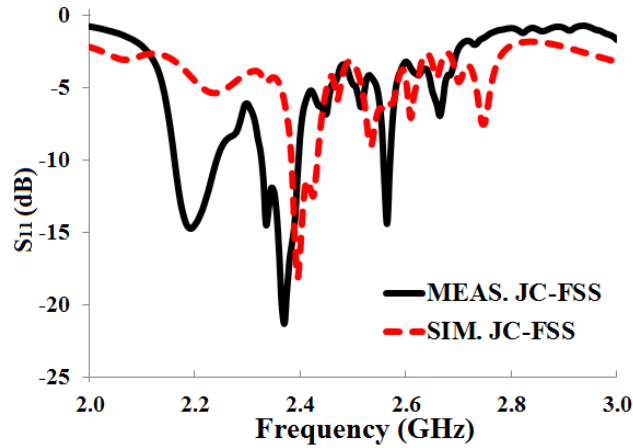
Figure 3.20: Simulated and measured S_{11} of the ELPOSD when backed by a JC-FSS using 24 and 48 unit cells.
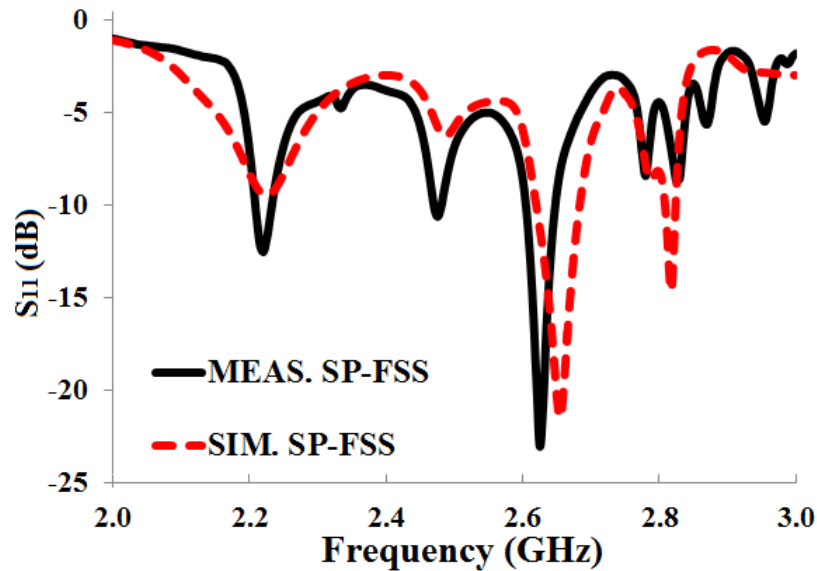
Figure 3.21: Simulated and measured S_{11} of the ELPOSD when is backed by SP-FSS using 48 unit cells.

The comparison of SP-FSS and JC-FSS with ELPOSD antennas has been presented. In comparing the performance of these two types of FSS structures, it was observed that the SP-FSS shows a better behavior (with less structure across frequency) than the JC-FSS from a return loss perspective. For both FSS designs, increasing the number of unit cells improves the fractional bandwidth. The bandwidth increased from 0.8% to 1.8% and from 0.8% to 2.7% for the JC and SP structures, respectively. Due to the larger size of the SP unit cell compared to that of the JC unit cell, a larger increment in planar size was obtained for the first. Thus a compromise between bandwidth and physical footprint is needed when deciding upon the FSS design.

3.3.3. Discrete Capacitor

In this section, the impact of adding discrete capacitive loading along one dimension of a FSS for low profile antenna applications is presented. The primary objective was to study the impact on antenna bandwidth and planar size when capacitive loading was introduced into the FSS. Based on section 3.3.2 results, the SP geometry was selected due to its better return loss performance and higher fractional bandwidth.

Two dipole antennas (Designs C and D) were designed using Rogers$^{®}$ RT6010 substrates, having a vendor-specified dielectric constant of 10.2. A high dielectric constant is preferred for low resonant frequencies to achieve better angular stability and smaller areal dimensions [67]. Design C uses 2.5 mm-thick boards for the FSS and the superstrate that supports the ELPOSD, while Design D uses 1.27 mm-thick boards. The height (h) for each substrate is relatively thick in order to increase the inductance (L_d) of the FSS impedance [45]. Both antennas were designed and tested with and without the capacitive loading in order to have a useful benchmark for the loaded designs. The antennas are fed using the balun presented in section 3.2.3.

43

The resulting total antenna thickness for the capacitively-loaded designs (excluding the feed layer) is $\sim\lambda/22$ for Design C and $\sim\lambda/40$ for Design D; this measurement includes a 0.8 mm air gap between the top of the FSS layer and the superstrate, to accommodate the capacitor height. For the unloaded designs, the total thickness values are $\lambda/25$ and $\lambda/50$, since there is no air gap.

Chemical etching was used to fabricate the antennas making the best effort to maintain a tight tolerance on the dimensions. This is important given that the performance of the FSS is quite sensitive to dimensional variations, especially the spacing between unit cells. This fact is illustrated in Figure 3.22, which shows the variation in the phase of the FSS reflection coefficient due to a change in the spacing from 0.9 mm to 0.95 mm.
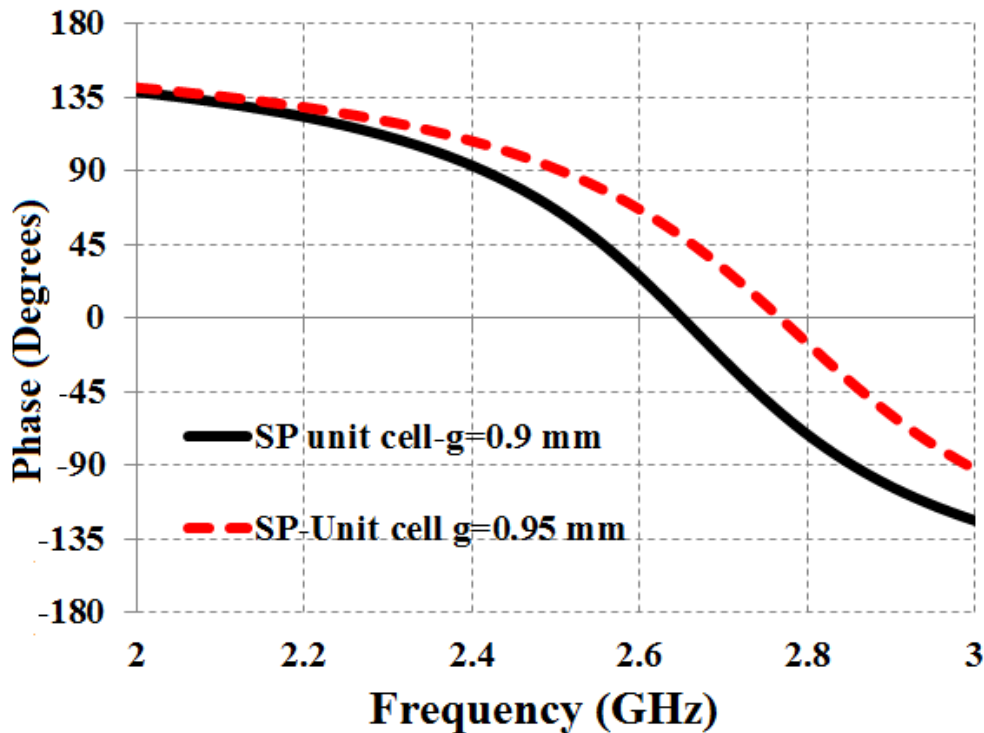
Figure 3.22: Reflection coefficient phase for a representative SP FSS when the unit cell spacing (g) varies by 0.05 mm.

44

3.3.3.1. Design C -2.5 mm-Thick Substrate/Superstrate

The simulated and measured return losses for the non-loaded Design C antenna are presented in Figure 3.23. The measured bandwidth around the 2.6 GHz design frequency is 5.3% and the measured gain is 4.9 dB. This design has a size of 110 mm x 80 mm.
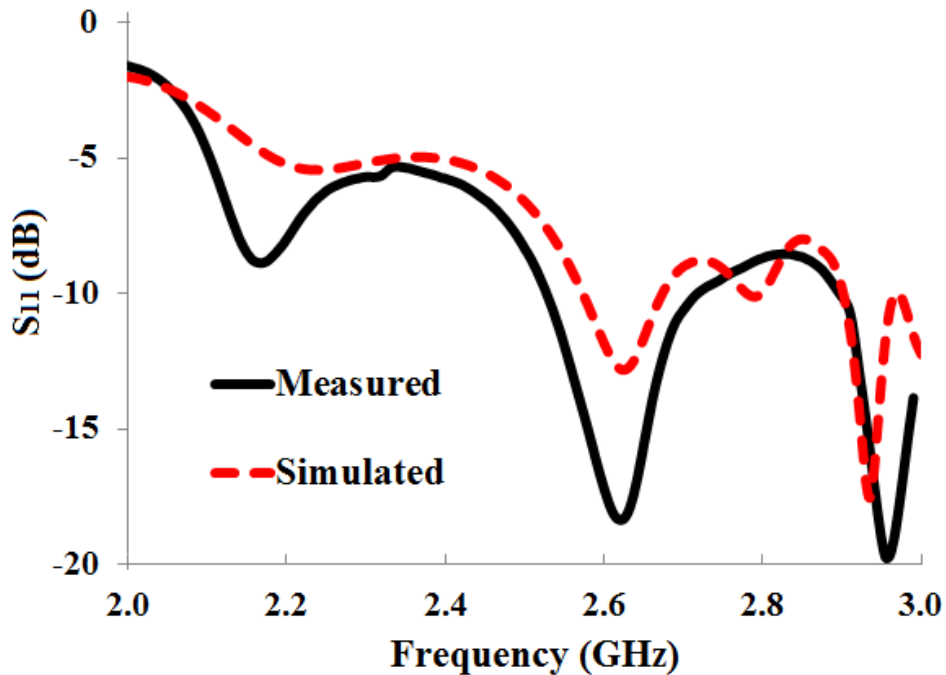
Figure 3.23: S_{11} when Design C is backed by non-loaded FSS.

Introduction of the capacitive-loading produces changes in various dimensions of the antenna. In the case of Design C, the FSS unit cell and overall grid size were changed while the ELPOSD dimensions remained the same. Figure 3.24 illustrates the ELPOSD, unit cell and grid, while Figure 3.25 compares the FSS grids for the two versions of Design C. The planar size of the loaded grid is 70 mm x 56 mm, which is 55% smaller than the non-loaded version. This size reduction results primarily from the need to use fewer unit cells in the loaded design to achieve comparable return loss characteristics.

The characterization of the loaded FSS unit cell was performed assuming periodic boundary conditions and perfectly matched layers. The reflection coefficient phase for two values of discrete lumped capacitance is shown in Figure 3.26. The ±90° bandwidth is ~300 MHz and ~500 MHz for 0.7 pF and 0.3 pF capacitors, respectively. The capacitor values of 0.7 pF and 0.3 pF were selected as these correspond to the capacitance limits within which the varactor diode is tunable.
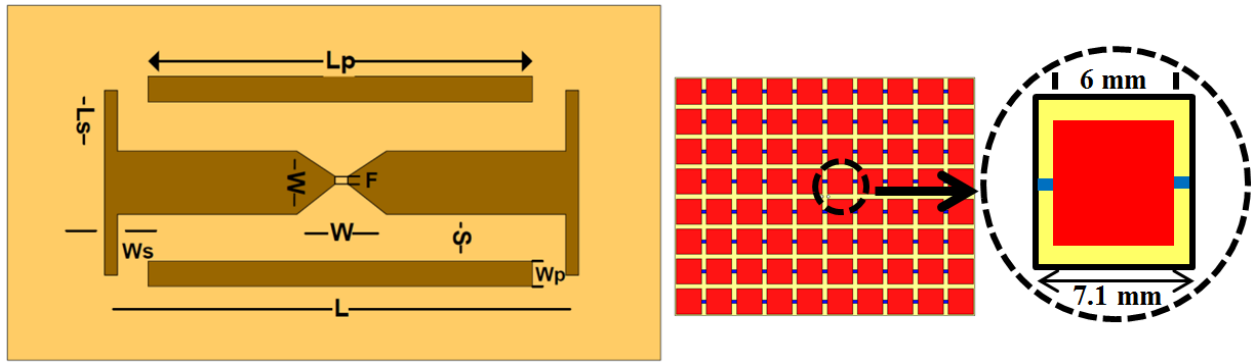
Figure 3.24: Design C ELPOSD over capacitively-loaded FSS. ELPOSD geometry: L=31.5, Lp=11, Ls=1.99, W=10, Wp=10, Ws=2.35, S=1 F=0.5 (all in mm); Cell Size: 7.1 mm.
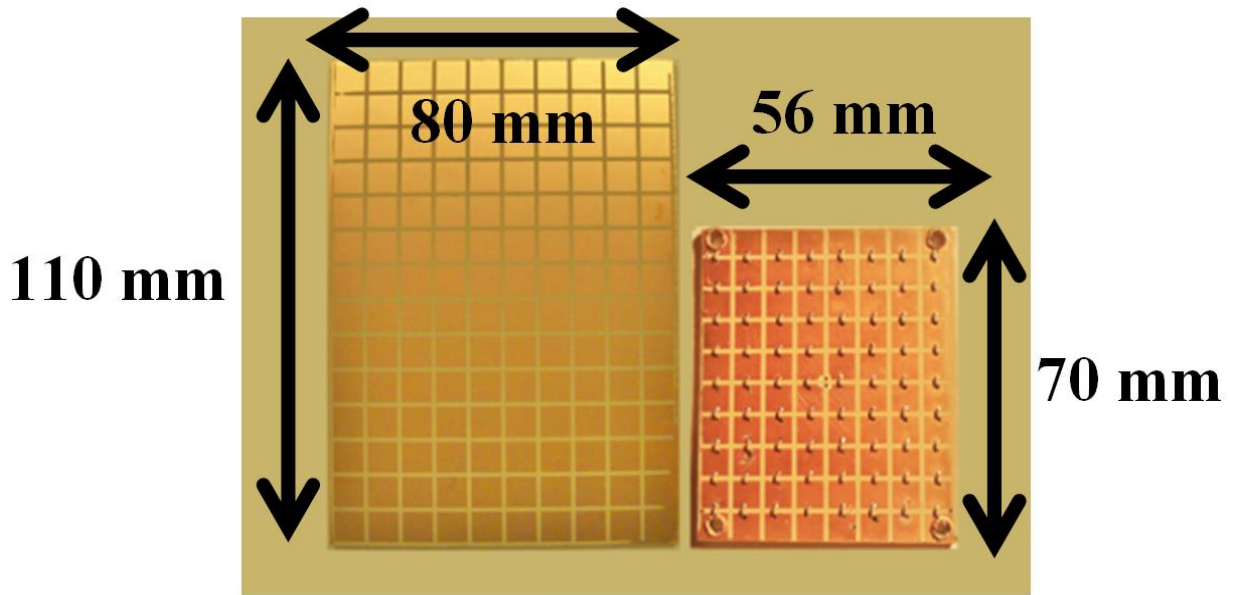
Figure 3.25: Design C: non-loaded FSS (left) and loaded FSS layer (right).

The behavior of the antenna return loss when using different capacitance values gives some measure of the potential for a frequency-tunable design. Simulated and measured S_{11} data for Design C using 0.3 pF and 0.7 pF loading capacitors are shown in Figure 3.27. Using the 10 dB return loss criterion, there is a 670 MHz span between the low end of the response with 0.7 pF capacitors and the high end of the response using 0.3 pF capacitors. This span correlates well with the results in Figure 3.26, particularly the $\pm 45^{\circ}$ boundaries. Consistent with (3.1) and (3.2) it is seen that by increasing the grid capacitance the resonance frequency and bandwidth decrease.
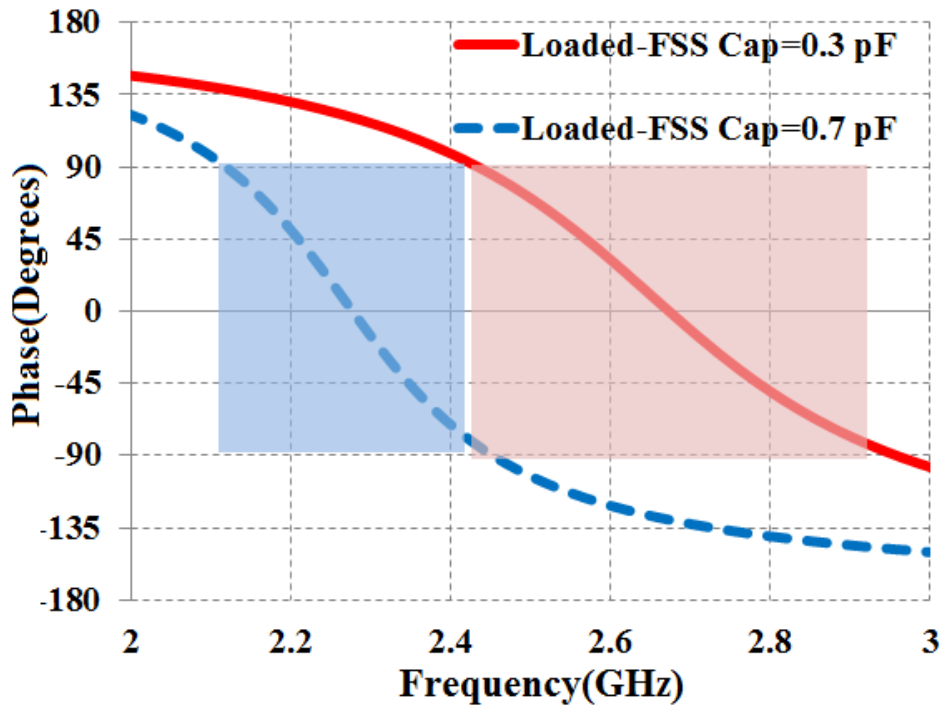
Figure 3.26: Reflection coefficient phase for a loaded FSS with capacitance values of 0.3 pF and 0.7 pF.

A summary comparison between the non-loaded and loaded versions of Design C is given in Table 3.7. With the 0.3 pF capacitors, the 10 dB return loss bandwidth is 7.3% for the simulated and experimental data. Using the 0.7 pF capacitors the simulated bandwidth is ~6.5%;

the smaller measured bandwidth of 3.6% may be the result of tolerances involved with the assembly of the antenna.
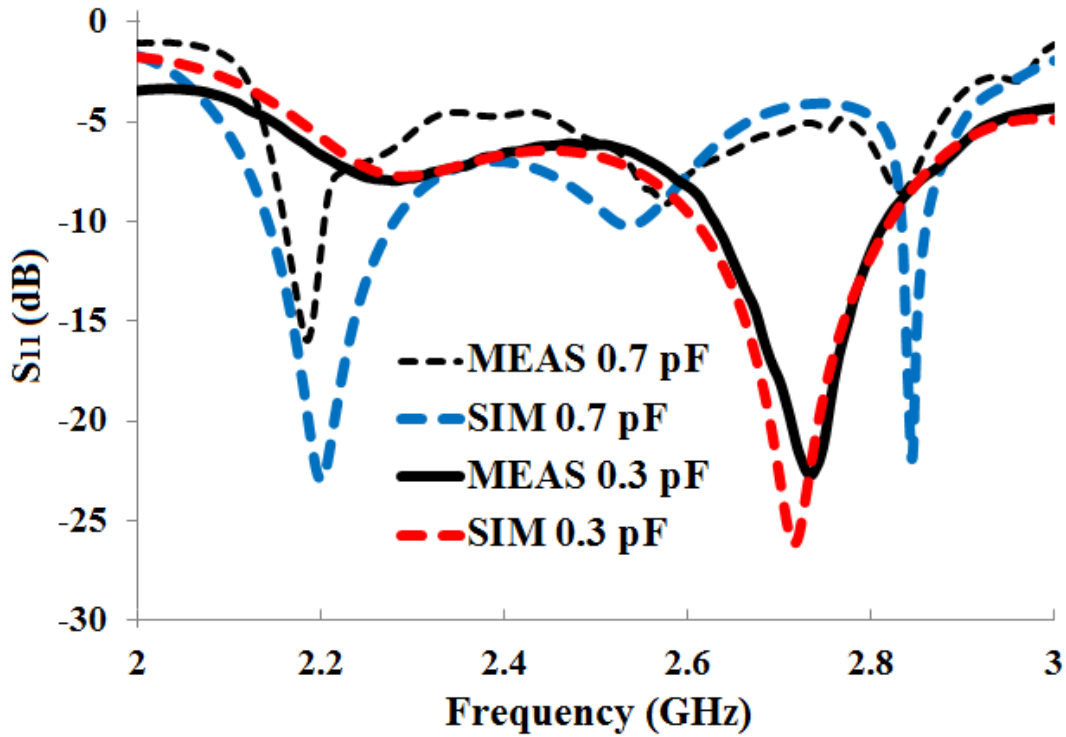
Figure 3.27: S_{11} when the Design C ELPOSD is backed by a loaded FSS.

Table 3.7: Experimental characteristics design C.

Capacitive loaded	Capacitance Value (pF)	Unit cells	Planar Dimensions (mm)	BW (%)	Area reduction (%)
NO	N/A	140	110 x 80	5.6	-
YES	0.3	72	70 x 56	7.3	55
YES	0.7	72	70 x56	3.6	55

3.3.3.2. Design D – 1.27 mm-Thick Substrate/Superstrate

A similar comparison as that presented above was performed for Design D without and with capacitive loading. For the non-loaded design the planar size was 120 mm x 90 mm and the

measured fractional bandwidth was 1.6% (Figure 3.28). The loaded version was tested using 0.3 pF and 0.7 pF capacitors, with center frequencies of 2.8 GHz and 2.54 GHz, respectively. In this case the dimensions of the dipole, unit cell and grid (Figure 3.29) were all slightly different from those of the non-loaded design. To maintain comparable return loss characteristics over frequency, equal numbers of unit cells were used for the two versions.
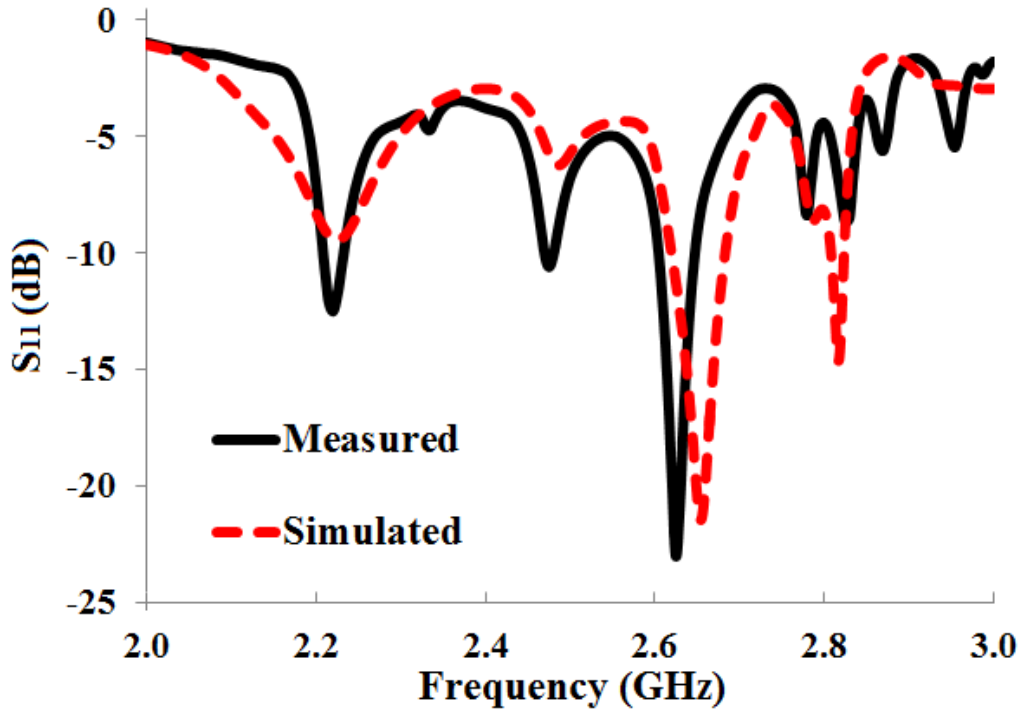
Figure 3.28: S_{11} when the Design D ELPOSD is backed by a non-loaded FSS.

The simulated and measured S_{11} for the two loaded cases are compared in Figure 3.30. As before, there is significant tunability in the frequency response using the different capacitance values. The measured bandwidths for 0.3 pF and 0.7 pF loading are 9.2% and 8.4%, respectively. The simulated bandwidth is somewhat smaller in each case, and the discrepancies are suspected to be related to fabrication tolerances (i.e. capacitor tolerances, air gaps between layers, etc.). The comparison between the non-loaded and loaded designs is summarized in Table 3.8 and Figure 3.31.
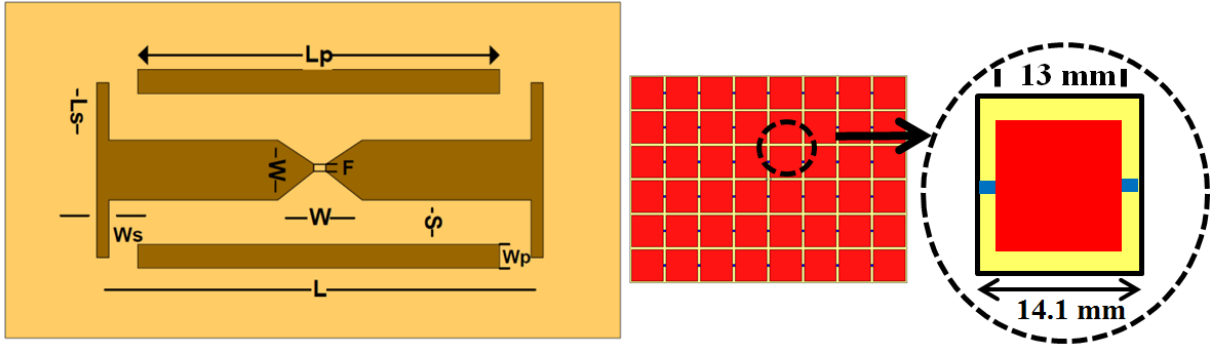
Figure 3.29: Design D ELPOSD over capacitvely-loaded FSS. ELPOSD geometry (L=35, Lp=11, Ls=1.99, W=10, Wp=10, Ws=2.35, S=1.5 F=0.5 (mm)). Cell Size 13 mm.
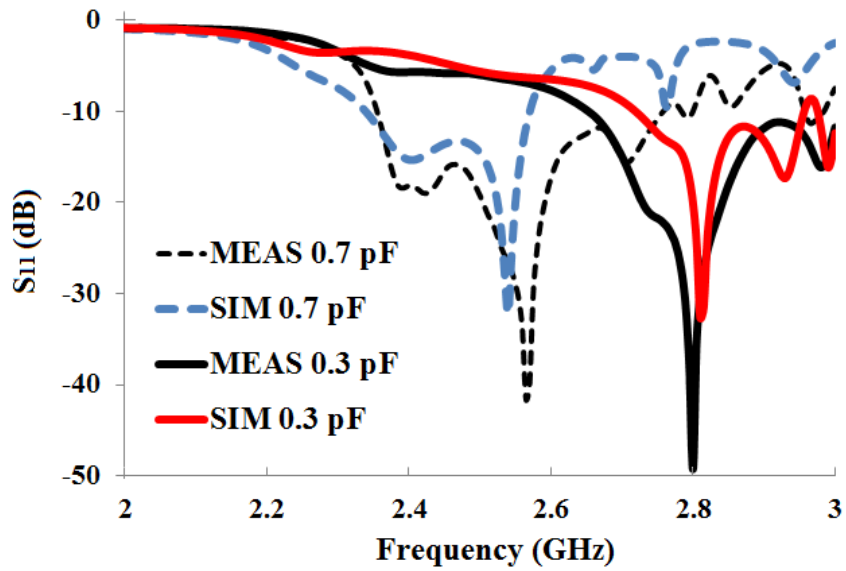
Figure 3.30: Simulated and measured S_{11} when Design D is backed by a loaded FSS.

Table 3.8: Experimental characteristics design D.

Capacitive loaded	Capacitance Value (pF)	Unit cells	Planar Dimensions (mm)	BW (%)	Area reduction (%)
NO	N/A	48	120 x 90	1.6	-
YES	0.3	48	112 x 85	9.2	12
YES	0.7	48	112 x85	8.4	12
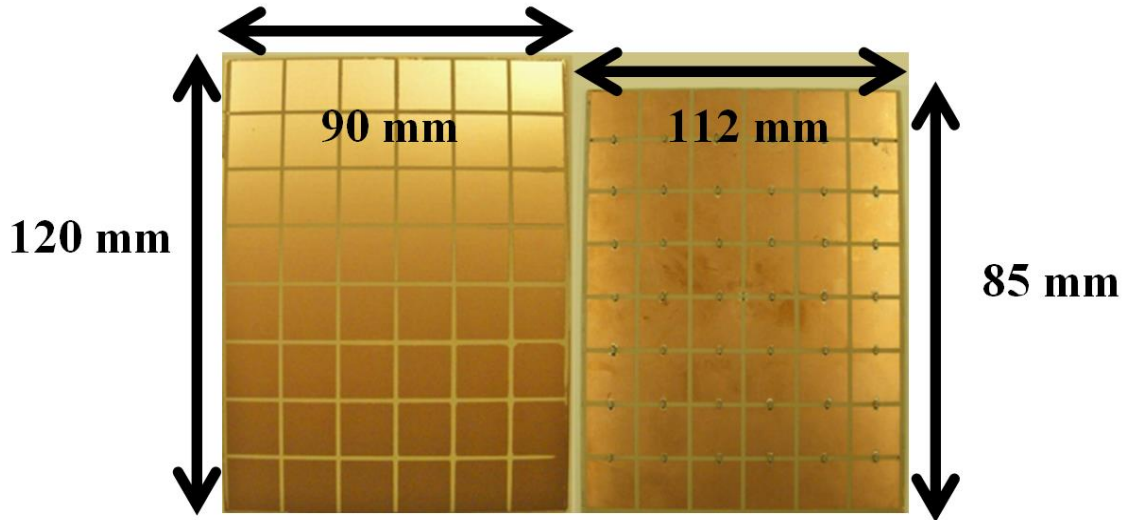
Figure 3.31: Design D: non-loaded FSS (left) and loaded FSS layer (right).

For completeness, measured E-plane radiation patterns for Design D using 0.7 pF and 0.3 pF loading capacitors are shown in Figure 3.32 at 2.2 GHz and 2.8 GHz, respectively. The measured gain at the aforementioned frequencies was 4.1 dB and 3.8 dB, respectively.
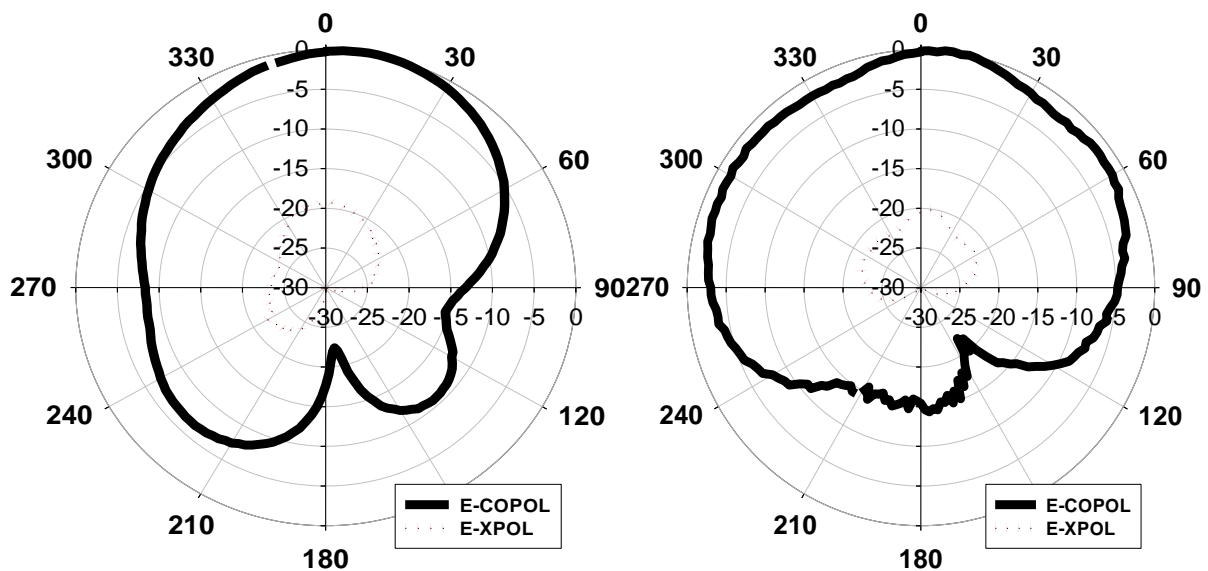
Figure 3.32: Measured E-plane radiation pattern for Design D using 0.7 pF loading capacitors at 2.2 GHz (left) and 0.3 pF loading capacitors at 2.8 GHz (right).

3.4.   Conclusion

A series of antenna architectures have been designed, built and compared against each other. The first generation of the antenna, using Jerusalem crosses (JC) as the FSS structure (non-tunable symmetrical HIS), showed a fractional bandwidth of 1.41%. The need to increase the bandwidth suggested research into alternative FSS structures. The second generation of the antenna showed an increase in the fractional bandwidth from 1.4% to 2.68% when a SP-FSS (non-tunable symmetrical HIS) was used as a cell structure. The third generation using discrete capacitors (non-tunable asymmetrical HIS) demonstrated comparable performance between a non-loaded and a capacitively-loaded FSS with a significant reduction in the number of cells and/or cell geometry size. The provision of discrete capacitive loads reduced the FSS susceptibility to fabrication tolerances based on placement of a fixed grid capacitance. The bandwidth increased from 1.5% to 9.2% for a thickness of $\sim\lambda/40$. The total antenna area was reduced by 12% [45]. In the next chapter the design and fabrication of low profile tunable antennas using discrete varactors is shown.

CHAPTER 4: END-LOADED PLANAR OPEN SLEEVE DIPOLE BACKED BY ELECTRONICALLY-TUNABLE HIGH IMPEDANCE SURFACES

4.1. Introduction

In this chapter a theoretical and experimental study on low profile, 2.4 GHz dipole antennas that uses a frequency selective surface (FSS) with varactor-tuned unit cells is presented. The tunable unit cell is a square patch with a small aperture on either side to accommodate the varactor diodes. The FSS was built using semiconductor commercial varactors and in-house fabricated BST devices. An analytical circuit model for an electrically asymmetric tunable unit cell is shown. The BST Varactor development is also explained. It is shown that these types of antenna can be tuned for optimal performance even in the presence of a human core body phantom. The total thickness of the antennas is approximately $\lambda/45$.

4.2. Low Profile Tunable Dipole Antenna Using Semiconductor Varactors

In this section an end-loaded planar open sleeve dipole (ELPOSD) antenna backed with an electronically-tunable frequency selective surface (FSS) is presented (Figure 4.1). In this design, varactor-loaded asymmetric square-patch (SP) unit cells are used to affect tuning only along the direction that is parallel to the main axis of the dipole. The antenna is fed from beneath the ground plane through vias connected to a microstrip-to-coplanar strip balun [62], [63]. The FSS is sandwiched between two 1.27 mm-thick substrate layers, resulting in a total antenna thickness (excluding the feed layer) of $\sim\lambda/45$ at the operational central frequency of 2.4 GHz.
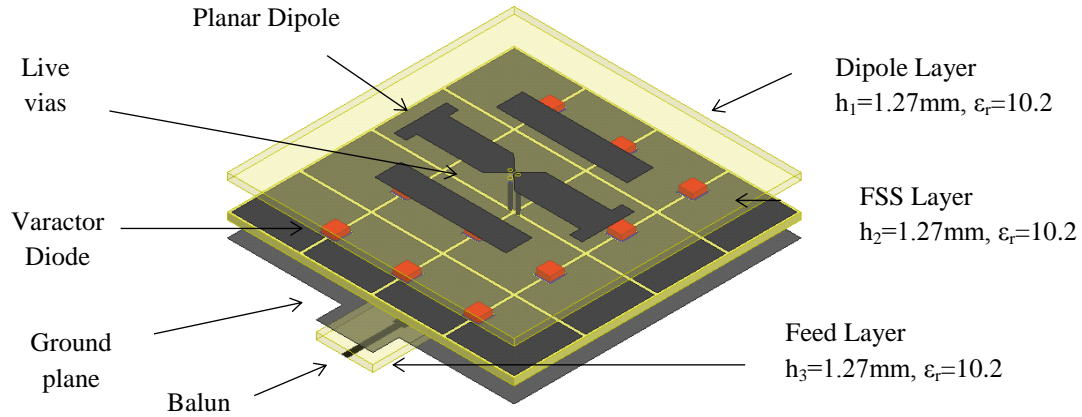
Figure 4.1: Isometric view of the antenna illustrating the multi-layer substrate with feed layer, tunable FSS layer, and dipole layer.

The primary features of the antenna design discussed in this section are the use of an FSS that does not include via connections to ground, its low profile characteristic, and potentially conformal nature. The significance of these features stems from the intended use of the antenna for biomedical radiometric sensing wherein the sensor may be embedded in uniforms, prosthetic devices, or other body-worn protection. For these applications low profile is desirable; ease of assembly and resulting flexibility of the multi-layer substrate configuration can be enhanced by reducing or eliminating the number of vias used. While the presented design is yet to be flexible or conformal, the topology has been developed with the aim of working towards a flexible design (see chapter 5).

Other important performance metrics for this application include high radiation efficiency and high front-to-back radiation pattern ratio. Reflections at the antenna input reduce the energy captured by the radiometer and also cause thermal noise produced by the receiver to be re-injected into the front-end. Dissipative losses in the antenna further reduce sensitivity by increasing the system noise temperature [68], [69]. To minimize back-side radiation, a ground plane is placed beneath the ELPOSD. It is well known that image current cancellation effects

54

due to the proximity of a ground plane to a dipole antenna result in poor radiation efficiency. Accordingly, the textured surface above the ground plane, i.e. the FSS layer, is used to alter the current distribution on the ground plane thereby mitigating the interference issues and improving radiation properties.

Finally, the tunable characteristic of the FSS introduced in this design helps to address another challenge of close-proximity radiometric sensing – that of the variable nature of the interface between the sensor and subject under test. Human body tissues such as muscle, skin, cortical bone, fat, etc., have been studied to determine their frequency dependent dielectric properties in [70]-[73]; for example, the relative permittivity for muscle, fat and cortical bone tissues varies approximately between 62-52, 11.5-10.5 and 13.5-11.8, respectively, within the frequency range of 700 MHz to 3 GHz. Naturally occurring variations in the permittivity of the composite tissue structure, which depend on the percentages of fat, bone and muscle, as well as variations in the separation distance between the sensor antenna and the tissue, can induce dramatic changes in the thermally-induced electromagnetic energy transfer between the patient (or subject) and the sensor. Furthermore, accurate interpretation of radiometric data obtained within a single frequency band is complicated by these same variations. A broadband or a multiband antenna with moderate instantaneous bandwidth enables maximum temperature resolution, which is critical in detecting subsurface emissions from internal tissue and organs [68]. Thus, the ability to dynamically adjust the center frequency and impedance match of the sensor antenna is desirable.

A broadband dipole over a tunable FSS is preferred over tunable frequency-agile patch antennas because greater fractional bandwidth can typically be achieved. The former have demonstrated fractional bandwidths of approximately 10%, while the latter have relatively

55

narrow instantaneous bandwidth, typically 5% or less [10]-[19]. The dipole approach can also be scalable to lower frequencies without significantly compromising the height and planar size of the antenna [15], [19]. In the following sections, a quasi-static analysis for the asymmetric tunable unit cell is presented, along with the design and fabrication of the antenna backed by the tunable FSS.

4.2.1. Tunable Unit Cell Model

A square patch unit cell was selected due to its inherently broad bandwidth, high value for the magnitude of the reflection coefficient and simplicity in the design [10]. The square patch unit cell is illustrated in Figure 4.2 The patch includes a centered aperture on either side to place the varactor diodes. The dimensions of the aperture were selected to fit the diode package and the distance between adjoining cells was kept at a minimum to achieve miniaturization. The total cell size is only 0.11λ at 2.5GHz, which is smaller than cells presented in previous works ([43], [45], [75]-[77]). The diodes were placed only in one direction (e.g., along the x-axis in Fig. 2) to reduce complexity in the DC bias network and avoid the need for vias.
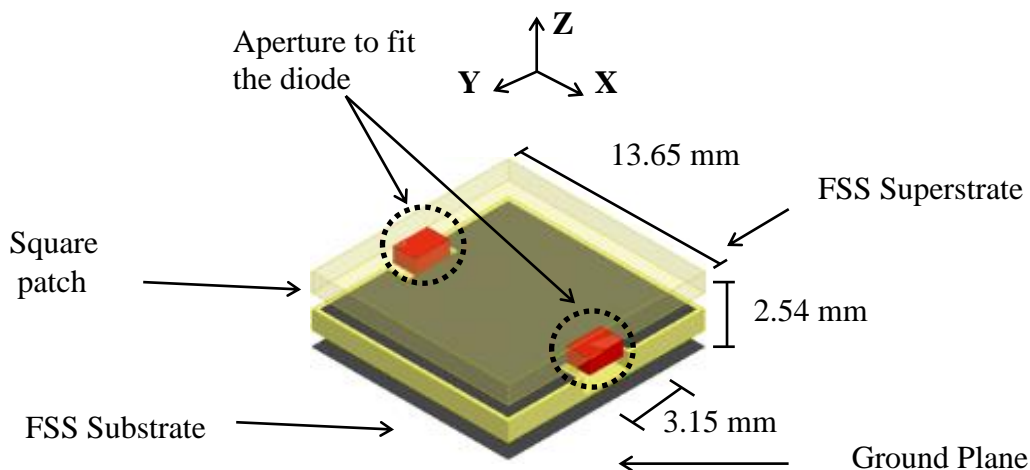
Figure 4.2: Isometric view with dimensions of the tunable unit cell sandwiched between two dielectric layers.

Several methods have been employed to analyze the characteristics of a symmetric FSS. The methods can be classified into three categories: lumped element models [66], periodic transmission line methods [74] and full wave numerical electromagnetic (EM) simulations [78]. The initial dimensions of the FSS unit cells were obtained using a lumped element model and closed-form equations from [66], [52]. The unit cell dimensions were then optimized using full-wave numerical EM simulation as discussed in [44] and [45] without consideration of the polarization properties of the antenna. This basic analysis approach can also be used for electrically asymmetric unit cells; however, the direction of the electric field relative to the unit cell orientation needs to be taken into account. The polarization aspect is critical to achieving higher tunability.

The reflection coefficient phase of capacitively-loaded symmetric and asymmetric structures when excited by a plane wave (normal incidence) is shown in Figure 4.3 and Figure 4.4, respectively. Here the capacitive loading emulates the effect of the varactor diodes. In Ansoft's High Frequency Structural Simulator (HFSS)the plane wave is generated by a Floquet port as the sum of two fields, a field that is transverse magnetic to z (TMz) polarized in the y direction and a second that is transverse electric to z (TEz) polarized in the x direction [79]. In the case of the symmetric unit cell, the reflection coefficient phase of each mode exciting the structure (TM and TE) shows a similar tuning range when the loading capacitance changes from 0.25 pF to 0.95 pF. In contrast, the x-oriented electrically asymmetric unit cell shows different tuning ranges for TE and TM modes. When the diodes are placed in the direction of the electric field (TE mode), higher tunability is obtained. This result follows naturally because the electric field across the gap on the varactor-loaded side of the patch is much higher.
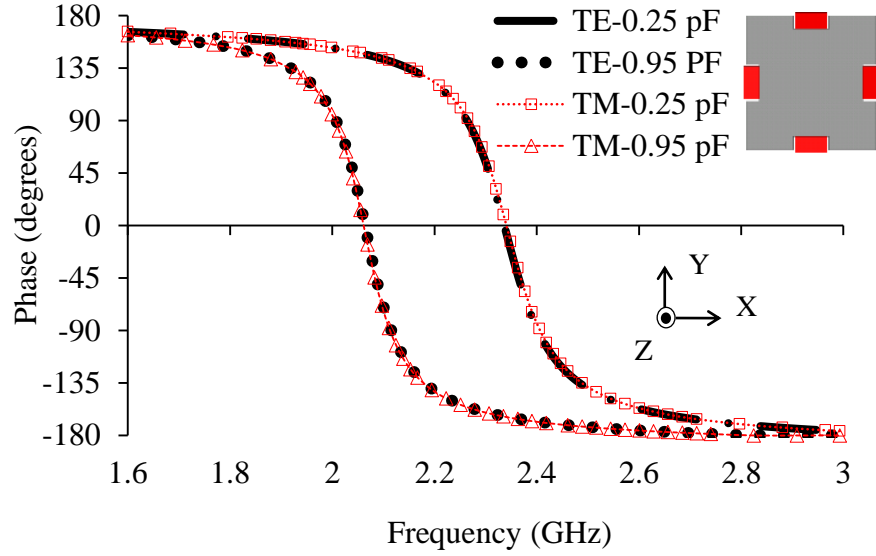
Figure 4.3: Simulated reflection coefficient phase for normal incidence on a capacitively-loaded symmetric unit cell.
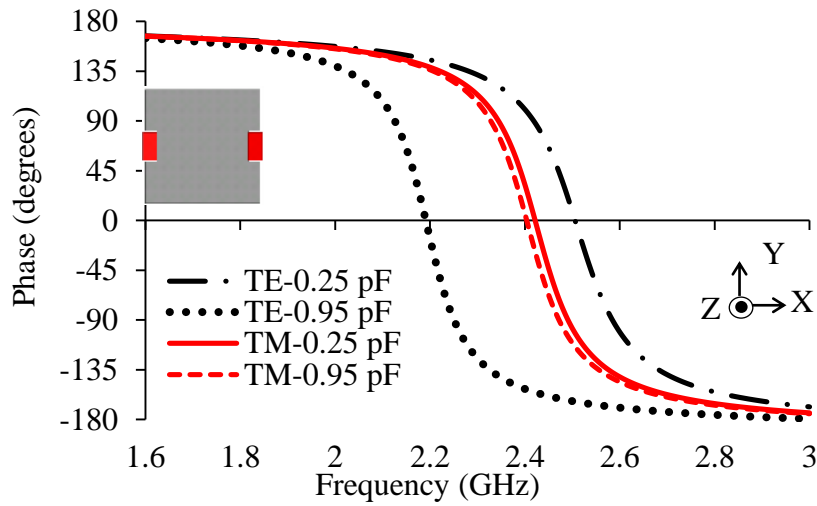
Figure 4.4: Simulated reflection coefficient phase for normal incidence on a capacitively-loaded asymmetric x-oriented unit cell.

The unit cell TE mode incidence can be modeled using a quasi-static circuit model approach. Herein the derivation of the equations associated with the direction where maximum tunability occurs is presented. A similar analysis can be used for the orthogonal direction.

58
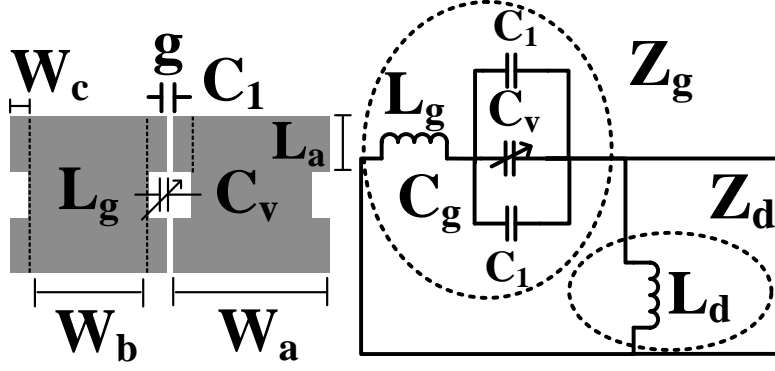
Figure 4.5: Equivalent circuit for the self-resonant grid (left) and series combination of the self-resonant grid with the dielectric slab impedance (right) of a tunable unit cell; Wa=13.05, Wb=10.5, Wc=1.275, La=4.725, g=0.6, periodicity (Wa+g) =13.65 (all units in mm).

The unit cell can be represented by a parallel resonant LC circuit as shown in Figure 4.5. The LC model consists of the parallel combination of the self-resonant grid impedance (Z_g) which represents a strip, with the grounded dielectric slab impedance (Z_d). Z_d is inductive (L_d) and it is calculated using [53]. Z_g can be expanded into the series combination of the strip impedance and the edge impedance between end loading plates. The latter is capacitive (C_1, Eqn. (4.1)) and is a result of the charge built up between these plates [52]. C_v is the effective capacitance of the varactor diode. Thus, the grid capacitance (C_g) is obtained by adding these three parallel capacitances (4.2).

$$C_1 = \frac{2L_a\varepsilon_0\varepsilon_{re}}{\pi}\cosh^{-1}\left(\frac{[W_a - W_b] + g}{g}\right)$$

(4.1)

$$C_g = 2C_1 + C_v$$

(4.2)

The strip impedance is mostly inductive (L_g) and is derived from the Telegrapher equations [53] or from the stepped- impedance equations in [66]. Due to discontinuity effects,

the inductance is determined most accurately if the dependence of the current distribution on the varactor capacitance value is taken into account. In this formulation, the difference observed for C_v below and above 0.6 pF was considered. If the value is less than 0.6 pF the current is distributed uniformly to the edges of the patch through capacitors C_1, due to the high varactor impedance. Conversely, for C_v values greater than 0.6 pF, the current tends to flow through the varactor. The behavior is demonstrated in Figure 4.6, which shows current distributions for various grid capacitance values, simulated at the frequency where the FSS reflection coefficient phase is equal to zero degrees. The equation for L_g is given in (4.3), using permittivity and characteristic impedance equations taken from [66]. The resulting equation for Z_g is given in (4.4).

$$L_g = 2Z_o \tan\left[\frac{\left(\omega\sqrt{\mu_0\varepsilon_0}\sqrt{\varepsilon_{re}}\right)W}{2}\right] \qquad \begin{aligned} W &= W_a \text{ if } C_v < 0.6 \, pF \\ W &= W_b \text{ if } C_v > 0.6 \, pF \end{aligned} \qquad (4.3)$$

$$Z_g = j\omega L_g + \frac{1}{j\omega C_g} \qquad\qquad (4.4)$$
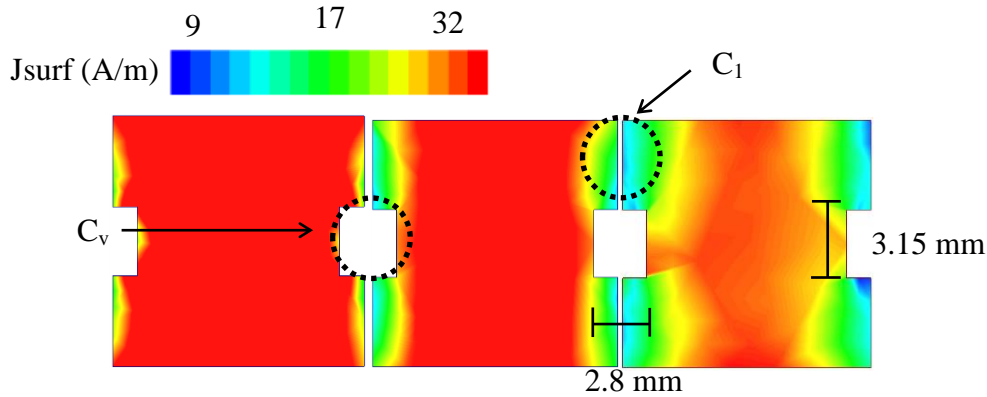
Figure 4.6: Surface current density distribution of the tunable unit cells for different capacitance values: C_v=0.25 pF (left), C_v=0.6 pF (center) and C_v=0.95 pF (right).

From the parallel LC circuit in Figure 4.5 the equivalent surface impedance Z_s is obtained by the parallel combination of the impedances Z_g and Z_d (4.5). The resonant frequency can then be calculated by equating the denominator from (4.5) to zero (4.6).

$$Z_s(\omega) = Z_g \parallel Z_d = j\omega L_d \frac{1 - \omega^2 L_g(2C_1 + C_v)}{1 - \omega^2(L_d + L_g)(2C_1 + C_v)} \tag{4.5}$$

$$f_{r(\omega)} = \frac{1}{2\pi\sqrt{(L_d + L_g)(2C_1 + C_v)}} \tag{4.6}$$

The reflection coefficient of a plane wave impinging upon the tunable unit cell is calculated using (4.7). The bandwidth is obtained by dividing the equivalent impedance of the FSS by the intrinsic impedance of the superstrate (4.8). This equation, derived in detail in [66], gives the bandwidth over which the phase of the reflection coefficient falls between $\pm 90^\circ$:

$$\Gamma(\omega) = \left[\frac{Z_s(\omega) - \frac{\eta_0}{\sqrt{\varepsilon_{re}}}}{Z_s(\omega) + \frac{\eta_0}{\sqrt{\varepsilon_{re}}}}\right] \tag{4.7}$$

$$BW = \frac{\pi\sqrt{\varepsilon_{re}}}{2\eta_0}\sqrt{\frac{(L_d + L_g)}{(2C_1 + C_v)}} \times \left(\frac{L_d}{L_d + L_g}\right)^2 \tag{4.8}$$

Figure 4.7 shows a comparison between the circuit model and the full-wave numerical electromagnetic simulation data. For low diode capacitance the current is distributed more uniformly in the unit cells and therefore higher accuracy of the circuit model and better matching to the numerical EM simulations is achieved. The agreement for the highest capacitance value is not as close, which is most likely explained by the less uniform current distribution across the

unit cell. Regardless, the equivalent circuit is a good approximation and provides an understanding of the behavior of this unit cell type.
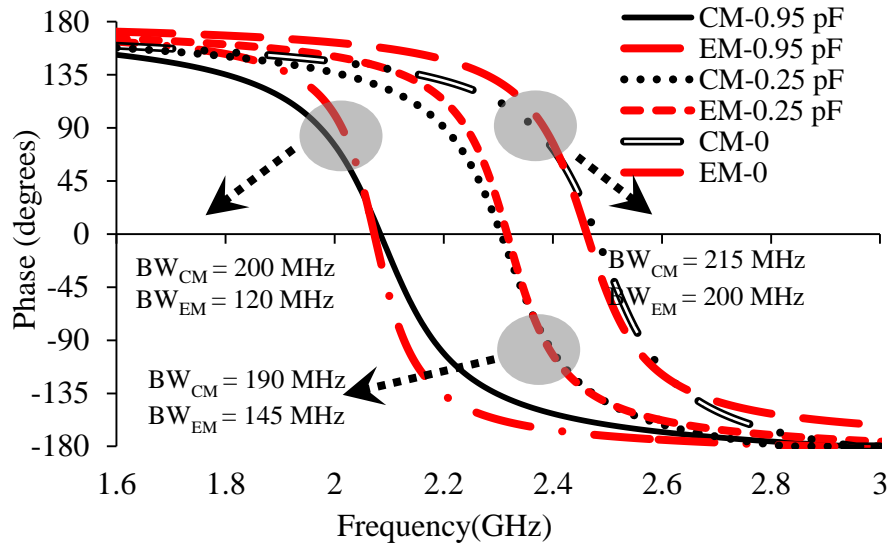
Figure 4.7: Reflection coefficient phase from the circuit model (CM) and electromagnetic simulations (EM) for an electrically asymmetric x-oriented unit cell. ±90° bandwidths are shown using shaded circles.

Table 4.1: Impact of dimensional variations for non-loaded and capacitively-loaded square patch unit cells.

Geometry type		Non-Loaded	Loaded
h_2 and h_1 (mm)	Tolerance	Δf (MHz)	Δf (MHz)
1.27	$\Delta Wa = 1mm$	300	130
	$\Delta g = 0.1mm$	260	60
2.5	$\Delta Wa = 1mm$	90	60
	$\Delta g = 0.1mm$	200	10

A desired outcome of using discrete capacitive-loading in the unit cell is that reduced sensitivity to dimensional variations is achieved. In a non-loaded SP FSS, the center frequency and bandwidth are highly dependent on the spacing between unit cells and the corresponding value of C_1 [45]. For $C_v = 0$, (4.6) and (4.8) show that small changes in C_1 can produce significant changes in the frequency response. Conversely, lower sensitivity is achieved when C_v

is the dominant capacitance assuming its value is tightly controlled. A comparison between a non-loaded and loaded unit cell that illustrates this difference is shown in Table 4.1; results are presented for two values of substrate height (h_1 and h_2).

4.2.2. Varactor Modeling

The diode selected for this design was the Aeroflex Metelics MGV050-20, which is a GaAs Abrupt Varactor with a nominal zero-bias junction capacitance between 0.5 pF and 0.6 pF, 50 pA of reverse saturation current and minimum quality factor of 4000 at 50 MHz. Since flexibility and low profile are desired for the design, a small package is preferred and therefore the type with dimensions of 2.7 mm x 2.6 mm ("H20" package) was chosen. Figure 4.8 shows the set up implemented in Advanced Design System (ADS) to calculate the effective capacitance for the diode. S-parameter measurements were taken and from here the effective capacitance was extracted using Y parameters and a pi-equivalent circuit model representation [80]-[82]. A quality factor of ~200 was extracted from the measured S-parameters at 2.5 GHz for a capacitance of 0.5 pF, which yielded a series resistance of ~2 Ohms.
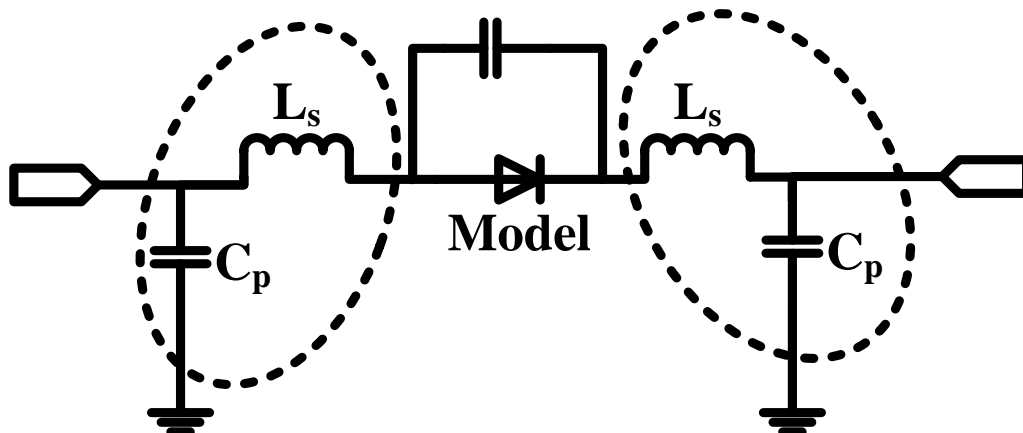
Figure 4.8: Schematic for diode simulation.
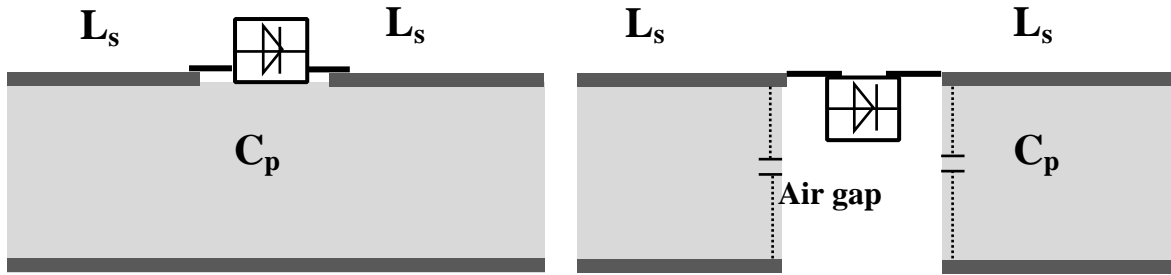
Figure 4.9: Diode mounting configuration; normal assembly (left-hand side) and inverted assembly (right-hand side).
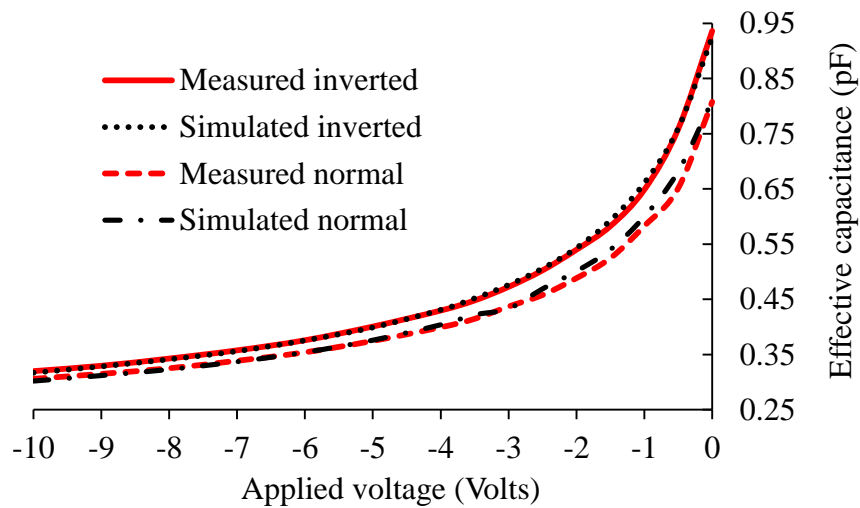
Figure 4.10: Effective capacitance at 2.45 GHz for the varactor diode in the normal and inverted mounting configurations (Figure 4.9).

Two methods for mounting the diodes to the substrate that forms part of the overall antenna construction were considered. The normal case, illustrated on the left-hand side of Figure 4.9, shows the MGV050-20 diode assembled over the lower substrate. The substrate introduces a capacitance modeled by the shunt capacitor (C_p), and the diode leads create an inductive behavior modeled with a series inductor (L_s). The inverted case, depicted on the right-hand side of Figure 4.9, shows the diode assembled into the lower substrate. The measured and extracted effective series capacitances, which are determined from the series element of the equivalent π-network, are plotted in Figure 4.10. The capacitance for the inverted case is slightly

higher than for the normal case, possibly due to the effects of the hole that is made in the ground plane when drilling through the substrate. The inverted configuration was chosen for the tunable FSS to maintain low profile characteristics given the height of the varactor diode (approximately 0.8 mm).

4.2.3. Semiconductor Antenna Design and Results

The tunable FSS was designed to operate at a center frequency of 2.4 GHz and built using a 1.27 mm-thick Rogers® RT6010 substrate, with a dielectric constant of 10.2. It has a planar size of 110 x 130 mm^2, including the bias network. It consists of 56 tunable hybrid unit cells and 56 varactor diodes. The criterion to select the number of diodes was based on the goals of maximizing performance and minimizing cost and planar size. Holes of approximately 1.1 mm in depth were drilled into the substrate to accommodate the packaged diode and maintain the low profile characteristic. The network is distributed in 8 rows, each containing seven diodes in series. Consistent with Section 4.2.1., the diodes were placed in the direction parallel to the main axis of the ELPOSD. A 1 KΩ resistor was used at the ends of each row to block RF leakage onto the bias lines. Figure 4.11 shows the fabricated tunable FSS.
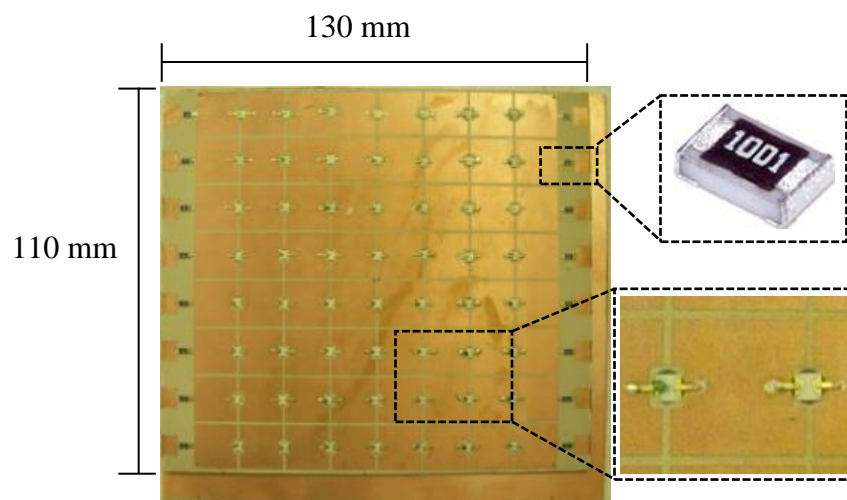
Figure 4.11: Tunable asymmetric FSS with bias network.

Figure 4.12 shows the simulated phase and magnitude of the reflection coefficient of the unit cell. The model includes the holes of 1.1 mm depth, the H20 ceramic package and a 0.2 mm air box between the FSS substrate and superstrate, which takes into account the height of the diode leads as provided by the manufacturer. The capacitance was varied from 0.3 pF to 1.0 pF as this corresponds to the approximate measured tunable range of the varactor diode. By taking into account the diode series resistance of 2 ohms described in section 4.2.2, the normalized magnitude of the reflection coefficient ($|\Gamma|$) in Figure 4.12 decreases from 0.92 (no resistance) to 0.86. In terms of a design criterion, the magnitude of the reflection coefficient is usually required to be $> |0.8|$, which corresponds to the minimum value for effective FSS operation [10], [66]. The impact of the series resistance on the reflection coefficient phase was even less significant. The simulation predicts a tunable bandwidth of 580 MHz, from 2.2 GHz to 2.78 GHz, when the criterion of 0 ± 90° phase shift is used.
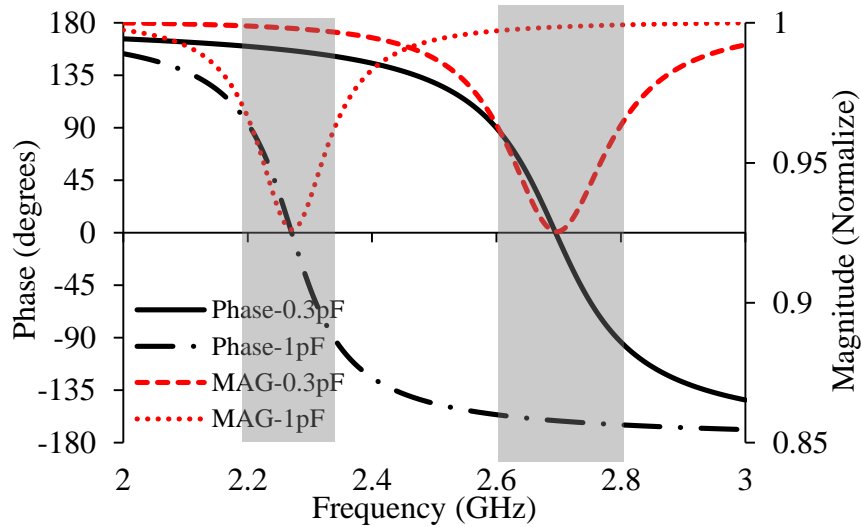
Figure 4.12: Simulated reflection coefficient phase and magnitude of the tunable FSS.

The ELPOSD was selected as the radiator to be consistent with the designs presented in chapter 3. The antenna was also fed through two wires coming from the output of a planar balun,

as demonstrated in [62]. When mounted to the FSS, the ELPOSD was oriented in the *x*-direction, so that its surface current vector is parallel to the direction where maximum tunability of the FSS occurs. Figure 4.13 depicts the magnitude of the surface current density, the surface current vector of the ELPOSD to confirm its linear polarization and its resulting dimensions; these simulations assume a free-space environment above the ELPOSD.
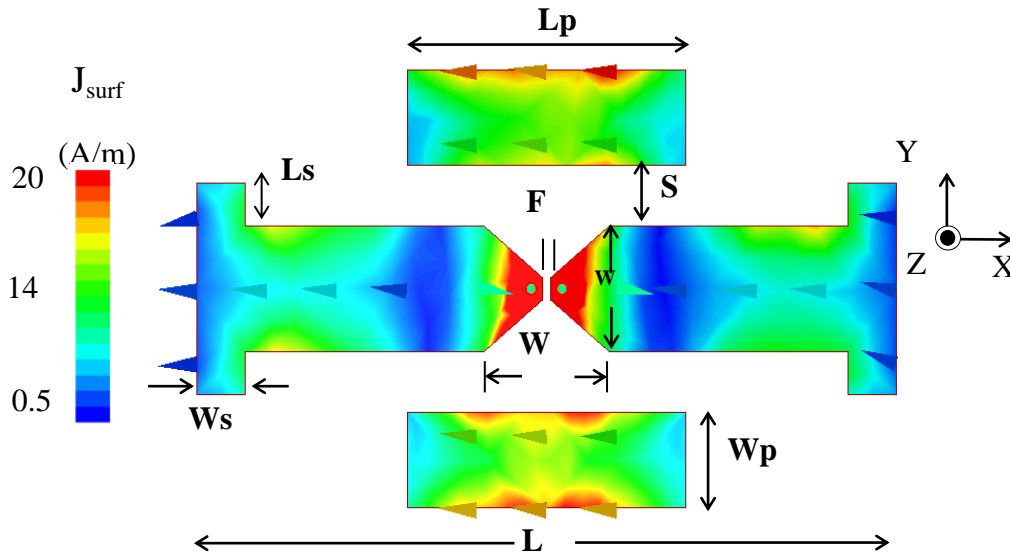
Figure 4.13: Magnitude of the surface current density, the surface current vector of the ELPOSD and geometry (L=35, Lp=11, Ls=1.99, W=19, Wp=10, Ws=2.35, S=1.5, F=0.6 (all units in mm)).

4.2.3.1.   Operation Using Uniform Bias Voltages in Free Space

Figure 4.14 shows the antenna assembly which integrates the ELPOSD, DC bias, FSS and ground plane with an overall dimension of 120 x 133 mm^2. It has eight independent DC voltage lines, for which each total voltage is divided evenly between the seven diodes per row. The antenna thickness (excluding the feed layer) is ~λ/45 at 2.4 GHz. With the feed layer the total thickness of the antenna is ~λ/32; however in the envisioned design this layer can be replaced with a much thinner and smaller MMIC chip.

DC Bias   1 KΩ resistors and ground

V_1
V_2
V_3
V_4
V_5
V_6
V_7
V_8

120 mm

133 mm
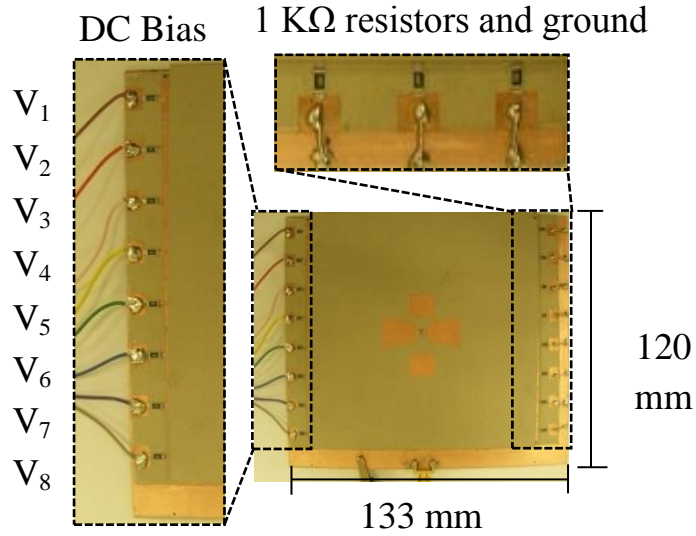
Figure 4.14: Top view of the antenna assembly showing 8 independent voltage ports and resistors to isolate the RF leakage from the bias lines.

Measured S_{11} data for the antenna when applying a common bias voltage of 0 V, 35 V and 70 V to all DC bias ports are shown in Figure 4.15. Using the 10 dB return loss criterion, there is a 510 MHz span between the low end of the response with 0 V and the high end of the response using 70 V. This span correlates approximately with the $\pm 90^o$ boundaries given in Figure 4.12.
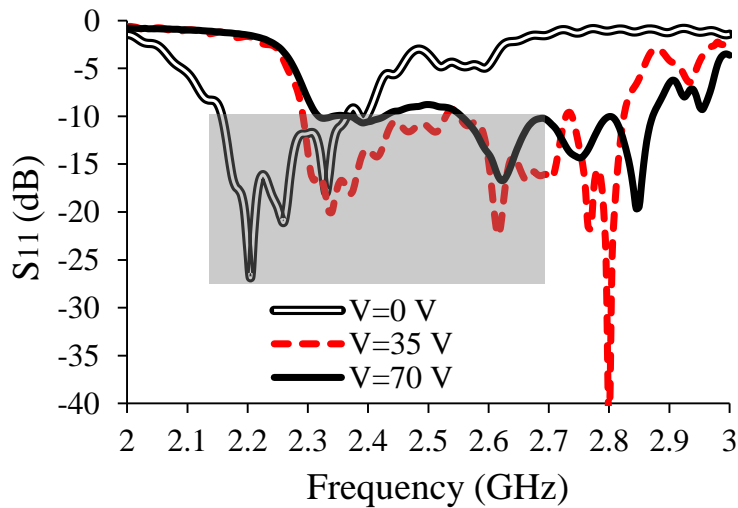
Figure 4.15: Measured S_{11} when each of the 0 V, 35 V and 70 V voltage levels is applied to all DC bias lines.

68

Comparisons between simulation and measurement data are given in Figure 4.16. For the simulated results, the capacitance value that provided the best correlation to measurement data at each bias point was offset from the expected value (Figure 4.10) by approximately 0.25 pF; specifically, the expected range from 0.95 to 0.32 pF was changed to 1.2 to 0.55 pF. This variation was necessary in order to compensate for potential dielectric variations due to air gaps between the substrate layers of the FSS. A summary of the measured and simulated performance is provided in Table 4.2.

Table 4.2: Correlation between gain, voltage and capacitance for the GaAs based antenna.

Bias Voltage (V)	0	10	20	30	40	50	60	70
Peak gain (dBi)	4	3.7	4.15	5.05	4.7	4.5	4.5	4.2
3dB gain bandwidth (MHz)	120	55	140	210	280	300	325	360
Single diode voltage (V)	0	1.4	2.9	4.3	5.7	7.1	8.6	10
Diode effective capacitance (pF)	0.95	0.55	0.47	0.43	0.38	0.36	0.33	0.32
HFSS diode capacitance (pF)*	1.2	0.85	0.75	0.7	0.65	0.63	0.6	0.55

* Value used in HFSS to obtain best agreement with measured S_{11} data.
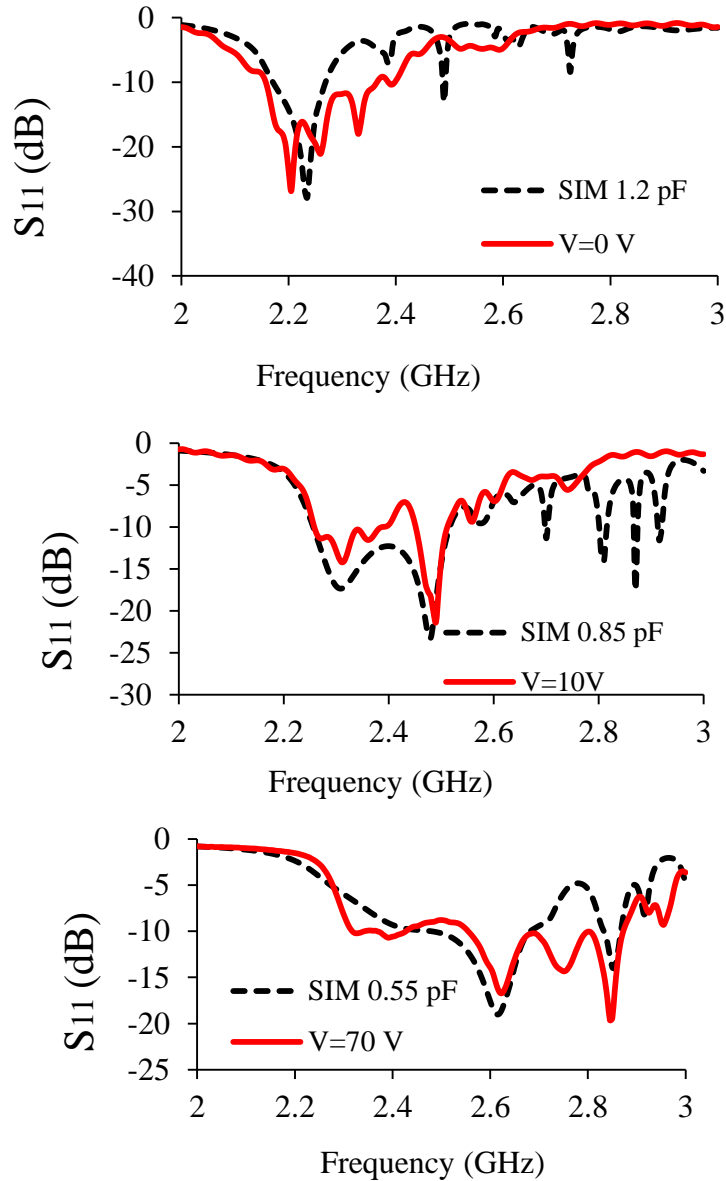
Figure 4.16: Measured and simulated S_{11} when 0 V, 10 V and 70 V is applied to all bias ports; the voltage across individual diodes is 0, 1.4 and 10 V, respectively.

Figure 4.17 illustrates the measured antenna gain at broadside for different values of DC bias. The antenna exhibits gain of more than 3 dBi from 2.1 GHz to 2.63 GHz. Consistent with (4.8), the gain bandwidth increases with the applied voltage. The maximum gain is obtained when the applied voltage is 30 V, which corresponds to the operational center frequency of the tunable FSS, antenna and balun.

The E-plane radiation patterns of the antenna for different bias voltages are shown in Figure 4.18. The radiation pattern in a linear dipole is formed when the fields radiated by its two arms reinforce each other [2]. Ideally, the transmission feed lines are designed to have the same current distribution magnitude, with a 180º phase reversal. This condition is maintained in the balun used here for frequencies between 2.35 and 2.65 GHz. It can be seen in Figure 4.18 that the patterns are rotated away from broadside for frequencies below 2.35 GHz due to the limited bandwidth of the balun; the balun limitation also affects the broadside gain measurement (Figure 4.17). Consistent with (4.6), (4.7) and Table 4.2, it is seen that by increasing the voltage and decreasing the grid capacitance, the resonant frequency and bandwidth of the FSS increase. The radiation patterns degrade for frequency bands where the image currents on the FSS are more out-of-phase than in-phase.
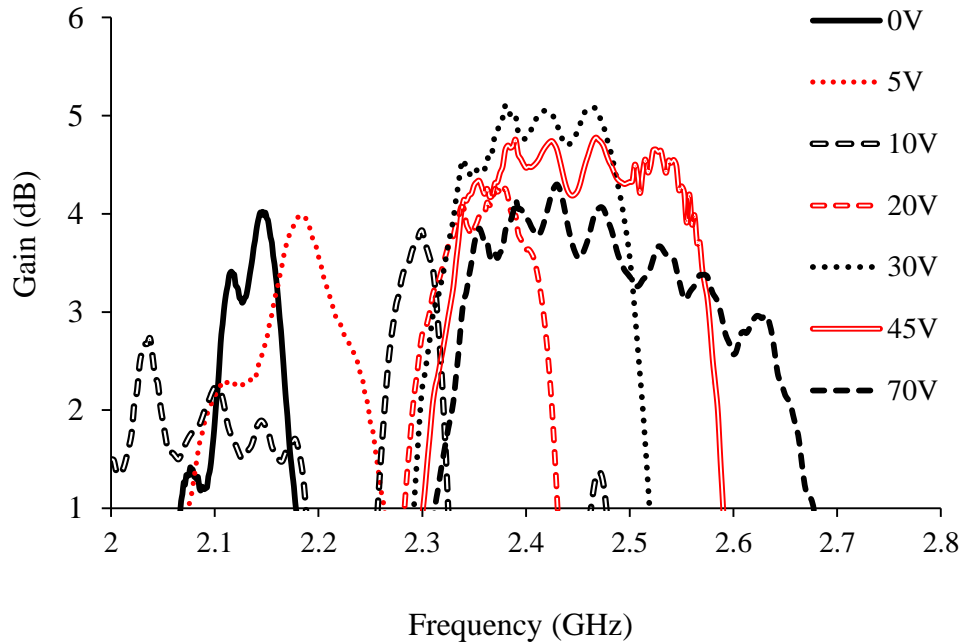
Figure 4.17: Measured gain of the antenna for different bias voltages for the GaAs based antenna.
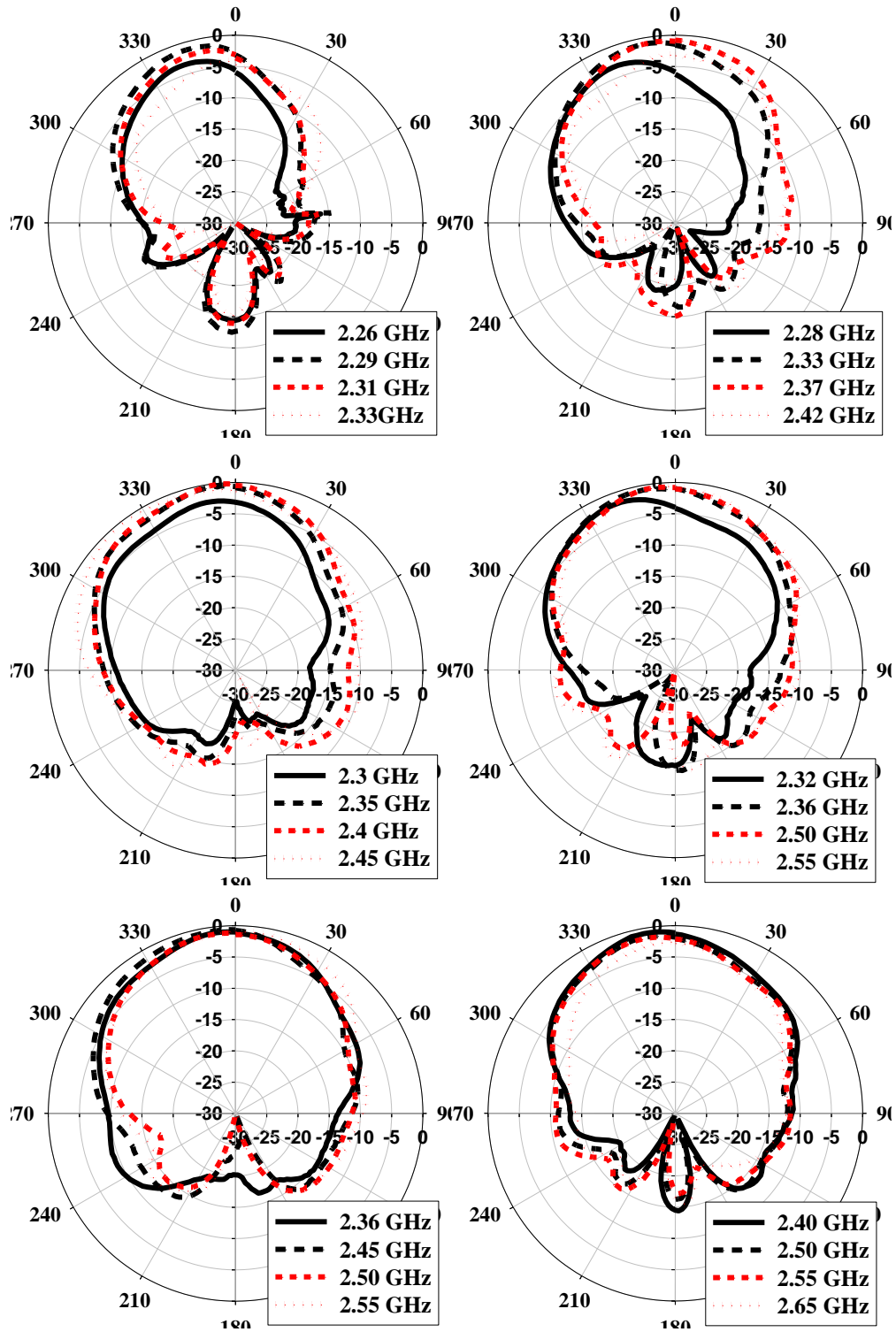
Figure 4.18: Measured E-plane radiation patterns for the GaAs varactor based antenna with bias voltage of 10 V (top left), 20 V (top right), 30 V (middle left), 45 V (middle right), 55 V (bottom left) and 70 V (bottom right).

The performance of the antenna is summarized in Figure 4.19. Here, the bandwidth (error bars in Figure 4.19) is defined as the band over which the return loss is greater than 10 dB and the gain is more than 3 dBi. For example, at 30 V applied bias, the center frequency is 2.4 GHz, the bandwidth is 150 MHz and the peak gain at broadside is 5.05 dBi. The shaded region shows tunability from 2.15 GHz to 2.63 GHz (i.e. BW ≈ 480 MHz) with gain greater than 3 dBi. The gain was determined using the substitution method. Using Ansoft HFSS the antenna efficiency was found to be between 55% and 93% depending on the capacitance value assigned to the varactor diode. The efficiency of the antenna was measured using a Wheeler cap and the values obtained were between 50% and 90% depending on the voltage [22]. To verify the accuracy of the gain and radiation pattern measurements, comparison tests were performed at NASA Glenn Research Center (GRC) and at the University of South Florida (USF) (Figure 4.20). The agreement in the peak broadside gain measurements made at each facility was better than ± 0.3 dB.
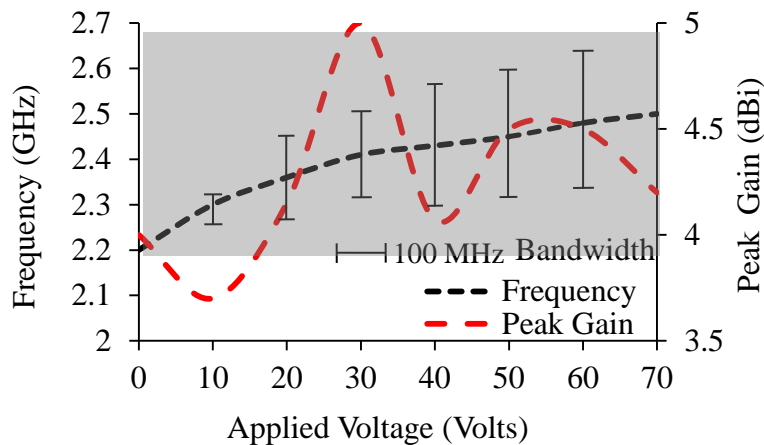
Figure 4.19: Performance of the GaAs varactor based antenna versus bias voltage.
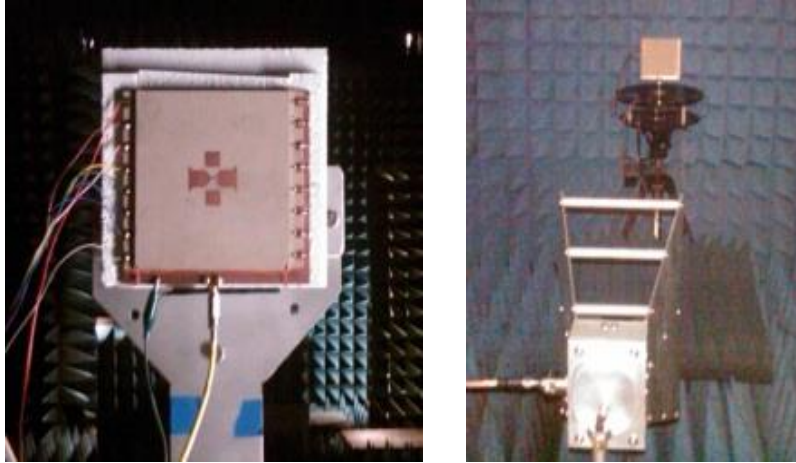
Figure 4.20: Top view of the antenna mounted in the fixture at NASA GRC (left) and the measurement setup at USF (right).

4.2.3.2.   Operation Using Non-Uniform Bias Voltages in Free Space

It is well-known that the performance of the antenna is affected by the finite extent of the FSS, since its edge presents an abrupt boundary condition that reflects energy trapped within the substrate. In Section 4.2.2, the impedance of the FSS was calculated assuming an infinite number of symmetrical unit cells and with the cells excited by plane waves at normal incidence [55]. As shown in [52], the antenna system can be described as the parallel combination of this FSS impedance and the dipole impedance in free space. However, since neither of the assumptions about the FSS is true in practice, the impedance match and radiation patterns deviate from the ideal condition. In [45], [55] and [83], the improvement in antenna performance with increasing ground plane size was demonstrated. For the design presented herein, the boundary conditions around the perimeter can be altered by producing a spatial variation in the FSS impedance. This variation is achieved by using a non-uniform bias across the eight rows of diodes.

The results presented in Figure 4.21 and Figure 4.22 demonstrate the measured performance of the antenna using different FSS bias configurations (Table 4.3). With a uniform voltage of 45 V on all rows (Configuration A), the antenna exhibits high gain and broad

bandwidth although surface wave effects are noticeable by the non-uniformity in the radiation pattern. For Configuration B, the first five rows are biased at 45 V and the last three rows are biased at 60 V. The return loss for this configuration is nearly identical to the case with uniform bias, but as observed in Figure 4.22 the radiation patterns are actually more symmetric. These results suggest that the pattern distortion for Configuration A is caused by imperfections in the assembly of the structure, possibly the planarity of the multi-layer assembly, and that they were compensated by the non-uniform bias. The results for Configuration C in Figure 4.21 demonstrate that the return loss can be strongly affected by applying a different voltage to the exterior rows of the FSS that are not directly beneath the dipole antenna. When a lower voltage is applied to the exterior rows the effective capacitance of the varactors in these rows increases, decoupling the parasitic sleeves and creating another resonant frequency at 2.3 GHz. The gain of the antenna system for Configuration C at the minimum S_{11} (2.3 GHz) also drops by 5 dB and the radiation pattern is distorted.

Table 4.3. FSS bias configurations in free space for the GaAs based antenna.

Configuration	V_1, V_2	V_3	V_4, V_5	V_6	V_7, V_8
A	45 V	45 V	45 V	45 V	45 V
B	45 V	45V	45 V	60 V	60 V
C	20 V	20V	45 V	20 V	20 V
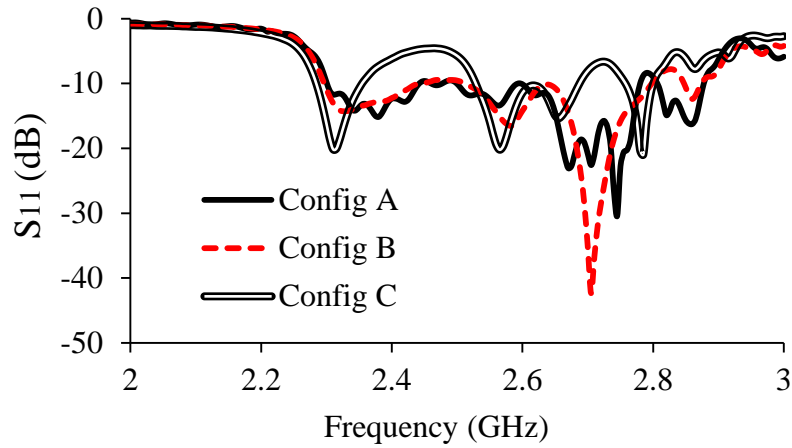
Figure 4.21. Measured S_{11} when non-uniform bias is applied to the diodes for the GaAs varactor based antenna.
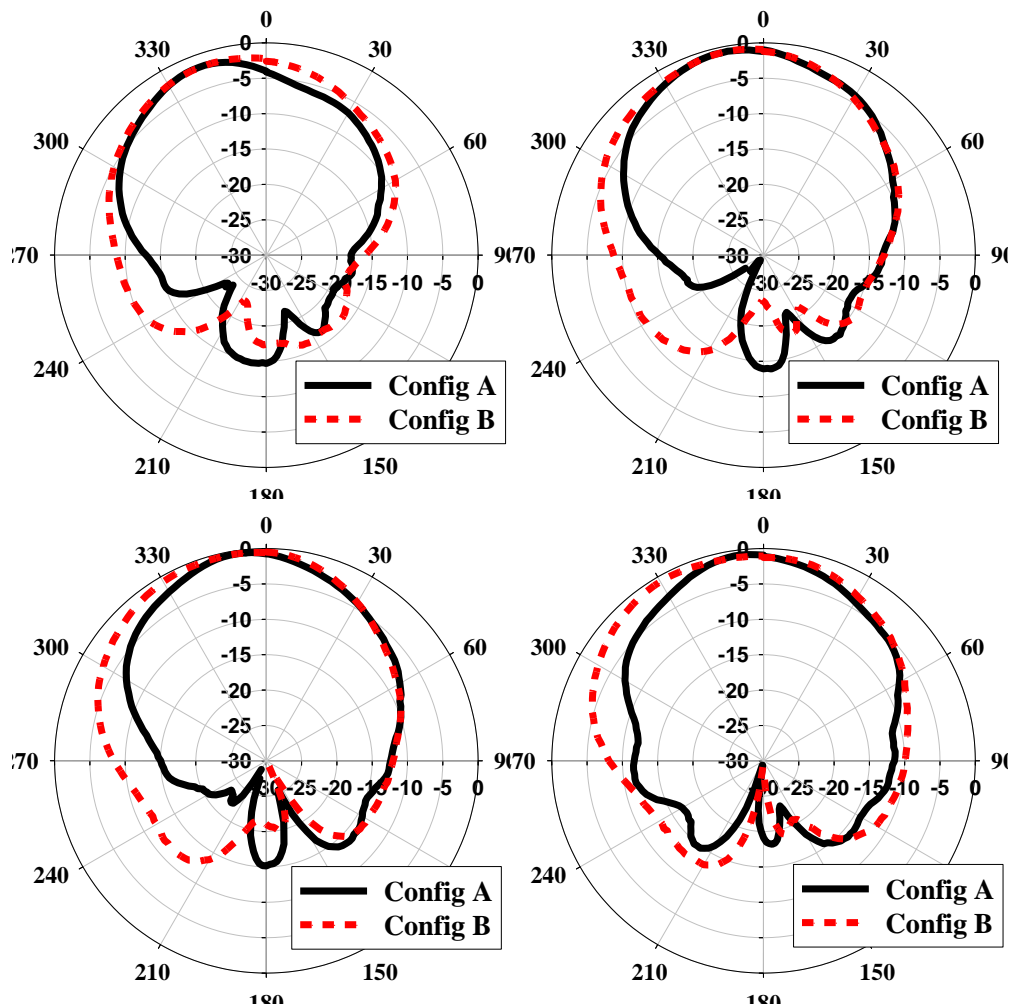
Figure 4.22: Measured E-plane radiation patterns for voltage configurations A and B in Table 4.3: 2.32 GHz (top left), 2.36 GHz (top-right), 2.40 GHz (bottom left) and 2.50 GHz (bottom right).

4.2.3.3. Operation Using Non-Uniform Bias Voltages in in The Presence of Human Core Model

In this section the antenna performance is characterized in the presence of a Human Core Model (HCM) phantom, which mimics a conical volume of the human stomach explained in detail in [69], [84]. The objective is to assess how the performance of dipole antenna backed with an electronically-tunable FSS is affected by close proximity to human tissue. Figure 4.23 shows the HCM which consists of a solid skin-muscle tissue phantom and liquid blood-fatty tissue phantom. With a uniform voltage of 30 V on all rows of the FSS and in free space (Configuration D in Table 4.4), the antenna has a good impedance match from 2.26 GHz to 2.52 GHz. When the HCM is placed at a 20 mm offset from the face of the antenna (Configuration E), the S_{11} response is changed as depicted in the shaded region in Figure 4.24. The HCM deteriorates the antenna performance by producing input impedance variations, resonance shift and bandwidth degradation. However, by adjusting the bias voltage at the input lines (Configurations F-H), the antenna performance can be improved and depending on which configuration is used the frequency range from 2.28 GHz to 2.8 GHz can be covered (Figure 4.25). These results demonstrate that this type of antenna allows adjustment in response to near field loading making this design amenable to biomedical radiometric sensing applications.

Figure 4.23: HCM consisting of a solid skin-muscle tissue phantom and liquid blood-fatty tissue phantom (left), antenna at 20 mm separation from the HCM (right).

Table 4.4. FSS bias configurations in the presence of HCM for the GaAs based antenna.

Configuration	V_1, V_2	V_3	V_4, V_5	V_6	V_7, V_8
D (no HCM)	30 V	30 V	30 V	30 V	30 V
E (w/HCM)	30 V	30 V	30 V	30 V	30 V
F (w/HCM)	10 V	30 V	30 V	30 V	20 V
G (w/HCM)	50 V	30 V	30 V	30 V	50 V
H (w/HCM)	100 V	100 V	100 V	100 V	100 V
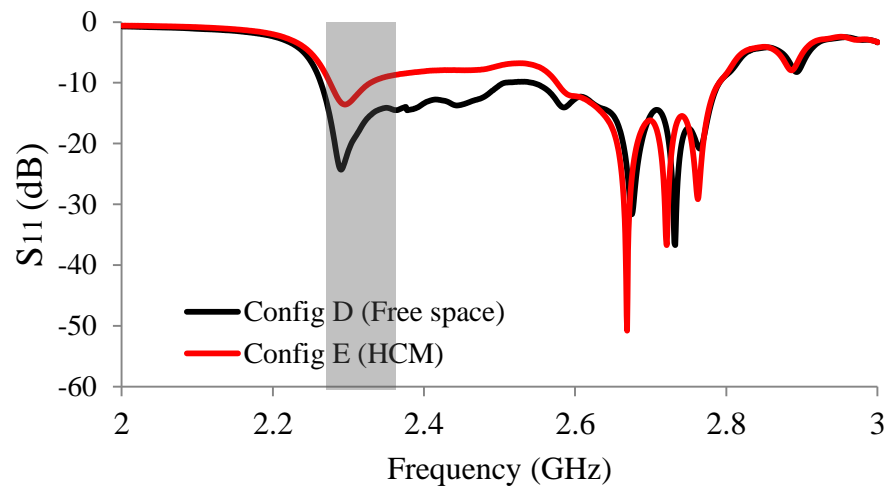
Figure 4.24: Measured S_{11} of the antenna in free space and in the presence of the HCM when a 30 V uniform bias is applied to the diodes.
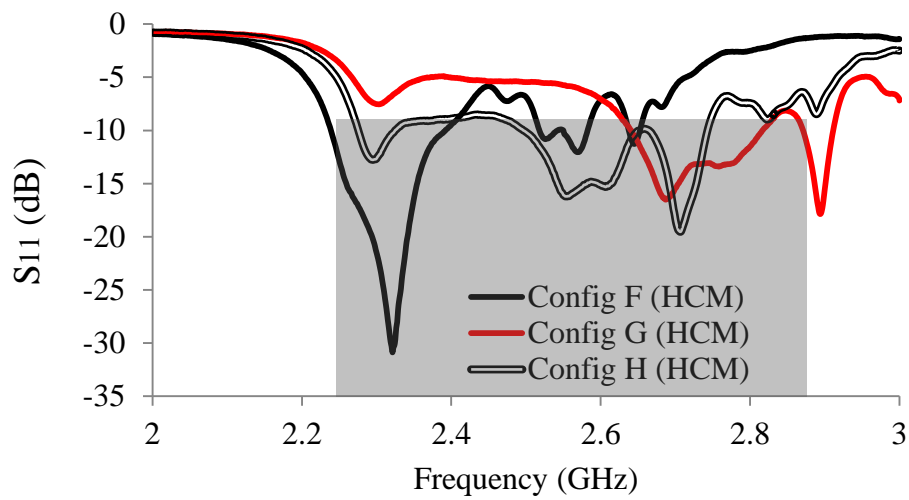
Figure 4.25: Measured S_{11} of the antenna in presence of the HCM when non-uniform bias is applied to the diodes.

4.3.   Low Profile Tunable Dipole Antenna Using BST Varactors

In this section a 2.4 GHz low profile dipole antenna that uses a frequency selective surface (FSS) with interdigital ferroelectric-based barium strontium titanate ($Ba_{0.6}Sr_{0.4}TiO_3$; henceforth BST) varactor-tuned unit cells is presented. The antenna uses similar radiator and feed layers as the structure presented in section 4.2. The tunable unit cell is a square patch with a small aperture on either side to accommodate the BST devices. The BST varactors were fabricated on alumina substrates and demonstrate capacitance tuning of 1.5:1 (33%) at 90 V. The varactor chips were placed only along one dimension of the FSS to avoid the use of vias and simplify the DC bias network. The FSS is sandwiched between two 1.27 mm-thick substrate layers, resulting in a total antenna thickness (excluding the feed layer) of $\sim\lambda/47$ at the operational central frequency of 2.4 GHz.

Specifically, the intention of this section is to investigate the use of BST to enable the development of low profile tunable antennas for biomedical radiometric sensing [21]. In this type of application, the cost, size and robustness of the tunable devices are all important design constraints. The use of semiconductor varactors and pin diodes to fabricate tunable antennas, as demonstrated in [11]-[14], [21] may therefore be less desirable than using BST varactors. In comparison to the semiconductor devices, BST is relatively simple and inexpensive to process; for the custom-designed interdigital varactors used herein, only a BST- and subsequent electrode-layer deposition are needed. BST can also be deposited onto a ceramic substrate (in this case Al_2O_3) which provides a compact, rigid platform that prevents damage under possible flexing of the thin antenna. In contrast, due to the fragile nature of semiconductor materials such as GaAs and silicon, external plastic or ceramic packages are typically needed to ensure the integrity of the devices and can significantly increase the footprint. Despite these potential

79

advantages of BST varactors, their electronic properties may have yet to match those of semiconductor devices. However, it is still relevant to assess how the aforementioned tradeoffs affect the performance of the antenna under study.

Due to the small size of the BST chips, the FSS unit cell size could be reduced by 35% compared to the design presented in section 4.2, resulting in an overall 50% reduction in the antenna size. The antenna is also more robust because the BST varactors do not suffer from the intrinsic fragility of the GaAs varactors which required packaging to allow integration into circuit boards. Regarding cost, the BST varactors are estimated to be at least an order of magnitude less expensive than the GaAs varactors due to the simplicity of the BST fabrication process, which translates into the BST-based antenna being more cost effective than GaAs varactor-based counterpart. In addition to the aforementioned advantages, a novel bias scheme with no interlayer wiring to ground and lower voltage requirements with respect to the semiconductor varactor based antenna discussed previously in section 4.2 is introduced in this design. The symmetric C-V curve of the BST varactors along with the use of one-dimensional tuning of the FSS, are leveraged to simplify the DC bias network. In order to protect the integrity of the BST film in the assembly process, the varactors were coated with benzocyclobutene (BCB). The 33% tunability range of the interdigital varactors allows the operating frequency of the antenna to be varied from 2.23 – 2.55 GHz. While the Q-factor of the BST varactors is smaller than that of their GaAs counterparts discussed in section 4.2 (e.g., Q-factor of ~11 at 2.4 GHz) which results in a drop in radiation efficiency of approximately 20%, there are approaches such as the increase in thickness of the FSS layer that could be used to compensate for this effect. In the following sections, the BST varactor design, fabrication, permittivity extraction and

modeling are presented, along with the design and fabrication of the antenna backed by the tunable FSS.

4.3.1. BST Varactor Development

4.3.1.1. Design and Fabrication

Interdigital capacitors (IDCs) using coplanar waveguide (CPW) feed lines were initially fabricated and measured employing a similar procedure as explained in [80]. Using RF sputtering, the BST was deposited onto 500-µm-thick polycrystalline alumina substrates. The average thickness measured on the BST layer was approximately 350 nm. The metal layer consists of a 15 nm chrome adhesion layer and 800 nm gold layer. The CPW devices have dimensions of 1.05 x 0.9 mm^2. Figure 4.26 depicts a 3D schematic diagram of the multilayer IDC structure identifying its layers, dielectric constants and thicknesses.
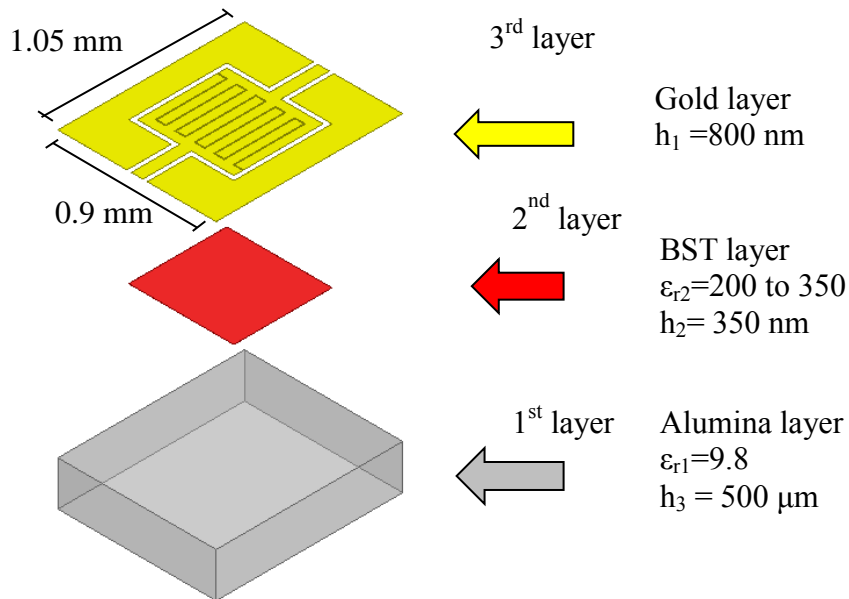
Figure 4.26: 3D schematic diagram of the CPW multilayer IDC identifying the dielectric constant and thickness of each layer.

To characterize the BST varactors, IDCs consisting of three, five and seven pairs of fingers were fabricated on top of the patterned BST thin films. The fingers are 400 μm long by 50 μm wide, and are separated by a 5 μm gap [80]. Figure 4.27 shows the measured capacitance vs. voltage for representative devices at 1 GHz. The capacitance changed by 1.5:1 at 90 V DC bias, demonstrating a tunability of 33%. The 5 finger configuration was selected for the FSS design as its extracted capacitance allows a unit cell size of only 0.07λ at 2.4 GHz (8.9 mm) which is smaller than cells presented in section 4.2 and [12]-[14], [76]-[77]. The unit cell size was 30% larger for the 3 finger configuration and for the 7 finger configuration it was considerably smaller (0.045λ); however, the fabrication complexity of the antenna is increased for the latter.
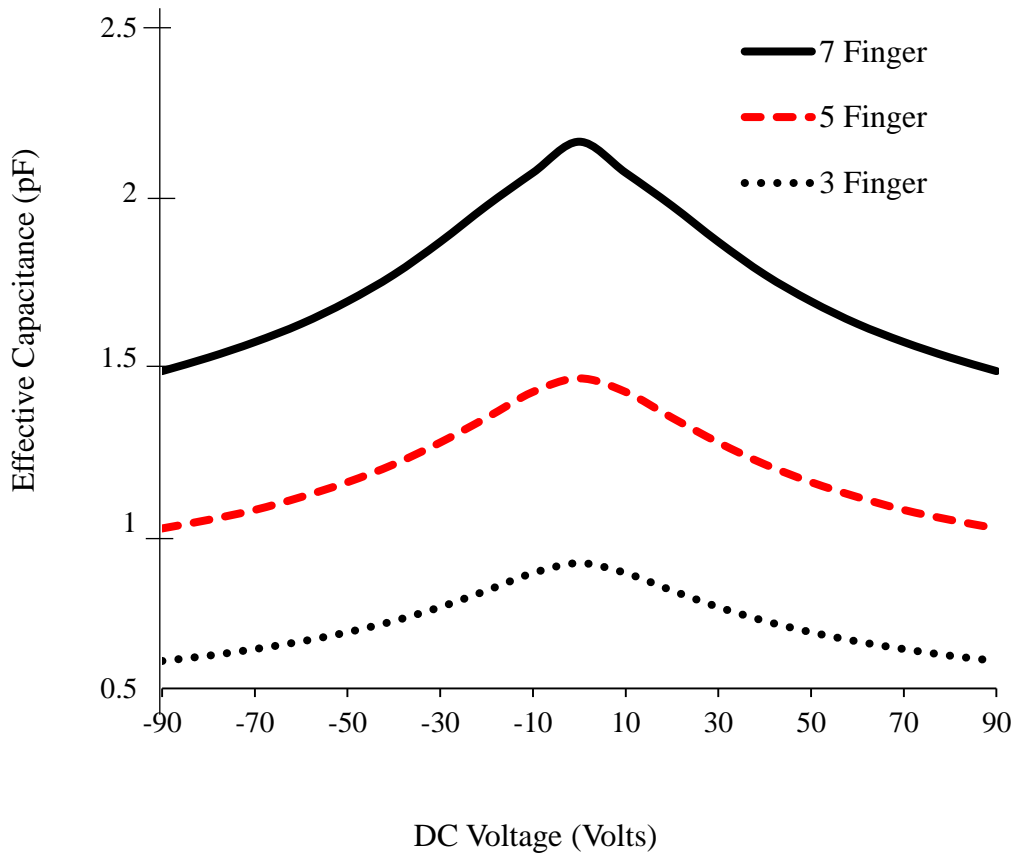
Figure 4.27: Measured effective capacitance vs. voltage for 3, 5 and 7 finger IDCs at 1 GHz.

4.3.1.2. Permittivity Extraction

The relative permittivity of the $Ba_{0.6}Sr_{0.4}TiO_3$ thin films was extracted using full-wave numerical electromagnetic software (Ansoft HFSS) and compared to a conformal mapping-based model for CPW device structures (CAD model) [50]. In this CAD model the finger end capacitance in (4.9) was defined as "half of the capacitance of the three-strip structure". However, (4.9) actually calculates the full capacitance of the three-strip structure and thus was modified as shown in (4.10). The modified equation also takes into account Wheeler's approximation for the case in which electric field at the corners of the finger is not uniform [87]. Aside from this correction for finger end capacitance the model as presented in [50] was implemented in MathCad. As with the CAD model, the CPW structures were also simulated using Ansoft HFSS to determine the BST permittivity by fitting the effective capacitance to the measured data. Figure 4.28 shows the measured data at 0 V and 90 V DC bias for the 5-finger device, along with the simulated data for different values of ε_{r2} (ref. Figure 4.26).

$$C_{end} = 4ns(2 + \pi)\epsilon_{end}\varepsilon_0 \frac{K(\kappa_{0end})}{K(\kappa'_{0end})} \tag{4.9}$$

$$C_{end} = 2ns\left(2 + \frac{\pi}{2}\right)\epsilon_{end}\varepsilon_0 \frac{K(\kappa_{0end})}{K(\kappa'_{0end})} \tag{4.10}$$

Table 4.5 shows a comparison of the permittivity values that best match the measured data using both methods. Using Ansoft HFSS the permittivity was found to be between 350 and 230 for the 0 V and 90 V bias cases, respectively. The CAD model using (4.10) estimates values of 360 and 210, which are in close agreement with those estimated by HFSS. The extracted permittivity values using (4.9) in the CAD model were significantly different (between 180 and 90).

83

Table 4.5: Permittivity extracted from BST samples at 1.0 GHz for 3, 5 and 7 Finger Interdigital Capacitors (IDCs).

IDC Number of Finger Pairs	Measured Cap. at 0 V and 90 V (pF)	Extracted ε_{r2} at 0 V and 90 V (HFSS)	Extracted ε_{r2} at 0 V and 90 V (CAD model) Eqn.(4.10)
3	0.75-0.5	350-230	350-200
5	1.4 -0.98	350-230	360-210
7	2.1 -1.45	350-230	370-220
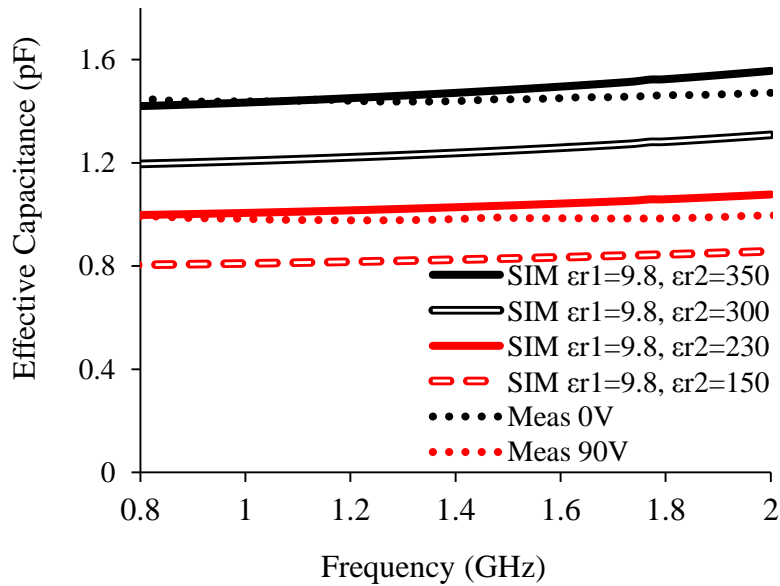
Figure 4.28: Effective capacitance vs. frequency for a 5-finger BST varactor on alumina. Measured data and HFSS simulation results are shown.

4.3.1.3. BST Varactor Modeling

The equivalent circuit model of the BST interdigital capacitor is shown in Figure 4.29, where C is the capacitance between the interdigitated fingers, R_p the parallel resistance representing dielectric loss, R_s the series resistance of the metal electrodes, L_s the series parasitic inductance and C_p is the capacitance between the IDC fingers along the outer perimeter of the device and the ground planes of the CPW lines [88], [89]. The model was implemented in Advanced Design System (ADS) and optimizations were performed to determine the values of these added components by matching the measured S-parameters to the simulated S-parameters.

Optimization goals were set to minimize the differences of the measured and modeled S_{21} responses and that of the measured and modeled S_{11} responses for the frequency range of 0.4 – 6.5 GHz. R_s was calculated using (4.11), where *a* defines the frequency-independent resistant and *b* accounts for the frequency-dependent skin effect. Five finger devices were also fabricated on magnesium oxide (MgO) and sapphire substrates to test the accuracy and repeatability of the model. The effective capacitances were extracted using Y parameters and a pi-equivalent circuit model representation [88]-[90]. Measured and modeled effective capacitance and S-parameter responses resulting from the optimization are shown in Figure 4.30. The quality factor was obtained using the formula presented in [90]. A Q-factor of ~11 was extracted from the measured S-parameters at 2.5 GHz for the alumina sample with a capacitance of 1.5 pF. Table 4.6 shows the lumped parameter values extracted from the model at 2.5 GHz with 0V DC bias.

$$R_s(\Omega) = a + b\sqrt{f(GHz)} \hspace{3cm} (4.11)$$
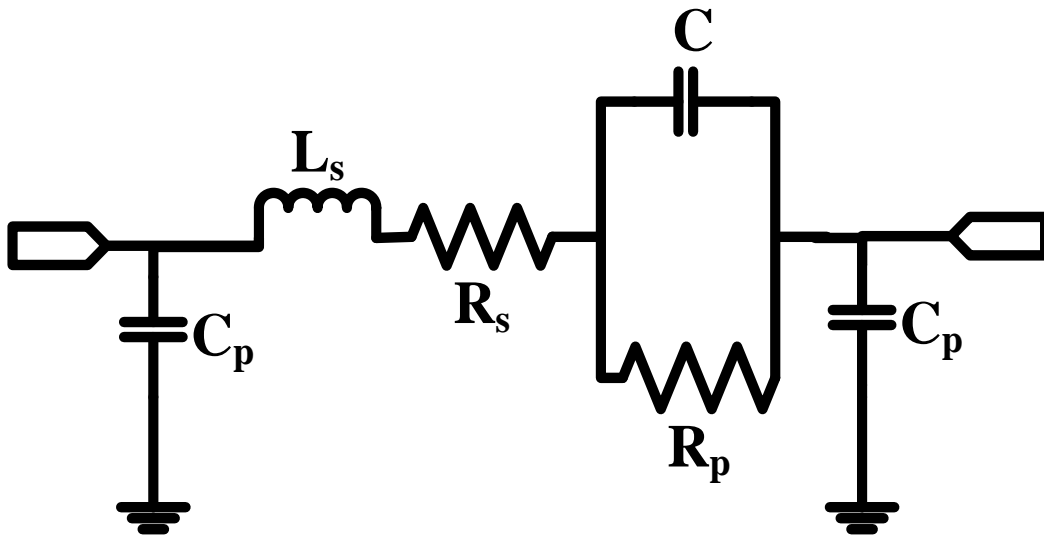
Figure 4.29. Equivalent circuit model of the BST interdigital capacitor.

Table 4.6: Lumped parameters extracted at 2.5 GHz with 0 V DC bias.

Substrate	C (pF)	C_p (pF)	L_s (nH)	R_p (Ω)	a	b
Al_2O_3	1.45	0.1	0.23	1200	2.5	0.16
Mg0	0.97	0.1	0.23	1100	2.5	0.16
Sapphire	1.8	0.1	0.23	500	2.5	0.16

4.3.1.4. BST Chips Used in the FSS

The previous fabrication process flow described was modified in order to accommodate integration of the varactors into the FSS layer. First, the ground-signal-ground (CPW) feed lines were removed and replaced with bonding pads on each end. Also, to protect the BST from the conductive epoxy used to connect the varactors to the unit cells, a benzocyclobutene (BCB) layer was applied to the top surface and patterned to expose the bonding pads. As the final fabrication step, the alumina wafer on which the varactors were fabricated was diced into individual chips measuring 2.4 x 0.7 mm^2; this includes the two 0.7 x 0.7 mm^2 bonding pads. This planar size represents a 76% of area reduction with respect the diode selected in section 4.2.2 which had dimensions of 2.7 x 2.6 mm^2. Notice that the planar size of the chips can be further reduced by decreasing the bonding pad area. Figure 4.31 shows the process flow diagram.

Figure 4.32 depicts the top view of a fabricated BST chip and its 3D schematic diagram identifying its layers, dielectric constants and thicknesses. Figure 4.33 shows the measured effective capacitance of a chip with and without the BCB layer. The results demonstrate that no significant change occurs in the effective capacitance due to the presence of the BCB.
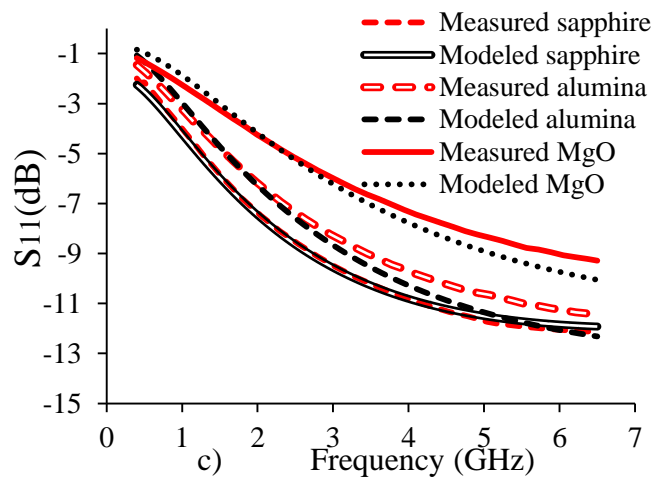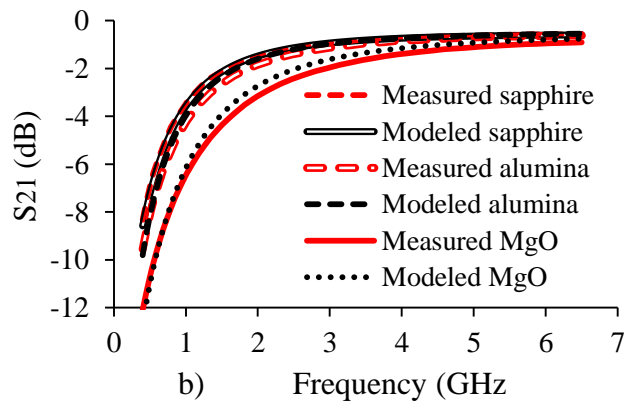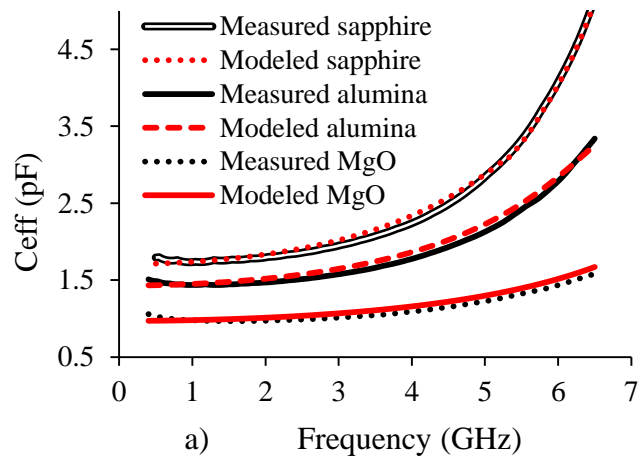
Figure 4.30: Effective capacitance vs. frequency for a 5-finger BST varactor on alumina, MgO and sapphire. (a) Measured and modeled S-parameters of 5 finger IDCs: S_{21} (b) and S_{11} (c).
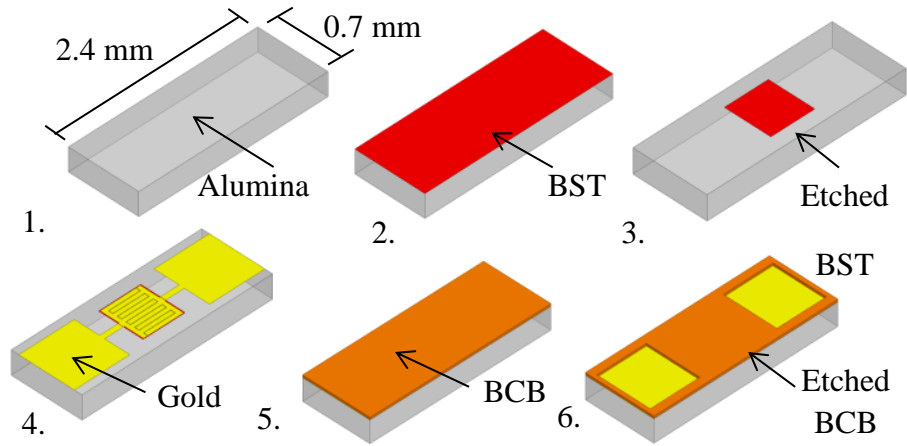
Figure 4.31: Process flow diagram for the BST chip varactor.
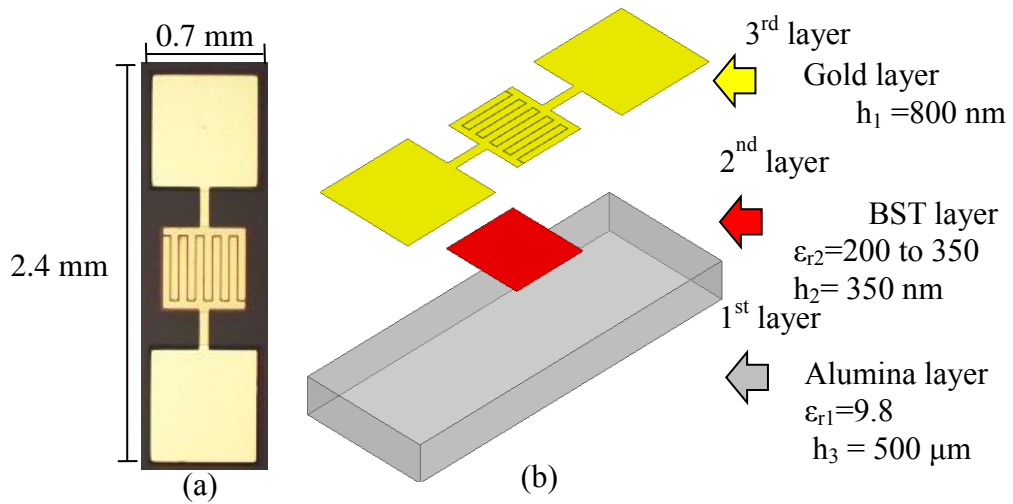
Figure 4.32: (a) Top view of the BST chip. (b) 3D schematic diagram of the multilayer IDC identifying all its layers, dielectric constants and their thickness.
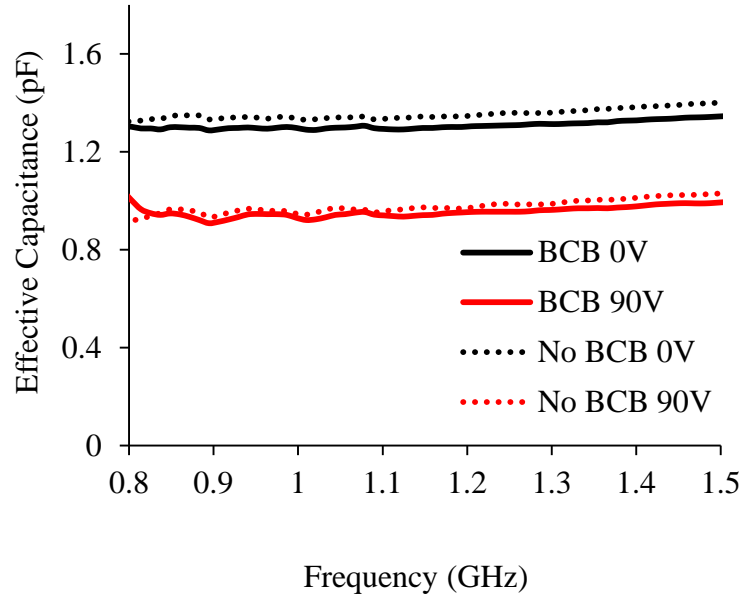
Figure 4.33: Effective capacitance vs. frequency for a 5-finger BST chip varactor on alumina.

4.3.2. BST Antenna Design and Results

The tunable FSS was designed to operate at a center frequency of 2.4 GHz and built in a 1.27 mm-thick Rogers® RT6010 substrate, with a dielectric constant of 10.2. It has a planar size of 86 x 84 mm^2, including the bias network. It consists of 64 tunable unit cells and 56 BST varactors. The criterion to select the number of varactors was based on the goal of maintaining a similar number of devices as in section 4.2.3. Holes of approximately 0.5 mm in depth were drilled into the substrate to accommodate the chips and maintain the low profile characteristic. The network is distributed in 8 columns, each containing seven BST chips in series, and 8 rows with 1 KΩ resistors in series. Similar to the GaAs varactor based antenna, the varactors were placed in the direction parallel to the main axis of the ELPOSD to achieve higher tunability. A 1 KΩ resistor was used at the ends of each row to block RF leakage onto the bias lines. Figure 4.34 shows the fabricated tunable FSS.

89
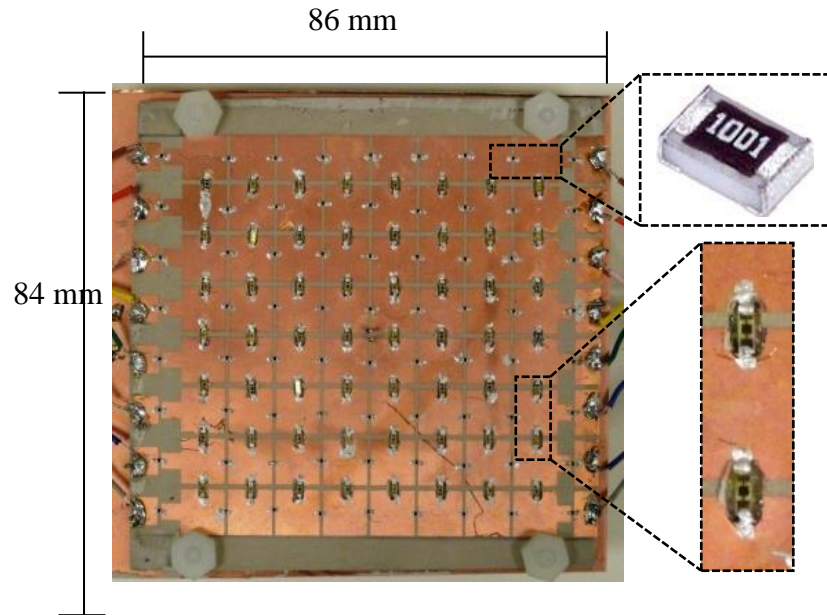
Figure 4.34: Tunable FSS with bias network.

Figure 4.35 shows the antenna assembly which integrates the ELPOSD, DC bias network, FSS and ground plane with an overall dimension of 84 x 94 mm^2. This represents a 50% area reduction in comparison to the GaAs varactor based antenna presented in section 4.2. The miniaturization was possible because of the smaller device size, which allowed the unit cell size to decrease by 35%. The antenna has eight independent DC voltage lines, on which the odd lines (V_1, V_3, V_5, V_7) are biased at the same voltage but opposite polarity with respect to the even lines (V_2, V_4, V_6, V_8) to create a virtual ground between them (Table 4.7). This bias network takes advantage of the symmetric behavior along the zero-bias voltage axis in the C-V curve and reduces the maximum required voltage. The antenna thickness (excluding the feed layer) is ~$\lambda/47$ at 2.4 GHz. With the feed layer, which was fabricated on a 1.27 mm-thick Rogers$^®$ RT6010 substrate, the total thickness of the antenna is ~$\lambda/33$; however, in the envisioned design the feed layer can be replaced with a much thinner and smaller MMIC chip.

Table 4.7: FSS bias configurations in free space for the BST based antenna.

Config.	V_1	V_2	V_3	V_4	V_5	V_6	V_7	V_8
A	0 V	0 V	0 V	0 V	0 V	0 V	0 V	0 V
B	30 V	-30 V	30 V	-30 V	30 V	-30 V	30 V	-30 V
C	50 V	-50 V	50 V	-50 V	50 V	-50 V	50 V	-50 V
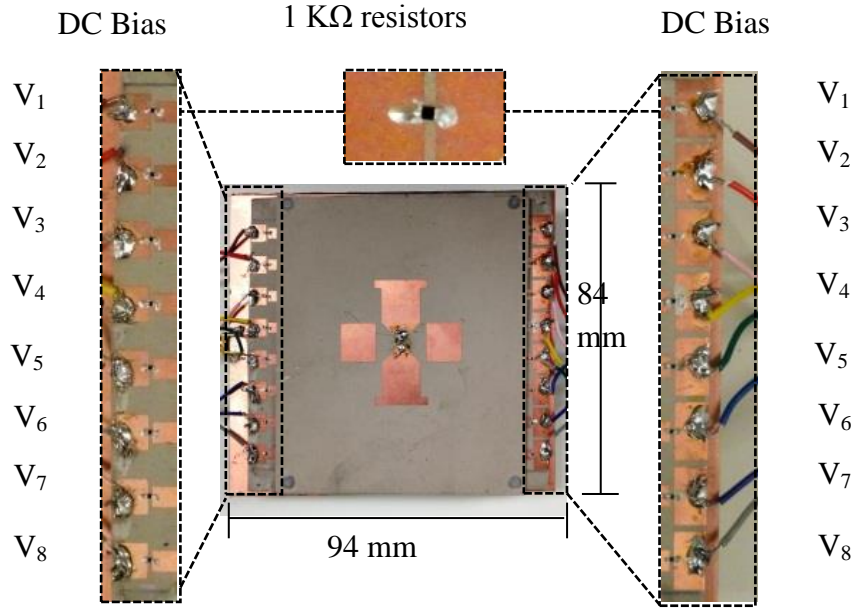
Figure 4.35: Top view of the BSTvaractor based antenna assembly showing 8 independent voltage ports and resistors to isolate the RF leakage from the bias lines.

4.3.2.1. Operation in Free Space

The antenna was simulated and measured using three types of bias configurations; namely, a common bias voltage of 0V (Configuration A), ±30V (Configuration B), ±50V (Configuration C). Measured S_{11} data for the antenna when applying a common bias voltage of 0 V, ±30 V and ±50 V to the DC bias ports are shown in Figure 4.36. Using the 10 dB return loss criterion, there is a 400 MHz span between the low end of the response with 0 V and the high end of the response using 50 V. This span correlates approximately with the ±90° boundaries given in Figure 4.37. As illustrated below, although the return loss bandwidth for Configuration

A covers the entire 400 MHz span, the radiation properties are optimal only near the low end of the band. Additional resonances appear at 2.67 GHz, 2.78 GHz and 2.9 GHz for Configurations A, B and C, respectively, as a consequence of TE surface wave propagation. The resonant frequencies of these modes can be calculated using the cavity model analysis explained in detail in [55]; this analysis predicts a TE resonance at ~2.69 GHz. The dispersion diagram of the unit cell for different capacitance values was simulated using HFSS and it confirms the existence of backward/forward leaky waves at ~2.7 GHz for a capacitance value of 1.4 pF and at ~3 GHz for 0.9 pF. The backward/forward leaky waves are supported in the fast wave region indicated to the left side of the light line shown in Figure 4.37a. Thus, the S_{11} performance of the antenna is not affected by TE surface wave resonances as these occur out of its frequency band of operation. The magnitude of the tangential electric fields of 8 cascaded unit cells for C=1.4 pF at 2.69 GHz (leakage) and at 2.3GHz (no leakage) are depicted in Figure 4.37b.
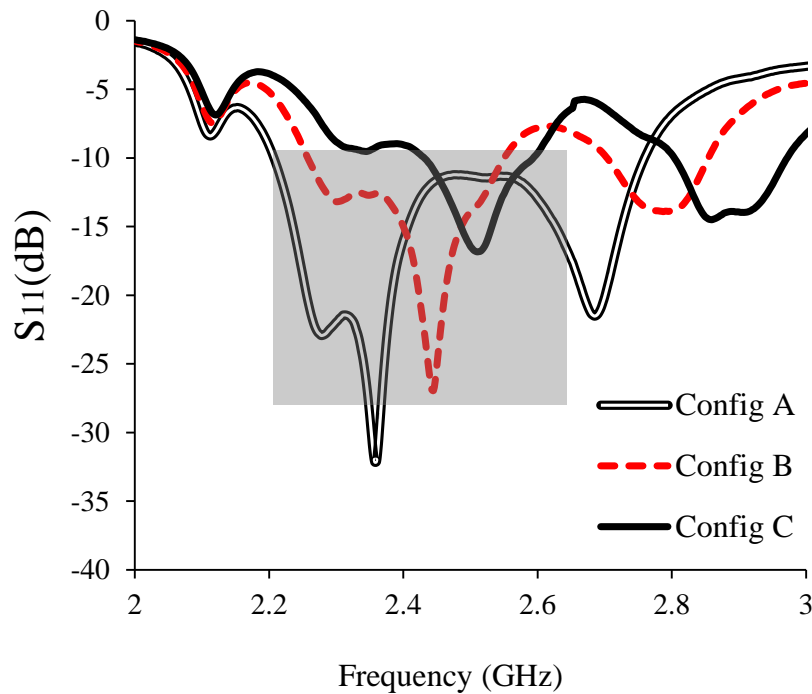
Figure 4.36: Measured S_{11} when 0 V (Config A), ±30 V (Config B), and ±50 V (Config C) is applied to all DC bias lines.
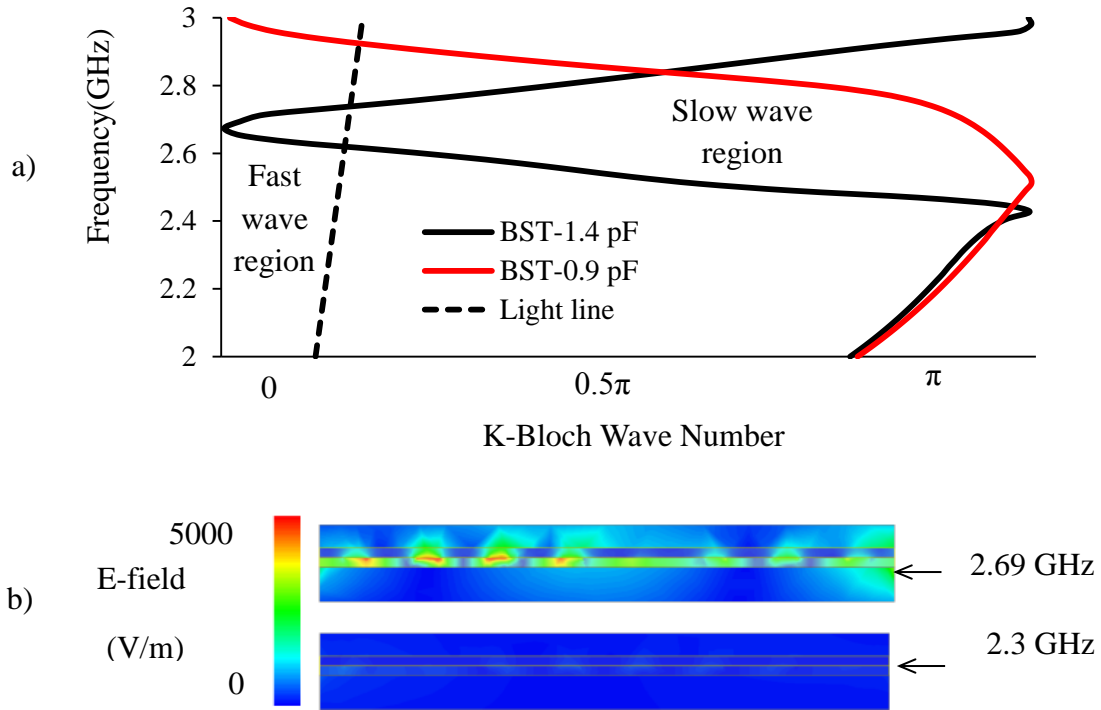
Figure 4.37: (a) Dispersion diagram obtained by cascading 8 unit cells with periodicity of 8.9 mm for C=1.4 pF and C=0.9 pF. (b) Magnitude of the tangential electric fields along the 8 unit cells for C=1.4 pF at 2.69 GHz (leakage) and at 2.3 GHz (no leakage).

Comparisons between simulation and measurement data are given in Figure 4.38. For the simulated results, the capacitance value that provided the best correlation to measurement data at each bias point was offset from the expected value (Figure 4.31) by approximately 0.1 pF; specifically, the expected range from [1.35, 0.92] pF was changed to [1.4, 1] pF. This variation was necessary in order to compensate for potential dielectric variations due to air gaps between the substrate layers of the FSS. A summary of the measured and simulated performance is provided in Table 4.8.
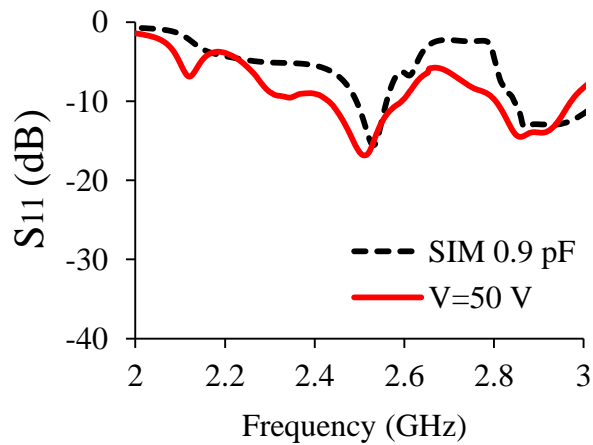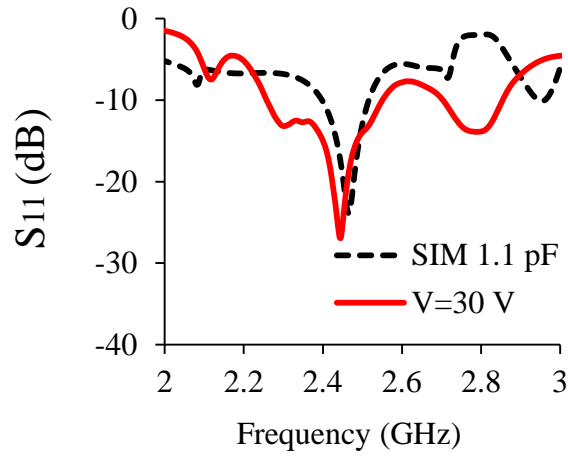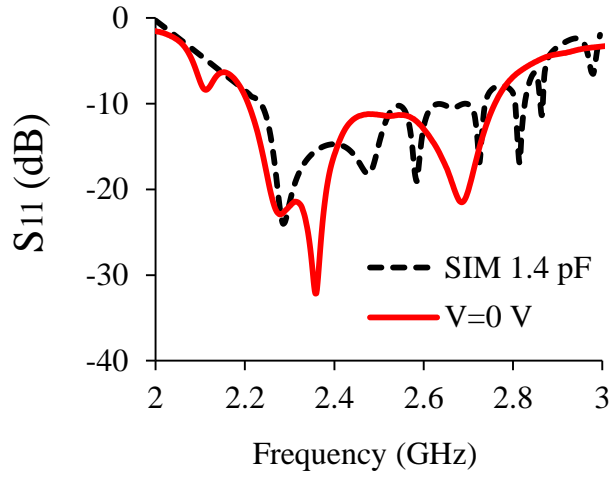
Figure 4.38: Measured and simulated S_{11} when 0 V (Config A), ±30 V (Config B), and ±50 V (Config C) is applied to all bias ports; the voltage across individual diodes is 0, 60 and 100 V, respectively.

Table 4.8: Correlation between gain, voltage and capacitance for the BST based antenna.

BiasVoltage (±V)	0	10	20	30	40	50
Peak gain (dBi)	3	3.2	3.1	3.3	3.6	3.7
3dB gain bandwidth (MHz)	50	80	120	160	120	130
Single diode voltage (±V)	0	20	40	60	90	100
Diode effective capacitance (pF)	1.35	1.22	1.08	0.98	0.92	0.9
HFSS diode capacitance (pF)*	1.4	1.28	1.2	1.1	1.05	1

* Value used in HFSS to obtain best agreement with measured S_{11} data.

Figure 4.39 illustrates the measured antenna gain at broadside for three different values of DC bias. The antenna exhibits a gain of more than 3 dBi from 2.2 GHz to 2.55 GHz when the voltage is varied between 0 V to 50 V. The E-plane radiation patterns of the antenna for different bias voltages are shown in Figure 4.40. The radiation patterns of the antenna with bias voltage of 0 V, ±30 V and ±50 V demonstrate cancellation of back radiation and a high cross-polarization ratio. The fact that there are no leaky waves within the operational frequency band (i.e. from 2.23 GHz to 2.55 GHz) allows good broadside radiation.
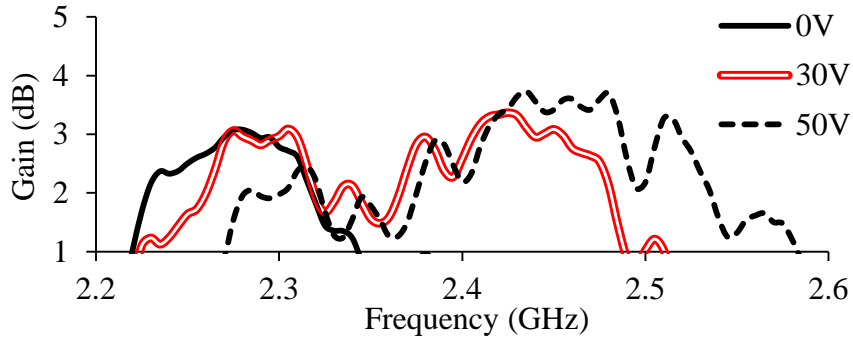
Figure 4.39: Measured gain of the BST varactor based antenna for different bias voltages.

While the bias scheme used in this design accommodates the relatively high DC tuning voltages which are characteristic of planar (interdigital) BST varactors, it limits the ability to adjust or enhance the radiation pattern by changing the bias (see section 4.2.3.2). In the GaAs varactor based antenna presented in section 4.2 the bias could be varied using eight independent voltages in the direction orthogonal to the dipole axis, which affected the coupling to the parasitic sleeves of the ELPOSD. This is also the direction of strong radiation, and because of these two factors it is possible to adjust the radiation pattern by tuning the bias voltage. On the contrary, to induce tuning in this design the bias is changed in the direction parallel to the axis of the dipole, which has less effect on the pattern.
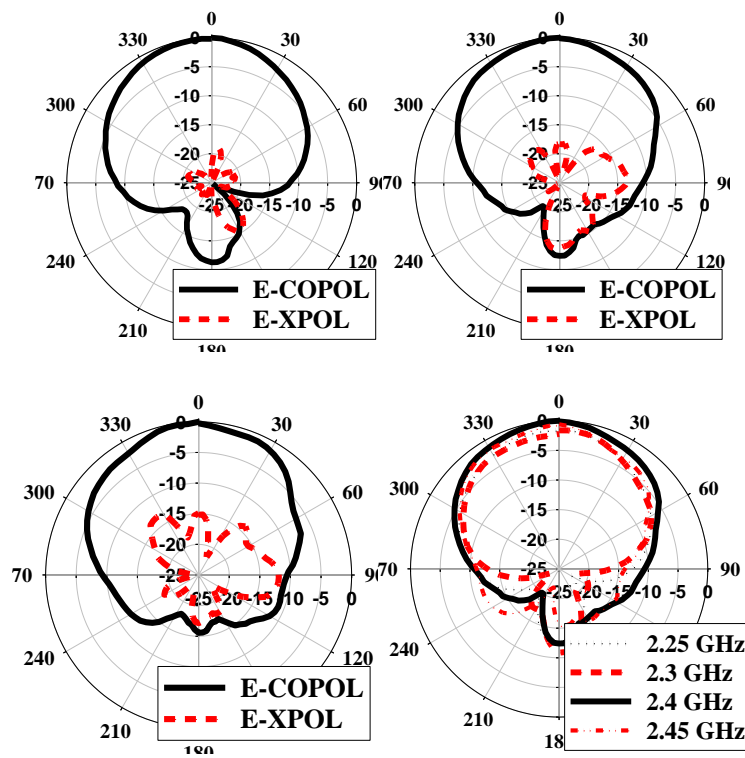
Figure 4.40: Measured E-plane radiation patterns for the BST varactor based antenna with bias voltage of 0 V (top left), ±30 V (top right), ±50 V (bottom left) all at 2.4 GHz and ±30 V at different frequencies (bottom right).

The performance of the antenna is summarized in Figure 4.41. Here, the bandwidth is defined as the band over which the return loss is greater than 10 dB and the gain is more than 2

dBi. For example, at ±30 V applied bias, the center frequency is 2.4 GHz, the bandwidth is 160

MHz and the peak gain at broadside is 3.3 dBi. The shaded region shows tunability from 2.23

GHz to 2.54 GHz (i.e. BW ≈ 310 MHz) with a gain greater than 2 dBi. The gain was determined

using the substitution method [91]. The efficiency of the antenna was measured using a Wheeler

cap and the values obtained were between 30% (0V) and 60% (50V) depending on the voltage.

The gain and efficiency of this antenna are lower than the GaAs based antenna discussed in

section 4.2 possibly due to the losses introduced by the BST varactor, which has lower Q than

the semiconductors diodes at 2.4 GHz. However, the notable size reduction enabled by the BST

varactors together with the reported tunable bandwidth and antenna gain are encouraging results

for biomedical applications such as radiometric sensing, which require small, low-profile, robust,

and continuously tunable antennas. In order to improve these results on the next generation

antenna, adjustment on the substrate thickness could be made to increase the magnitude of the

FSS reflection coefficient and the BST could be fabricated on single crystalline material to

reduce losses [92], [93].
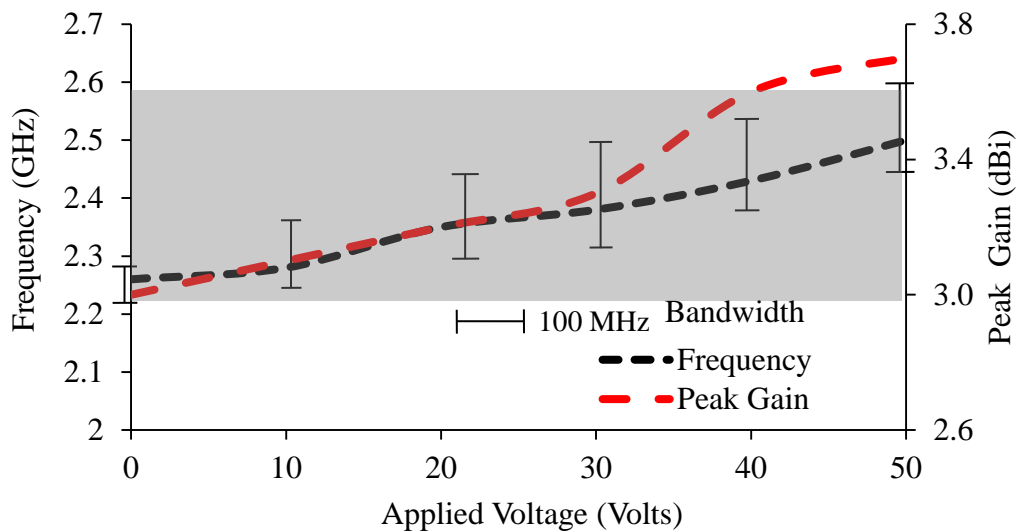
Figure 4.41: Performance of the BST varactor based antenna versus bias voltage.

97

4.3.2.2.   Operation in the Presence of Human Core Model

Similarly as previously shown with the GaAs varactor based antenna in section 4.2.3.3, in this section the BST varactor based antenna performance is also characterized in the presence of the human core model (HCM) phantom [85] (Figure 4.23). Thus, the HCM was placed in contact and at distances up to 15 mm from the antenna, given that experiments performed at USF using a 1.4 GHz planar antenna showed that the impedance measured at the antenna input varied as Z = (60±30) + j(-70±70) Ω over a distance of 0 to 15 mm from a human hand [85]. A Planar view of both antennas is shown in Figure 4.42.

a)   b)
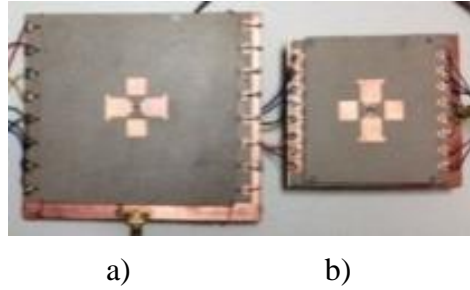
Figure 4.42: Planar size comparison for a) GaAs based tunable antenna and b) BST based tunable antenna.

Table 4.9: FSS bias configurations in presence of HCM for the BST based antenna.

Config.	V_1	V_2	V_3	V_4	V_5	V_6	V_7	V_8
A	0 V	0 V	0 V	0 V	0 V	0 V	0 V	0 V
B	30 V	-30 V	30 V	-30 V	30 V	-30 V	30 V	-30 V
C	50 V	-50 V	50 V	-50 V	50 V	-50 V	50 V	-50 V
D (15 mm)	30 V	-30 V	30 V	-30 V	30 V	-30 V	30 V	-30 V
E (15 mm)	13 V	-17 V	17 V	-17 V	17 V	-17	17 V	-13 V
F (15 mm)	0 V	0 V	0 V	0 V	0 V	0 V	0 V	0 V
G (15 mm)	40 V	0 V	40 V	0 V	40 V	0 V	40 V	0 V
H (0 mm)	15 V	-15 V	15 V	-15V	15 V	-15 V	15 V	-10 V
I (0 mm)	10 V	-10 V	10 V	-10 V	10 V	-10 V	10 V	-10 V

Previously in section 4.2.3.3 as well, it was demonstrated that the tunability of the GaAs-based antenna successfully corrected for impedance mismatch introduced by the HCM at varying offsets, from 2.2 to 2.8 GHz. The BST varactor based antenna was subjected to the same test and similar performance was achieved. Figure 4.43 shows that with a uniform voltage of 30 V on all rows of the FSS and in free space (Configuration B in Table 4.9), the antenna has a good impedance matching from 2.26 GHz to 2.52 GHz. When the HCM is placed at a 10 mm offset from the face of the antenna (Configuration D), the S_{11} response is changed as depicted in Figure 4.43. However, by adjusting the bias voltage at the input lines (Configuration E), the impedance match can be improved. This antenna also demonstrates that when HCM is in contact with the antenna, the impedance matching can be also improved (H and I). The characteristics of the two antennas are summarized in Table 4.10.
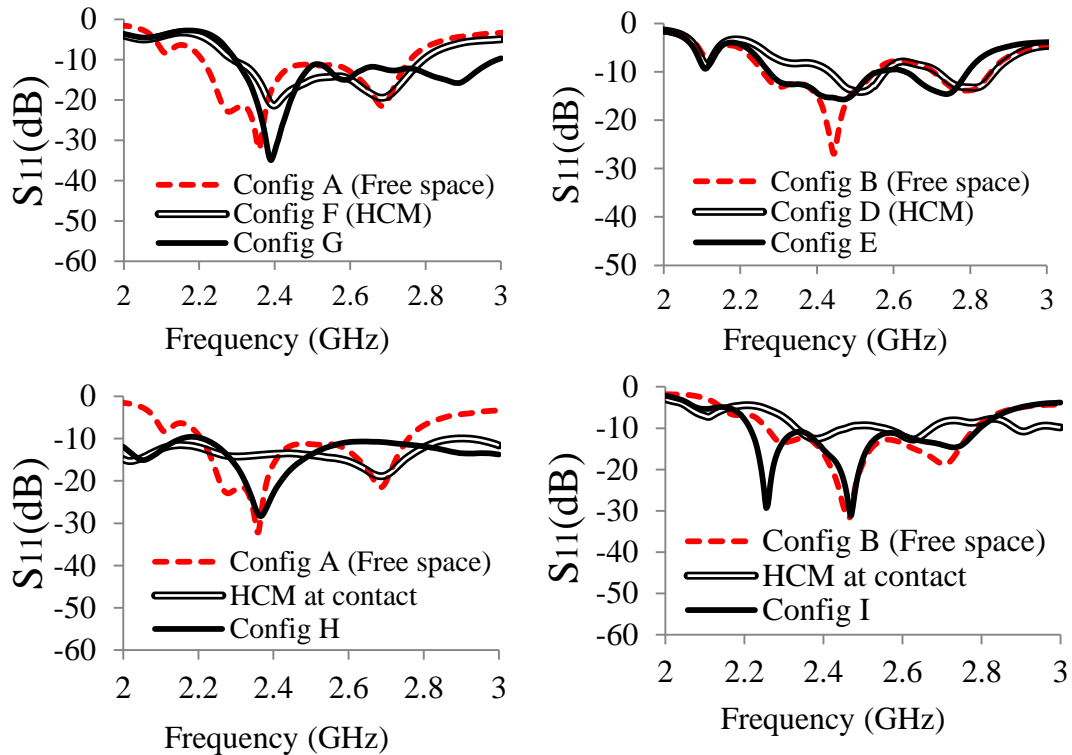
Figure 4.43: Measured S_{11} of the antenna in free space, in the presence of the HCM at contact with the antenna (Bottom) and 15 mm separation (Top) distance when different biases are applied to the diodes.

Table 4.10: Antenna comparison.

Antenna	Mass (gms)	Total devices	Cost per device	Cost	Area (mm^2)	Eff. (%)	Tunable BW (MHz)
GaAs	188	56	50 US$	High	15600	50-80	520
BST	87	56	0.1 US$	Low	7900	30-60	425

4.4.   Summary and Conclusion

The use of a varactor-tuned frequency selective surface with an ELPOSD antenna has been presented. The reduction of interlayer wiring on the electronically-tuned FSS minimizes the fabrication complexity and facilitates the potential use of flexible substrates for future works. The antennas are ultra-thin ($\sim\lambda/45$); they have low back lobes of the radiation patterns and allow adjustment in response to adverse environmental loading making this design amenable to biomedical radiometric sensing applications. The measured data demonstrate that both antennas can be tuned from approximately 2.2 GHz to 2.6 GHz with high gain and broad bandwidth.

Two different bias network configurations were explained. The bias scheme of the GaAs varactor based antenna consisting in eight independent DC voltage lines, each line having seven GaAs chips in series, allows the possibility to enhance the radiation pattern by adjusting the DC bias. The bias scheme of the BST varactor based antenna allows reducing the bias voltage needed into the lines and takes advantage of the symmetric behavior along the zero-bias voltage axis in the BST C-V curve.

A comparison of the BST varactor and GaAs varactor based antennas was also presented. The main advantages of the BST varactor based antenna are the planar size and mass reduction which are desirable features for portable applications. The BST varactor based antenna has lower radiation efficiency than the GaAs varactor based design, due primarily to the lower Q factor of the BST varactors ($\sim$11 at 2.4 GHz compared to $\sim$200 for GaAs). Although the lower efficiency

could compromise the noise figure of the radiometer and reduce its sensitivity, the design is highly cost effective, compact, robust, easily tunable and low profile.

CHAPTER 5: FLEXIBLE TUNABLE HGH IMPEDANCE SURFACE BASED LOW PROFILE ANTENNA

5.1.   Introduction

Previous chapters discussed various antenna designs fabricated over commercially available substrates. Most of the problems imposed by the close proximity of the radiometric sensor have been addressed. In addition, a path towards achieving flexibility has been prepared. This chapter presents the design, fabrication and analysis of flexible antennas. The selection of the flexible material stack was based on initial results using grooves in rigid commercial substrates which suggested the use of alternative materials to achieve flexibility (see Appendix D for technical details and Appendix G, section G.4 for copyright permission). The material characterizations as well as the fabrication processes of these antennas are explained in detail. Thus, first, the development of a flexible electrically-thick polydimethylsiloxane (PDMS)/liquid crystal polymer (LCP) microstrip antenna at 4.0 GHz is presented. Designs in previous chapters were done at 2.4 GHz. In this chapter the frequency was increased to 4 GHz to reduce the antenna size, material volume and cost. A microstrip antenna topology was selected as it offers a well-known performance using commercial substrate, low profile, low cost and simple fabrication process. The extraction of electrical and mechanical properties for the flexible material as well as a detailed fabrication process is explained. Subsequently, a flexible low profile dipole antenna using a frequency selective surface (FSS) with interdigital barium strontium titanate (BST) varactor-tuned unit cells is explained. The antenna uses overlapping

metallic plates that resemble fish scales as a ground plane to improve the flexibility of the multi-material stack structure.

5.2. Flexible Electrically-Thick PDMS/LCP Microstrip Antenna

In recent years antennas on various types of flexible substrates have been developed for applications ranging from medical implants to structural health monitoring [23]-[26]. Herein, the development of a flexible PDMS/LCP based antenna at 4.0 GHz is presented (Figure 5.1). The PDMS layer is sandwiched between two commercial ULTRALAM 3850 LCP layers, on which the copper ground plane and microstrip antenna are patterned using photolithography. The LCP and PDMS layers are bonded together using segmented (non-continuous) SU8-5 layers treated with (3-Aminopropyl)triethoxysilane (APTES). In addition, a novel design using a slotted ground structure (SGS) to enhance flexibility of the multi-material stack is implemented.
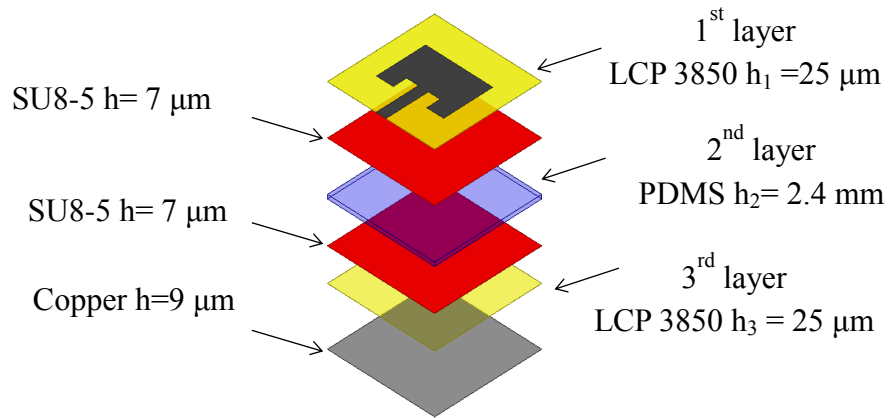
Figure 5.1: 3D schematic diagram of the multilayer microstrip patch antenna identifying each layer and its thickness.

This design approach is intended to enable the development of low profile antennas for biomedical radiometric sensing where the sensor may be embedded in uniforms, prosthetic devices, or other body-worn protection [21]. For this type of electromagnetic sensing, reduction in the back lobes of the radiation pattern is important in order to maximize the detection

sensitivity and thus the use of a backing ground-plane is appropriate. However, the two metal layers limit flexibility since the top (radiator) and bottom (ground) copper layers have the highest modulus of elasticity in the antenna structure and are the farthest materials from the neutral bending axis. For this reason the composite structure will most likely fail at either the top or bottom copper layers. As discussed in previous chapters of this thesis and in [21], antennas have been demonstrated that can be used for portable biomedical applications using a varactor-based tunable FSS which allows adjustment in response to adverse near-field loading. However for these antennas the electrical performance (i.e. matching, gain, efficiency, bandwidth, etc.) improves as the antenna thickness increases. Hence, the challenge resides in selecting appropriate physical parameters based on sound engineering principles to achieve good mechanical flexibility while maintaining high antenna efficiency.

Recent publications in flexible antenna design have demonstrated the use of ultra-thin layers of PDMS (20 to 200 μm) as a possible approach to designing flexible electronics and MEMS devices [37]-[42]. One of the advantages of PDMS is its bio-compatibility. Unfortunately, its inherent hydrophobic properties prevents this material from adhering easily to others (e.g., LCP, copper, etc.). In [27] and [41] the SU-8 was treated with APTES and plasma etching to create an intermediate layer and bond two or more layers of PDMS. In [28] a thin SU-8/PMDS flexible antenna was fabricated using metal deposition on sacrificial layers which were later transferred to the PDMS to keep it from high temperature stress. In [36] a patch antenna encapsulated in a PDMS/LCP substrate is shown, which avoids the use of transferring layers or metal deposition. The encapsulation releases the metal layers from maximum stress and strain, as they are not anymore the farthest layers from the neutral axis. However, the latter approach increases the antenna profile, degrades its performance and does not provide a permanent

solution to the LCP/PDMS adhesion problem as eventually air bubbles appear between the layers and the LCP is delaminated. In [35] PDMS was mixed with ceramic powder to create a blended polymer–ceramic which was used to investigate the performance of metal epoxy-printed patch antennas. However the brittle nature of metal epoxy makes this approach susceptible to cracks. To the best of the author's knowledge, none of the previous works address the challenges of building electrically-thick, robust and flexible microstrip antennas.

The following sections present the design, fabrication and bending test of a flexible microstrip antenna using commercially available, copper-clad LCP substrates and an electrically-thick PDMS layer. A method for permanent bonding between PDMS and LCP is demonstrated for the first time, featuring a shorter curing time for the fabrication of the blended material than that required in previously published processes. Additionally, a new design using a slotted ground structure (SGS) to enhance the flexibility of the multi-material stack is implemented. The 4 GHz antenna has a maximum gain at broadside of ~3 dBi when unbent and a maximum change of ±2 dB upon exposure of the antenna to stress and strain.

5.2.1.   Antenna Design and Fabrication

5.2.1.1. PDMS-Ceramic and LCP Materials

Prior to implementing the multi-layer antenna design the fabrication process for the blended PDMS-ceramic material was optimized and the high frequency electrical properties were determined. The PDMS type selected for this design was Sylgard 184 from Dow Corning which has been widely used for microwave applications [23], [35]-[36]. The ceramic powder used for loading the PDMS was the ultra-low fire UFL990 from Ferro Corp, which has a high dielectric constant (~90), small particle size (0.4 μm) and low loss material.

Prepare PDMS silicone gel   Add cure agent (10:1)   Degas for 10 minutes

Add ceramic powder and
mix (5 minutes at 2000)
rpm)

Degas for 30 min
at 76 cm Hg

Pour the mixture
into a container and
degas for 30 min

Cure for 1 hour at 100^0 C   Refrigerate for 10 min and peel off
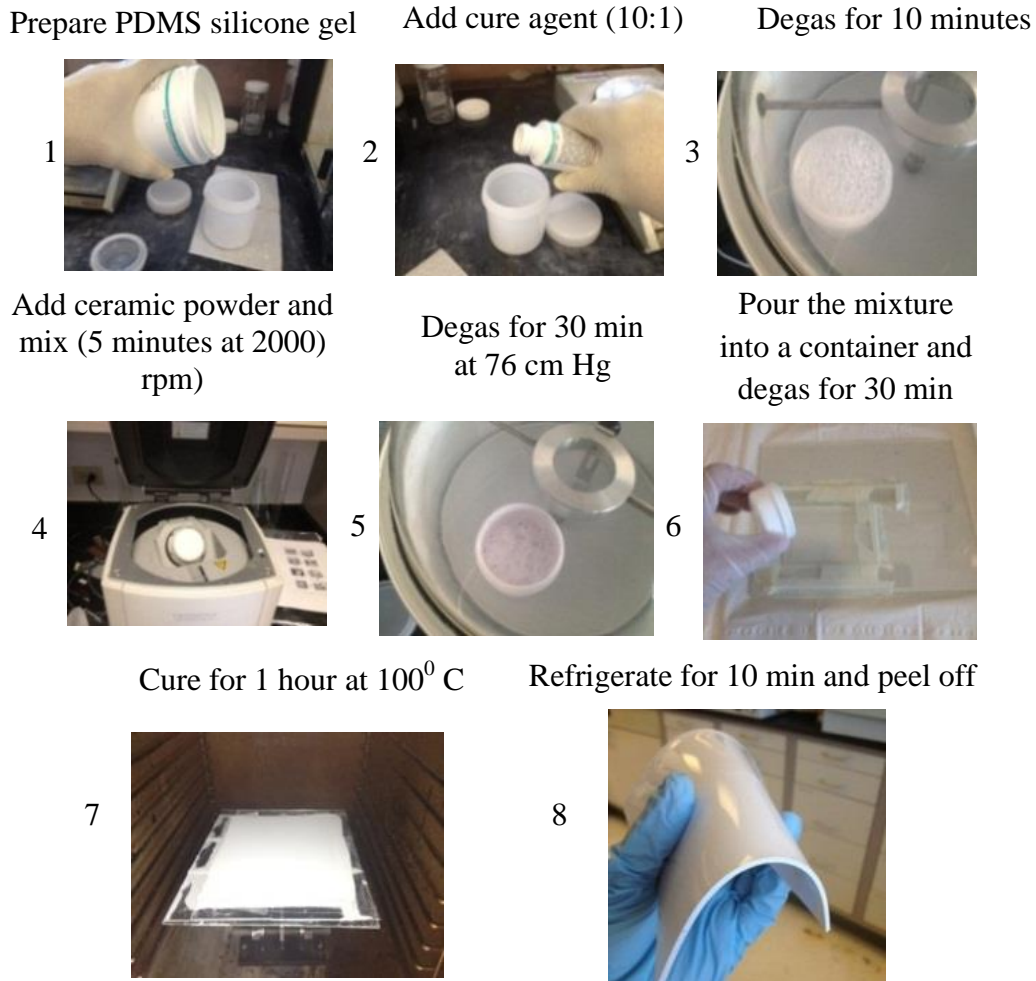
Figure 5.2: Fabrication process for PDMS-ceramic composite.

Figure 5.2 shows pictures outlining the fabrication steps. The process starts with the preparation of the PMDS by adding base and curing agents that are mixed in a ratio of ten parts base to one part curing agent. The resulting silicone gel is placed into a vacuum chamber for 10 to 30 minutes depending on the amount of PDMS. In order to speed up the degas process the valve of the chamber is briefly opened every five minutes to allow air to flow. Once all bubbles are removed from the PDMS, the UFL990 ceramic powder is added to the degassed silicone gel with the desired percentage volume ratio and mixed for 5 minutes at 2000 rpm; the volume ratio formula and calculation are explained in detail in [35]. Then the PDMS-ceramic mixture is again

degassed using the same process for 30 minutes at 76 cm Hg and poured into a glass container; the short interval approach reduces the total degassing time (from step 1 to 7) from 3 hours (as in [35]) to approximately 1 hour and 15 minutes. A final degassing step is performed after which the mixture is cured for 1 hour at 70° Celsius. The curing time can be reduced by increasing the curing temperature (e.g. 35 minutes at 130° C). The glass container is refrigerated for 10 minutes after curing to facilitate peeling off the substrate. In [35] the curing time of 24 hours was necessary because it was performed at room temperature.

The high frequency properties of the materials were measured using an Agilent 4291B RF impedance/material analyzer and 16453A dielectric material test fixture. An open/short/load calibration was performed up to the Agilent 4291B test head and then the 16453A test fixture calibration kit was connected. A second open/short/load calibration using a Teflon sample of 0.78 mm thickness and relative permittivity of $\varepsilon_r=2.1$ was carried out to calibrate the test fixture. Figure 5.3a shows the dielectric constant for different volume ratios. PDMS has a dielectric constant of ~3.0; by adding 10%, 20% and 30% of ceramic powder the dielectric constant increases to 4.5, 7.0 and 9.5, respectively. Figure 5.3b shows the extracted loss tangent for different percentages. At 1 GHz the PDMS has a loss tangent of approximately 0.013 and by adding 20% ceramic powder the loss tangent was reduced by 30% (~0.009). For 30% volume ratio the material losses increase, possibly due to the difficulty of creating a uniform mixture. These values are similar to the ones extracted in [35], demonstrating that reducing the fabrication time did not affect the electrical properties of the material as shown in Figure 5.3c. However, the rigidity of the material, as indicated by the measured Young's modulus, increases as the powder concentration and the curing temperature increased (Figure 5.3d).
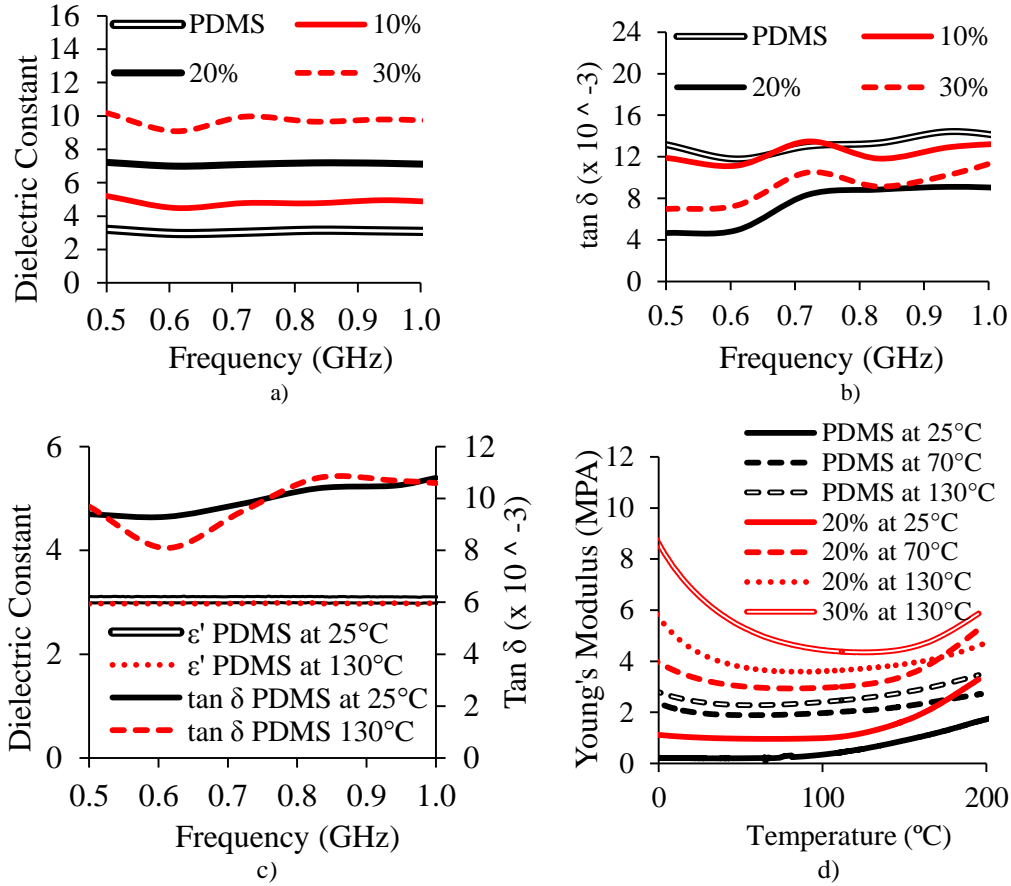
Figure 5.3: (a) Dielectric constant and (b) loss tangent for the PDMS-ceramic samples at different volume ratios. (c) Dielectric constant and loss tangent vs. frequency the PDMS samples cured at different temperatures (d) Young's modules for PDMS-ceramic samples cured at different temperatures.

The LCP type used in this design was ULTRALAM 3850 which has a low dielectric constant and low dielectric loss (ε_r=2.9 and tanδ = 0.0025). The LCP layer thickness is 25 μm with double-side copper cladding of 9 μm on which the radiator and the ground plane were patterned using photolithography [94]. The PDMS has an average thickness of 2.5 mm. The LCP and (blended) PDMS were bonded together using SU8-5 photoresist as an intermediate layer [27]-[28], [41]. The SU8-5 was spun onto the LCP at 2000 rpm (~7 μm thickness), then exposed and developed following manufacturer specifications. The SU8-5 was then treated with APTES as explained in [28], [41], [95]. Separately, the PDMS substrate was exposed to oxygen plasma at 10 W, 50 standard cubic centimeters per minute (sccm) for 30 seconds. The LCP and PDMS

were aligned with respect to each other and pressed together in a vacuum oven at 70°C for 3 minutes to create a permanent bond between the two materials.

5.2.1.2. Bending Test

The multi-layer antenna was exposed to different bending pressure points to assess its response to mechanical stress and strain. One of the challenges of these types of antennas is that the materials generally have different elasticity properties. When bending this structure, the printed radiator on the top LCP layer will experience positive bending moment (positive radius of curvature) while the ground plane on the bottom LCP layer experiences a negative bending moment (negative radius of curvature). In addition, in order to obtain the desired flexibility for the antenna, the thickness of the substrate needs to be kept at a minimum, as the stiffness is directly proportional to the cube of the thickness [34]. However, for the intended application considered in this thesis, the optimal thickness of the substrate is selected to increase the radiation efficiency and bandwidth [21].

As shown in Figure 5.4a and Figure 5.4b, the elastic response to negative bending moments (negative radius of curvature) does not affect the bonding between the materials because the copper is still under its deformation limits. In contrast, Figure 5.4c and Figure 5.4d demonstrate that positive bending moments produces detachment of the layers because the top surface is experiencing wrinkling, which correlates with high plastic deformation. In addition, the copper experiences maximum strain because it is the farthest of the three materials from the neutral axis. When the bending load is released, the copper does not return to the original shape because it is plastically deformed (notice Figure 5.4c). The copper modulus of elasticity is much higher than the polymer modulus (117 GPa for copper versus 1.2 MPa for the polymer), while the elastic strains in the copper are much smaller (0.06-0.3%) than in PDMS (80%) and PDMS-

109

ceramic (greater than 15%). Therefore, even though the strains in the copper and PDMS are the same at the interface, the copper yields plastically. Once the copper is plastically strained due to the deformation, large interfacial stresses are generated at the copper/PDMS interface on straightening or reversing the direction of bending deformation. This stress results in delamination of the copper (along with the LCP) from the PDMS.
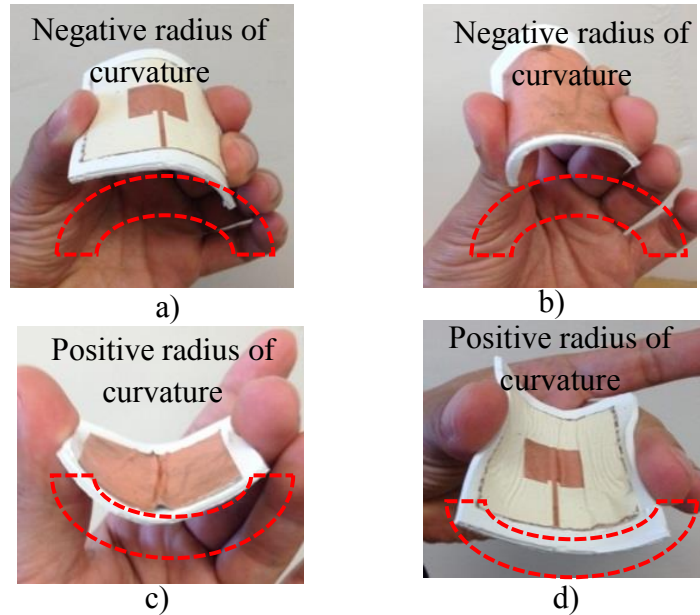
Figure 5.4: PDMS/LCP microstrip patch antenna. (a) Top of the antenna bent forming a negative radius of curvature; (b) bottom of the antenna bent forming a negative radius of curvature; (c) bottom of the antenna bent forming positive radius of curvature; (d) top of the antenna bent forming a positive radius of curvature.

5.2.1.3.   Antenna with a Slotted Ground Structure (SGS)

In this section segmented patterns in the SU8 layers and a novel SGS are demonstrated to improve the flexibility of the antenna. Meshed ground planes have been used to fabricate flexible printed circuit boards (PCB), while slotted ground structures have been used to enhance the performance of microstrip antennas [96], [97]. The presented design takes advantage of a SGS to increase the safe-limit radius of curvature of the ground plane. In a similar fashion, the SU8 layers are patterned into a square grid (segmented) to increase their flexibility as result of the high modulus of elasticity of the SU-8 when is hard baked (~ 5GPa). The new design also

minimizes the stress by reducing the areal dimension of the LCP on the top layer. The dimensions of the ground plane were held constant (72 mm x 72 mm) relative to the first design.

Figure 5.5 shows the 3D version of the antenna along with the surface current distribution. The dimensions of the microstrip patch are 14.5 mm by 23.5 mm, and the top LCP layer extends approximately 5 mm beyond the patch. The radiator was located at the center of the substrate. The SU8-5 layer was patterned using a grid of 4 mm x 4 mm squares separated by 1 mm spacing. To realize the SGS and increase flexibility for two pressure points, 0.05 mm-wide cuts parallel to the feed line were introduced into the ground plane. V-shaped cuts were also made in the ground to increase flexibility for 4 pressure points. Lateral cuts were not used in order to prevent the creation of surface current paths which can alter the electrical performance of the antenna [98]. The separation distance between the vertical lines and spaces between patches were determined by performing optimization using Ansoft's High Frequency Structural Simulator (HFSS). As shown in Figure 5.5 the surface current distribution demonstrates minimal leakage due to the use of the SGS. Figure 5.6 depicts the fabricated SGS bottom layer and the top-view schematic of the multilayer antenna identifying its dimensions. The final antenna dimensions are provided in Table 5.1.
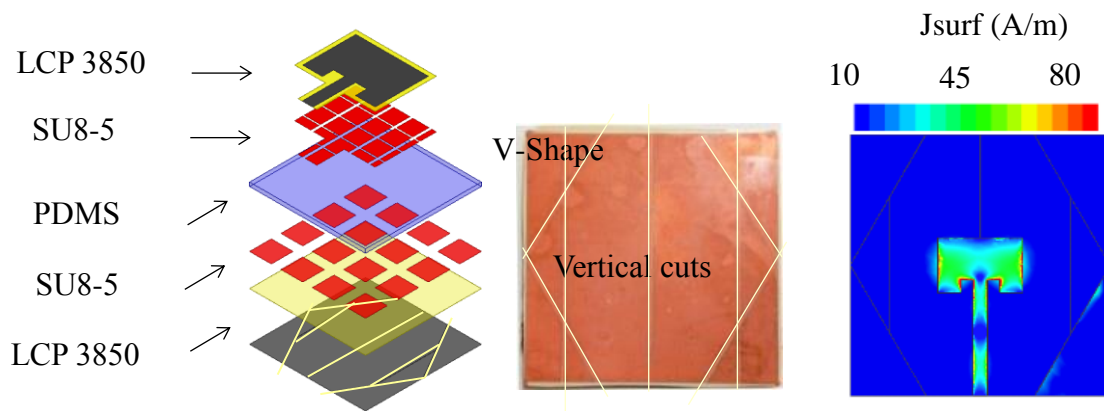
Figure 5.5: 3D schematic diagram of the multilayer microstrip patch antenna using a SGS (left), view of the ground plane (center) and the surface current density distribution (right).
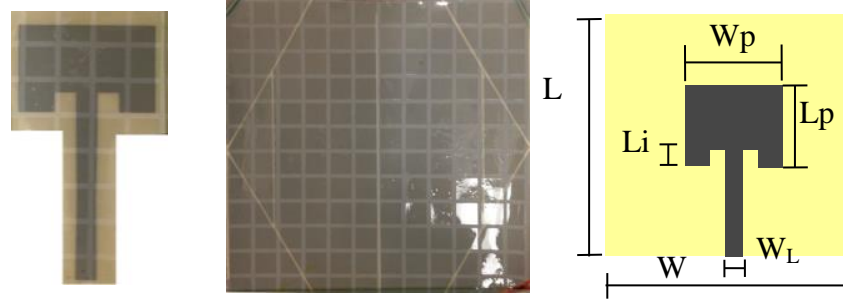
Figure 5.6: Segmented SU8-5 patterns (left and center) and top-view schematic of the multilayer antenna identifying its dimensional parameters (right).

Table 5.1: Antenna dimensions.

Material	*W*	*L*	W_p	L_p	W_L	L_i
RT/duroid® 5880	72	72	30	24.5	5	6.5
PDMS	72	72	30	22	6.6	4.4
PDMS-ceramic	72	72	23.5	14.7	3.8	3.2

* All dimensions are in mm

Figure 5.7 show S_{11} for the unbent antennas fabricated with PDMS and 20% ceramic powder/PDMS, with and without the SGS. The measured S_{11} of the unbent antennas using the SGS results are in good agreement with the simulations results. Figure 5.8 shows the radiation patterns for the unbent antennas. For comparison purposes a 2.5 mm-thick microstrip antenna using a commercial substrate RT/duroid® 5880 ($\varepsilon_r = 2.2$ and $\tan\delta = 0.0004$) was designed, built and tested at the same frequency. The measured gains using RT/duroid® 5880, PDMS and PDMS-ceramic were approximately 5 dBi, 2.45 dBi and 3.1 dBi, respectively. The gain using the SGS was 2.4 dBi for the PDMS design and 3 dBi for the PDMS-ceramic design. These results show a gain drop of 2 dB when using the PDMS-ceramic substrate with respect to the RT/duroid® 5880 antenna primarily due to its higher loss tangent. This agrees with the simulation results performed using Ansoft's HFSS which estimate a gain drop of 1.5 dB when the loss

tangent of substrate decreases by one order of magnitude. The gain was determined using the substitution method and the results are shown in Figure 5.9. The efficiency of the antennas was measured using a Wheeler cap and the values obtained were 78% for RT/5880, 48% for PDMS-SGS and 55% for PDMS-ceramic-SGS. Figure 5.10 depicts the top view of the RT/duroid® 5880, PDMS and PDMS-ceramic antennas.
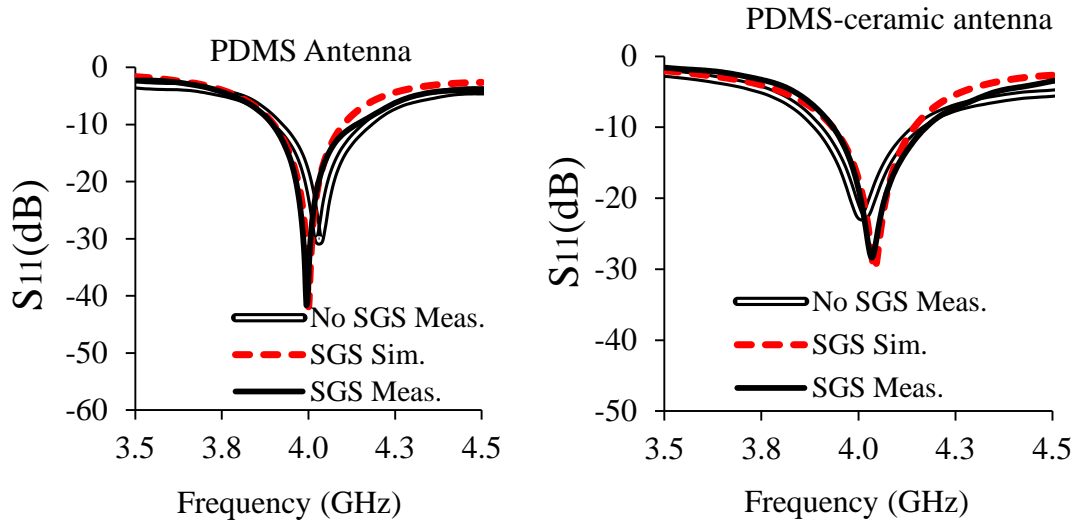
Figure 5.7: Simulated (with SGS) and measured S_{11} of the unbent PDMS microstrip patch antenna with and without SGS (left) and unbent PDMS-ceramic/SGS microstrip patch antenna with and without SGS (right).
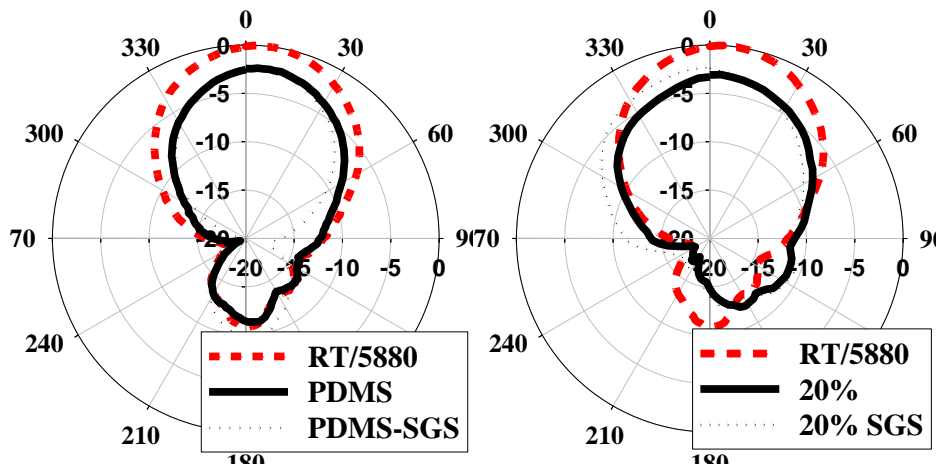
Figure 5.8: Measured H-plane radiation patterns for unbent antennas at 4GHz using different substrates: RT/duroid® 5880, PDMS, PDMS-SGS (left) and RT/duroid®5880, PDMS-20% ceramic, PDMS-20% ceramic-SGS (right).
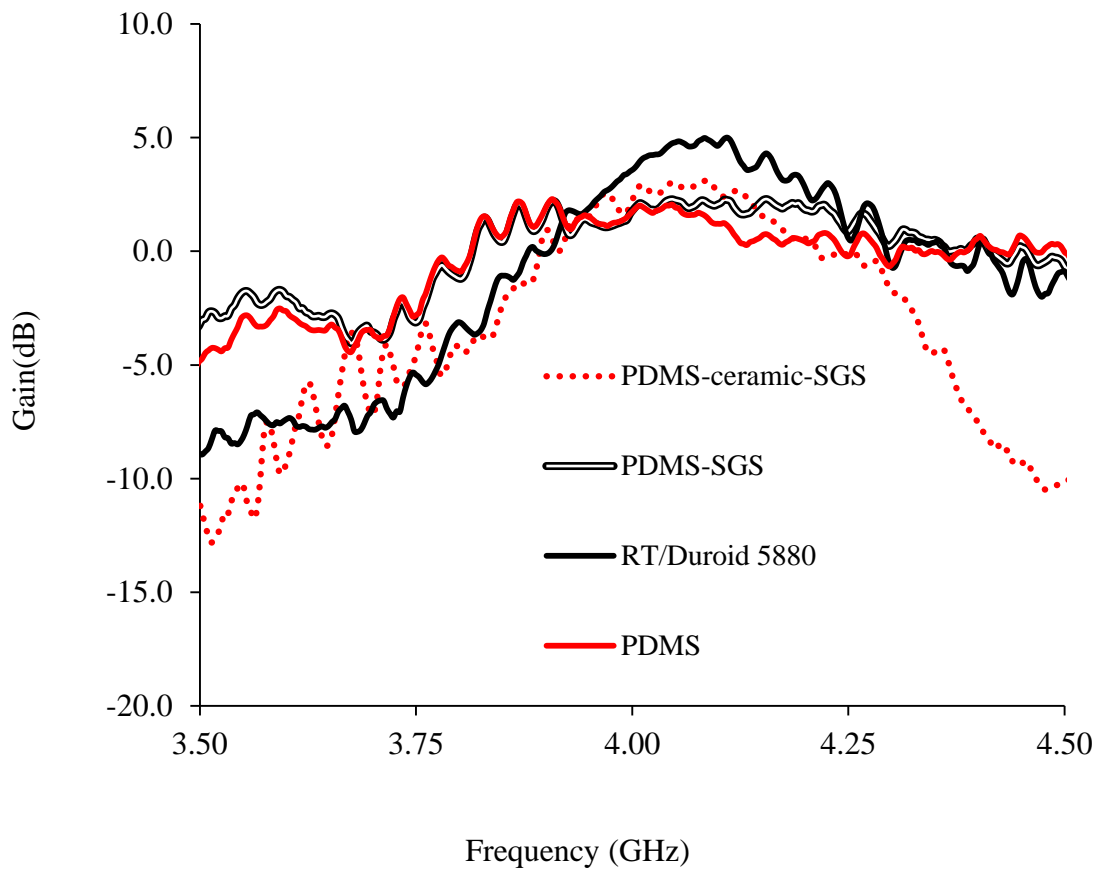
Figure 5.9: Measured gain of the RT/duroid® 5880, PDMS, PDMS-SGS and PDMS-20% ceramic-SGS microstrip antennas.
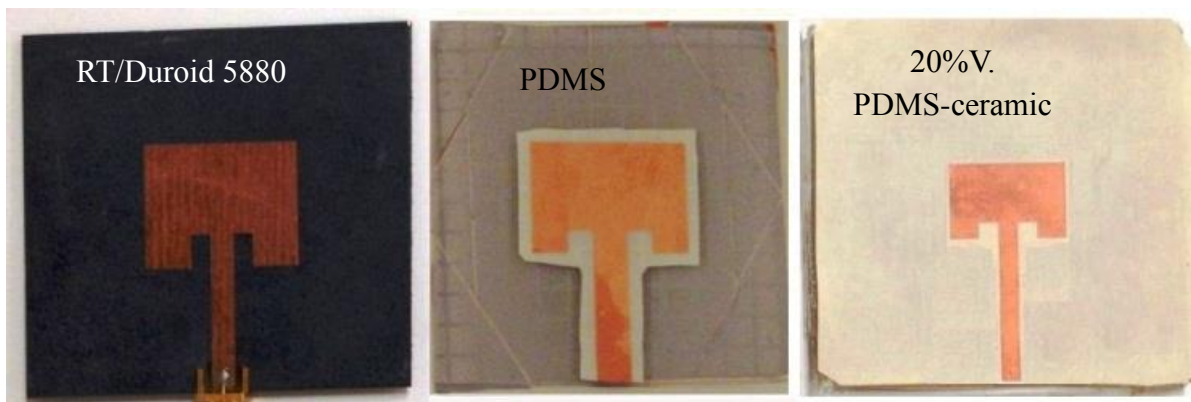
Figure 5.10: Planar size comparison for different antennas.

5.2.1.4. Antenna Performance and Bending Test

In this section the mechanical and electrical performance of the proposed antenna are evaluated when it is exposed to stress and strain. Figure 5.11 shows the antenna bent using different scenarios. The antenna demonstrates a reduction in the bending stress/strain and improvement in the flexibility of the ground plane due to the use of the SGS and the segmented pattern in the SU-8 layers, in comparison to the antenna depicted in Figure 5.4. The flexibility was tested for 1 to 4 pressure points. Given the direction of the cuts in the ground plane, the presented antenna design is not intended to accommodate torque that is perpendicular to the feed line.

Styrofoam cylinders of 25, 50 and 76 mm radius were used to perform the bending tests. The angle of curvature was determined using (5.1) which defines the central angle whose vertex is the center of a circle.

$$\theta(radians) = \frac{L}{r} \qquad\qquad (5.1)$$

where L is the length of antenna (72 mm) and r the radius of the cylinder.

Figure 5.12 shows the measured S_{11} and radiation pattern data for the PDMS-ceramic/SGS antenna when the antenna is unbent and bent in a negative radius of curvature for different angles. This bending broadens the H-plane pattern and the back radiation; accordingly, the gain drops by 0.4 dB, 0.8 dB and 1.3 dB for angles of 55º, 80º and 162º , respectively. The frequency shifts by only 15 MHz (0.35%) when the angle is 162º. The dependence of the gain on the angle of curvature is similar to that demonstrated for axially-polarized slot antennas mounted on cylinders [99].

115
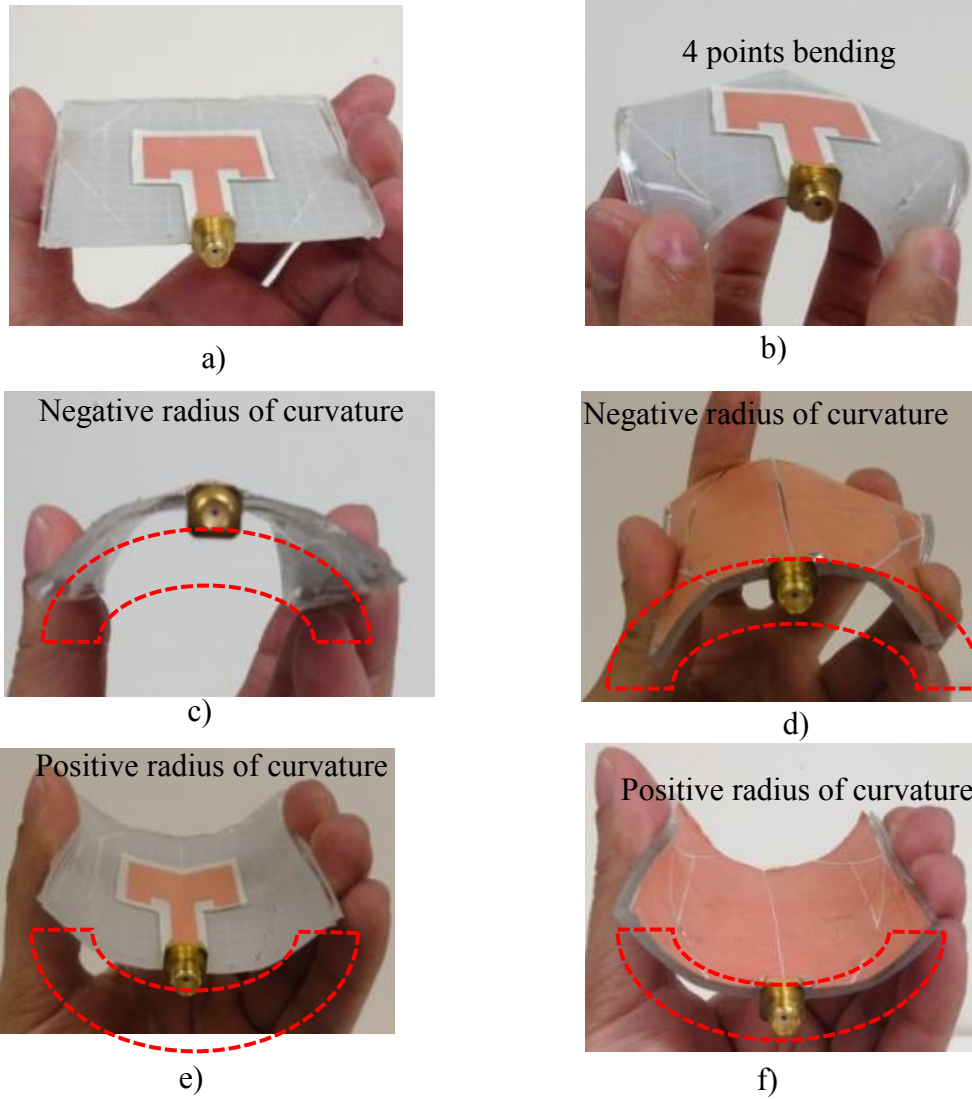
Figure 5.11: PDMS based microstrip patch antenna using a SGS. (a) Unbent antenna; (b) 4 pressure point test (c) top of the antenna bent forming a negative radius of curvature; (d) bottom of the antenna bent forming a negative radius of curvature; (e) top of the antenna bent forming a positive radius of curvature; (f) bottom of the antenna bent forming positive radius of curvature.
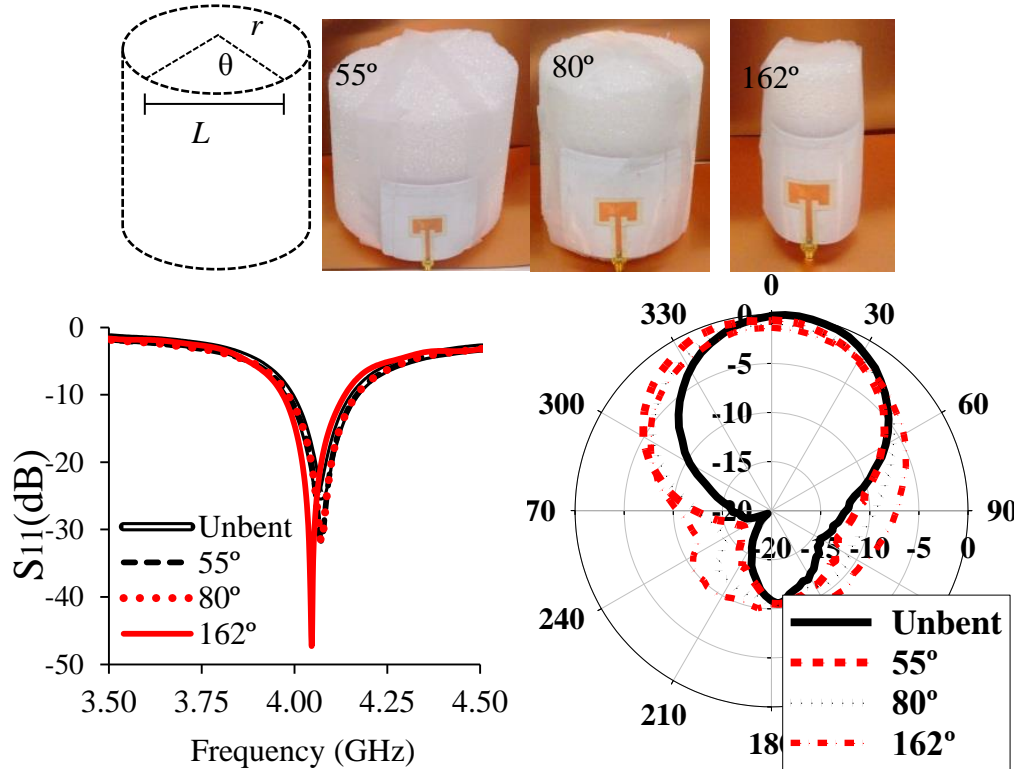
Figure 5.12: Measured S_{11} of the PDMS-ceramic-SGS microstrip patch antenna under different angles of negative curvature (left) and the corresponding H-plane radiation patterns at 4 GHz (right).

Figure 5.13 shows the measured S_{11} and radiation patterns for the PDMS-ceramic-SGS antenna when the antenna is unbent and bent in positive radius of curvature for different angles. The bending produces a frequency shift of 50 MHz (1.2%) when the angle is 162º. The gain increases by 0.4 dB, 1 dB and 2 dB for angles of 55º, 80º and 162º, respectively, for this type of bending. This gain increase is realized because there is less back radiation as the angle increases and the ground plane curves toward the patch direction. For angles greater than 162º the PDMS-ceramic antenna exhibits similar gain (5dB) as the one fabricated in RT/duroid 5880, but with a smaller back-lobe.
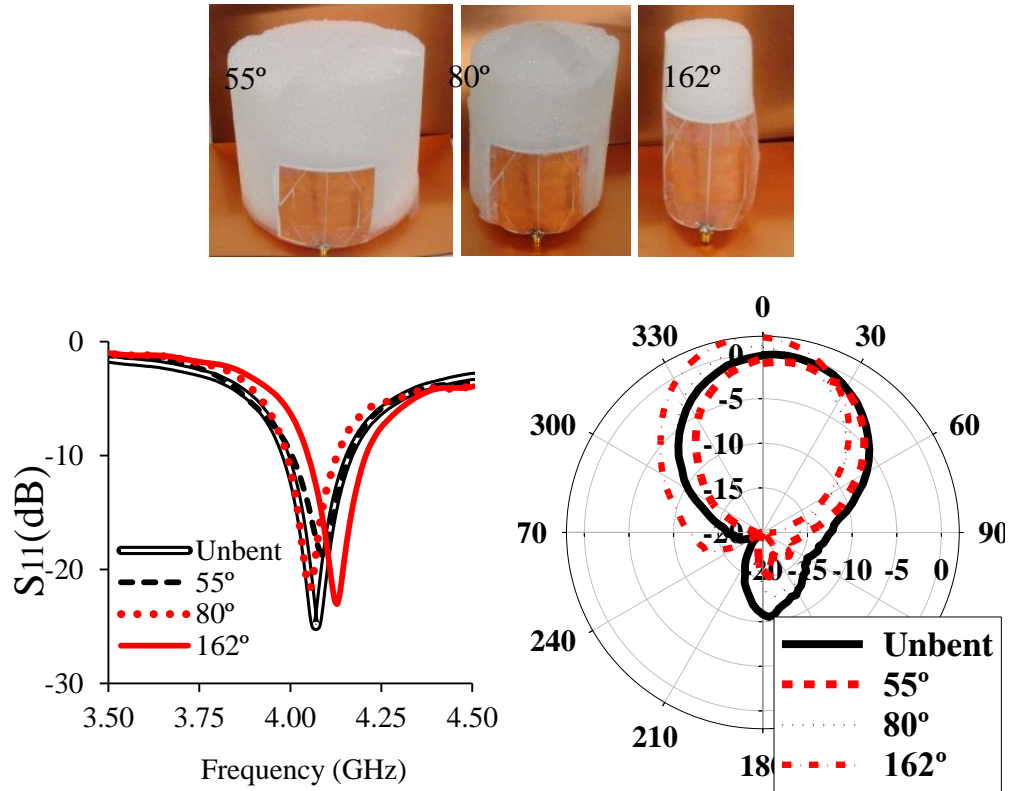
Figure 5.13: Measured S_{11} of the PDMS-ceramic-SGS microstrip patch antenna under different angles of positive radius of curvature (left) and the corresponding H-plane radiation patterns at 4 GHz (right).

A summary of the RT/duroid® 5880, PDMS and PDMS-ceramic antenna characteristics is provided in Table 5.2. The printed radiator area of the PDMS-ceramic antenna was reduced by 46% in comparison the PDMS antenna and the gain was increased. The importance of this miniaturization stems from the fact that a reduction of the copper areal dimension improves flexibility. Another valuable characteristic to highlight about the PDMS-ceramic antenna is that the bond between the LCP and PDMS is stronger when the latter is mixed with ceramic powder. The antenna also has lower mass than antennas fabricated on RT/duroid® 5880 with similar thickness. The antennas built on the conventional substrate (RT/duroid® 5880), PDMS and PDMS/ceramic have masses of ~31, 15 and 18 gms, respectively, while having the same planar size (72 mm x 72 mm) and similar thickness (2.5 mm).

118

Table 5.2: Non-bent antenna comparison.

Material	RT/duroid® 5880	PDMS-SGS	PDMS-ceramic-SGS
Radiator Area (mm^2)	735	660	352
Radiator Area Reduction	---	23%	50%
Mass (gms)	31	15	18
Mass Reduction (gms)	---	51%	42%
Gain (dBi)	5.0	2.4	3
Efficiency (%)	78%	48%	55%
Flexible	NO	YES	YES

5.3.   Flexible BST based Tunable Low Profile Antenna

In this section a flexible low profile dipole antenna using a frequency selective surface (FSS) with interdigital barium strontium titanate (BST) varactor-tuned unit cells is presented (Figure 5.14). The antenna is fed with a microstrip-to-coplanar strip balun and uses two 2.4 mm-thick substrate layers, resulting in a total antenna thickness of ~λ/24 at the operational central frequency of 2.4 GHz. The antenna uses overlapping metallic plates to improve the flexibility of the structure.
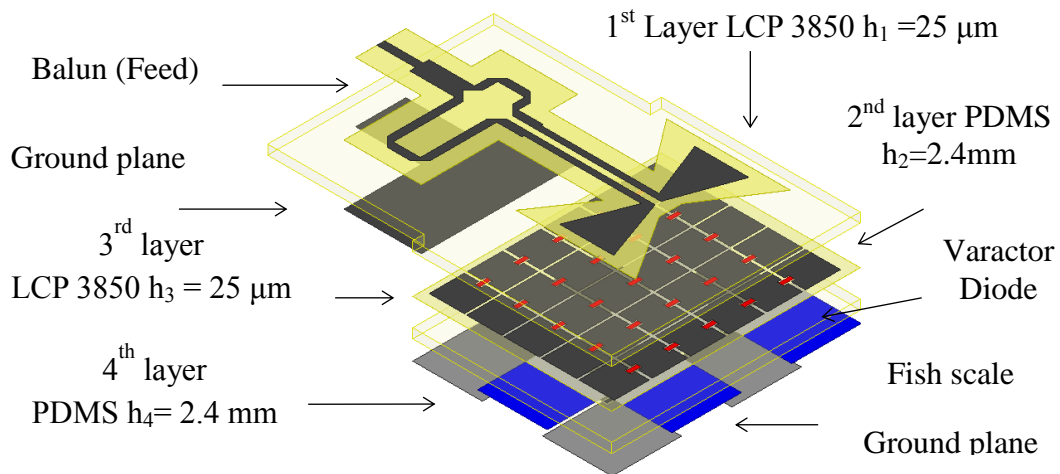
Figure 5.14: Schematic of bowtie dipole antenna illustrating the multi-layer substrate with feed layer, tunable FSS layer, and bowtie dipole.

119

The main contribution of this section is that it proposes increasing the flexibility of a multilayer antenna structure by using overlapping metal plates (fish-scale) which dramatically reduces the rigidity. Typically microwave antennas are made by assembling multiple layers of different materials. Some of these layers are made of metal; generally the backside of the antenna is a metal ground plane and the top side is a metal radiating element. Sandwiched between the metal layers is some kind of non-conducting, insulating material (the substrate). In most cases, the antenna performs better as the thickness of the insulating material increases. When these different layers are bonded together the structure tends to become rigid, even if the metal layers are thin and the insulator itself is a flexible material. Various research publications have demonstrated flexible antennas for wide ranging applications [23]-[35]. However, these approaches achieved flexibility by reducing the thickness of a single substrate layer or by using only one metal layer. None of the publications mentioned above mentioned address the mechanical and electrical challenge to create flexible microwave antennas that can be used with portable biomedical radiometers and be worn comfortably by patients for extended periods of time. This antenna design builds upon prior related work on rigid substrates that used a square patch FSS loaded with varactors [21], [46].

5.3.1. Mechanical and Electrical Considerations

One of the biggest mechanical challenges to address in a multi-material stack structure is how to achieve flexibility. The stiffness of a composite beam is directly proportional to the cube of the thickness and the maximum deformation is experienced by those materials that are farthest from the neutral axis (O). The need to block electromagnetic radiation compels the use of a ground plane far from the bending neutral axis (O) which increases the rigidity of the stack. Three different scenarios are depicted in Figure 5.15; a polymer using only one copper layer

120

(Case I), two copper layers (Case II), and a multi-material stack (Case III). The normalized rigidity was calculated for each case and is shown in Table 5.3. For Case I, the normalized rigidity of a board with polymer height (t_{PDMS}) of 1.25 mm and one copper layer of thickness (t_{Cu}) of 0.25 µm is 1. If the polymer thickness doubles, then rigidity increases by a factor of 4.3. In this case, the neutral axis does not pass through the centroid of the composite material and it lies closer to the copper layer, reducing the deformation of the latter. However, when a flexible material is sandwiched between two metal layers (Case II), the rigidity is increased by over three orders of magnitude (see Table 5.3). The metal layers will experience more plastic deformation than the polymer as they have higher modulus of elasticity and are farther from the neutral axis (Figure 5.15f). For a multi-material stack structure (Case III), the rigidity of the board is increased by factors of 8,300 and 30,000 with respect to case I when t_{PDMS} is 1.27 mm and 2.5 mm, respectively.
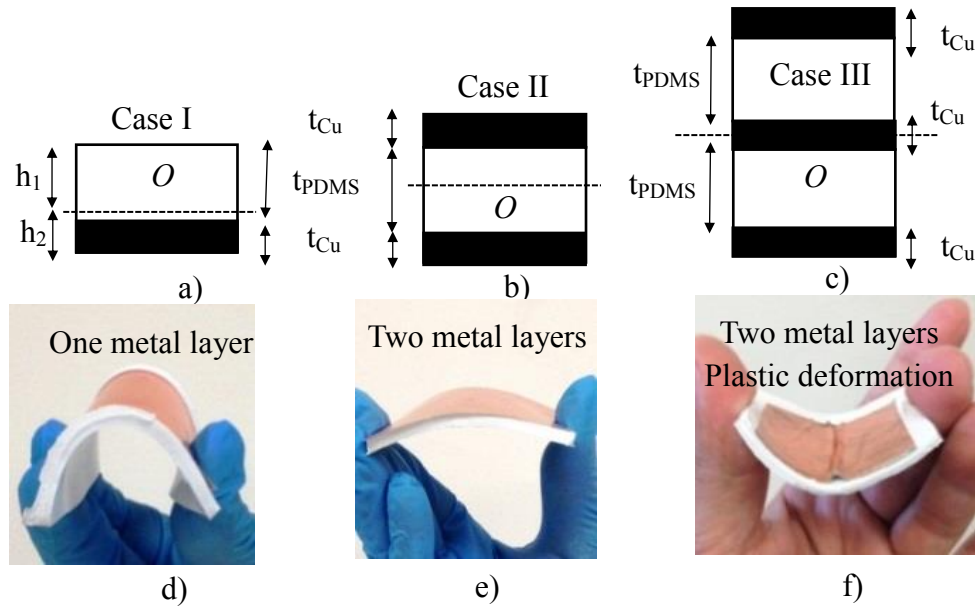
Figure 5.15: (a) Rectangular cross section of PDMS based substrate with one metal layer. (b) Rectangular cross section of PDMS based substrate sandwiched between two metal layers. (c) Rectangular cross section multi-material stack structure. (d) Case I bent forming a negative radius of curvature; (e) Case II bent forming a negative radius of curvature; (f) case II showing plastic deformation of the metal layer.

121

Table 5.3: Normalized flexural rigidity for different scenarios.

Polymer height	Case I One layer of copper	Case II Two layers of copper	Case III Multi-material stack
Rigidity (1.25 mm)	1*	1200	8300
Rigidity (2.5 mm)	4.3	8100	30000

* Less rigid case (normalized values). Calculation details are shown in Appendix E.

Another challenge of this design is reducing the losses caused by the series resistance of the varactor diodes while using a relatively thin substrate. Full wave analysis of the unit cells using Ansoft HFSS predicts that the series resistance of a varactor diode has less impact on the antenna performance as the substrate thickness is increased. However, increasing the substrate thickness also increases the rigidity as explained before. Figure 5.16 shows the effect of the series resistance of the varactor on the magnitude of the reflection coefficient for different substrate thicknesses. As mentioned in chapter 4 the normalized magnitude of the reflection coefficient ($|\Gamma|$) in is usually required to be $> |0.8|$, which corresponds to the minimum value for effective FSS operation. For a 1.27 mm substrate thickness, $|\Gamma|$ is much less than the design criterion and therefore the antenna electrical performance (i.e. gain, efficiency. etc.) will be negatively affected.
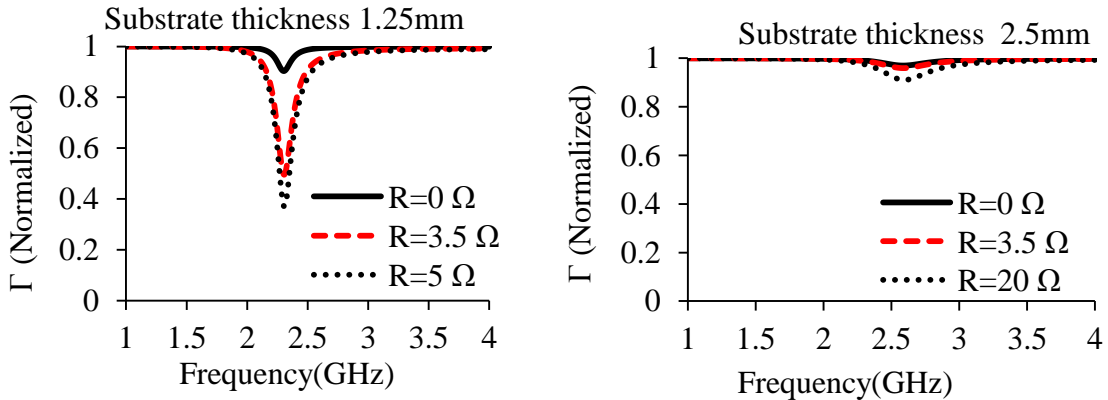
Figure 5.16: Impact of the substrate thickness and varactor losses on the reflection coefficient magnitude of the tunable FSS. Substrate $\tan\delta = 0.002$.

5.3.2. Antenna Design, Fabrication and Results

Prior to implementing the multi-layer antenna design the high frequency electrical properties of the materials were determined using Agilent's 85070D dielectric probe kit. The left side of Figure 5.17 shows the dielectric constant and electric loss tangent for different volume ratios in an extended frequency range from 500 MHz to 3 GHz (previous data on Figure 5.3 were extracted from 500 MHz to 1 GHz). The frequency of operation of the dipole antenna was chosen to be around ~ 2.4 GHz to be consistent with designs discussed in previous chapters and to facilitate in-house fabrication (right side of Figure 5.17)
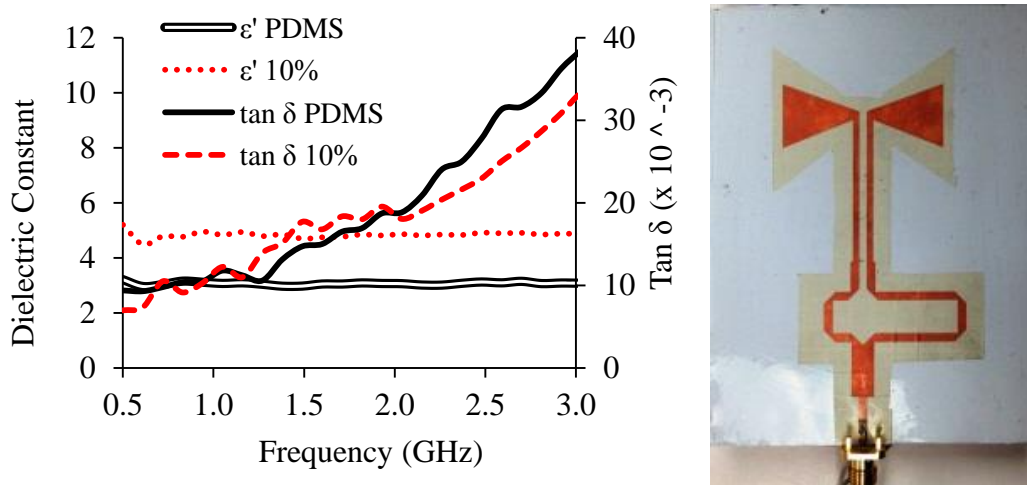
Figure 5.17: Dielectric constant and loss tangent for the PDMS-ceramic samples at different volume ratios (left). Flexible bowtie antenna (right).

The FSS and antenna substrates were cured at ambient temperature over a leveled optical table to maintain a uniform height and to avoid an increment on the Young's modulus of the material [28]. The maximum tolerance of variation allowed for the substrate height was ~ ±0.1 mm to reduce possible significant changes in the frequency response. The fabrication of these flexible antenna substrates as well as the LCP/PDMS bonding process is explained in detail in previous section 5.2 and in [49].

Simulations of the magnitude of the reflection coefficient (Γ) of a unit cell using different substrate losses and two different substrate heights are depicted in Figure 5.18. The results show that increment of the loss tangent of the substrate material reduces the magnitude of reflection coefficient (Γ) and it is particularly worse when the FSS substrate is thinner.
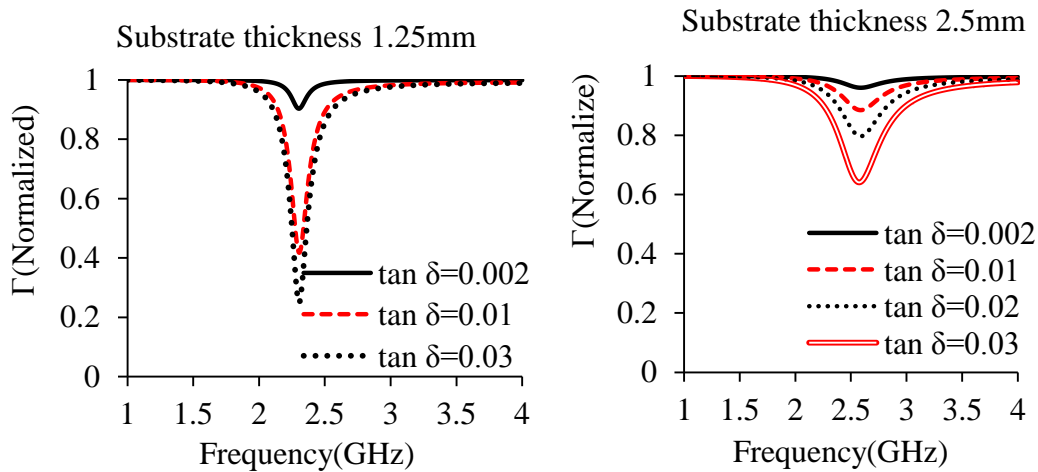
Figure 5.18: Impact of the substrate losses and thickness on the reflection coefficient magnitude of the tunable FSS.

To validate and investigate the impact on the antenna gain due to variations on the FSS height, three different FSS's with different substrate heights were fabricated with SMD chip capacitors (ESR=~0.5 Ω). All three FSS's consisted of 30 unit cells and 25 chip capacitors and they were designed to operate at ~ 2.4 GHz, but built with different substrates thicknesses of 2.0 mm, 2.3 mm and 2.5mm and capacitance values of 1.5 pF, 1 pF and 0.7 pF, respectively. S_{11} of the antenna backed with the three capacitive loaded FSS's are shown in Figure 5.19. The antenna backed with the 2.5 mm height FSS had the highest gain (0.8 dB) and better impedance matching than the others. The gain of the 2.3mm and 2.0 mm height were 0.6 dB and 3.5 dB lower respectively with respect to the 2.5 mm height. These results are in agreement with the units cells simulations in Figure 5.18 and demonstrate the importance of height variations.

To design the tunable FSS, simulations of the phase and the magnitude of the reflection coefficient (Γ) of a unit cell were performed. The capacitance was varied from 1 pF to 1.5 pF to correspond with the approximate measured tunable range of the BST varactor diodes and the FSS's thickness of ~2.4 mm was assumed. The results in Figure 5.20 predict a tunable bandwidth of 400 MHz, from 2.2 GHz to 2.6 GHz, when the criterion of 0 ± 45° phase shift is used. These results take into account an extracted varactor series resistance of 3.5 ohms and a substrate loss tangent of 0.02.
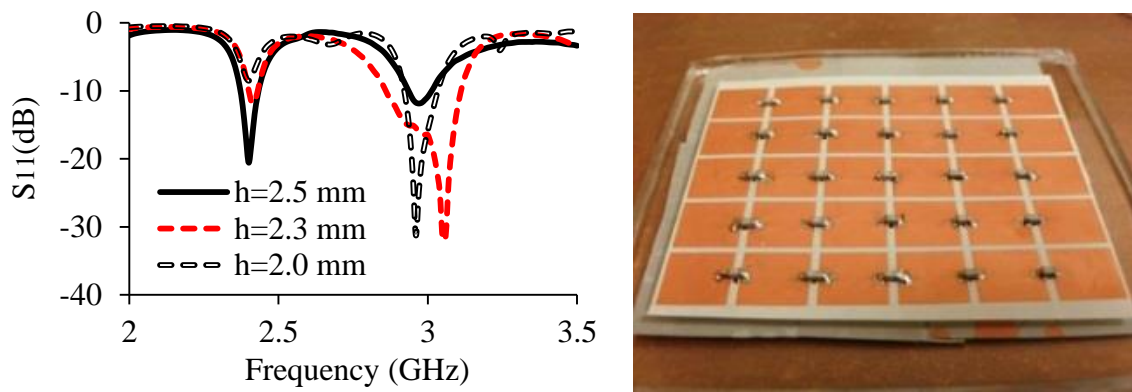
Figure 5.19: Measured S_{11} of the antennas with different heights (left) and capacitive loaded FSS (right).
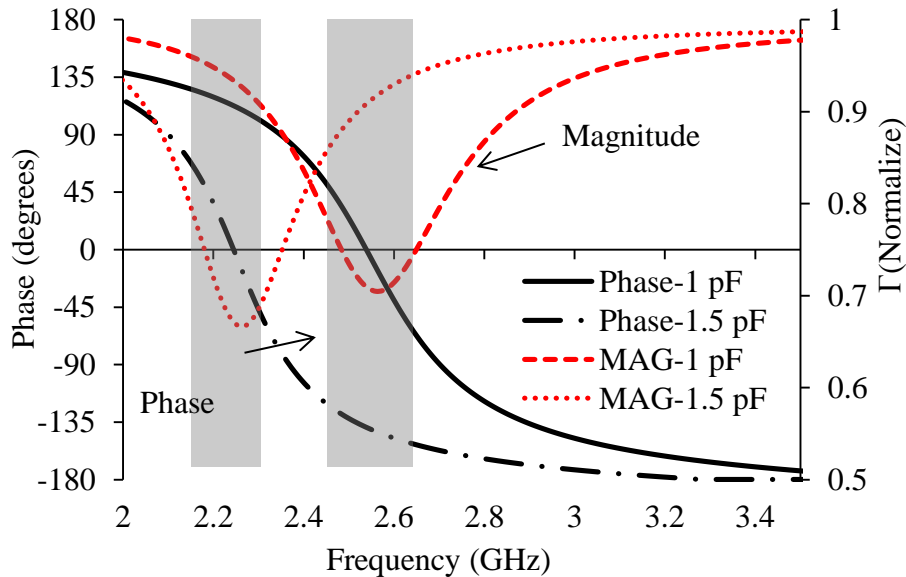
Figure 5.20: Simulated reflection coefficient phase and magnitude of the flexible tunable FSS.

125

The tunable FSS was fabricated using a ~2.4 mm-thick 10% volume blended PDMS ceramic substrate, with a dielectric constant of ~5. The number of devices and unit cell sizes remained the same. The FSS has a planar size of 64 x 65 mm^2, including the bias network. This bias network is distributed in 5 columns, each containing seven BST chips in series, and 6 rows with 1 KΩ resistors in series (See [46] for further details). Similar to [21], the varactors were placed in the direction parallel to the main axis of the bowtie dipole to achieve higher tunability. A 1 KΩ resistor was used at the ends of each row to block RF leakage onto the bias lines. The FSS's ground plane has overlapping metallic plates instead of a continuous metal layer to improve flexibility. The dimensions of the metal plates were ~21x13 mm^2. They were fabricated by keeping the copper on one side of the LCP and patterning the other side using photolithography. The copper was partially removed on the side to be bonded to the flexible substrate to overlap the plates and have an electrical connection and bonded to the PDMS. The overlapping distance among metal plates was ~ 1-2 mm. Then, SU-8 photoresist was spun onto the LCP and patterned into a square grid to increase their flexibility in similar manner as in section 5.2.1.3. The LCP was prepared for bonding using APTES and the squares were cut with a precision scalpel. The LCP squares and PDMS were aligned with respect to each other and pressed together in a vacuum oven at 70°C for 3 minutes to create a permanent bond between the two materials. Figure 5.21 shows the fish scale ground plane and the fabricated tunable FSS.

Comparisons between simulation and measurement data are given in Figure 5.22. For the simulated results, the capacitance range that provided the best correlation to measurement data at each bias point was [1.5, 1] pF. Using the 10 dB return loss criterion, there is a 280 MHz span between the low end of the response with 0 V and the high end of the response using 50 V. Two additional resonances appear at 2.1 GHz and 3 GHz when the input bias is 0 V and they these are

shifted up ~200 MHz when the voltage is 50V as a consequence of TE surface wave propagation. The resonant frequencies of these modes can be calculated using the cavity model analysis explained in detail in [55]; this analysis predicts a TE resonance at ~2.07 GHz and 3.1 GHz for an FSS structure composed of five unit cells with periodicity of 9.9 mm.
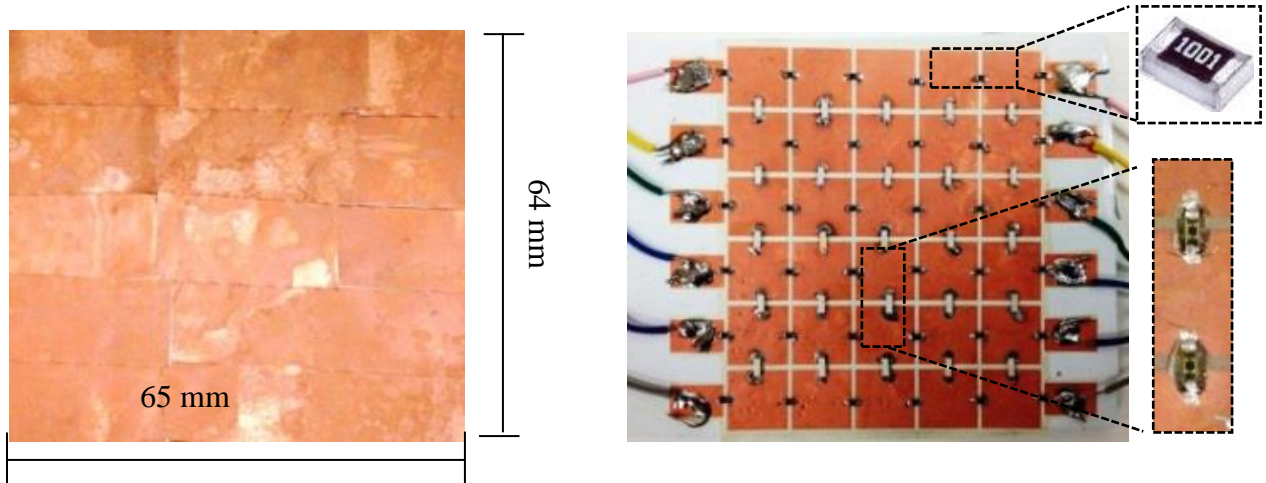
Figure 5.21: (a) Ground plane with overlapping metallic layers and (b) tunable FSS with bias network.
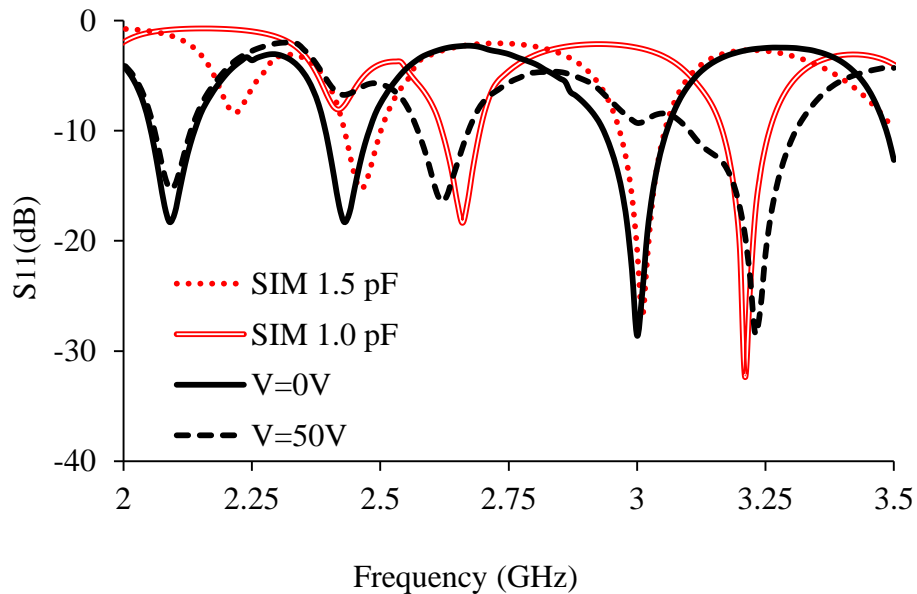
Figure 5.22: Measured and simulated S_{11} when 0 V and ±50 V is applied to all bias ports.
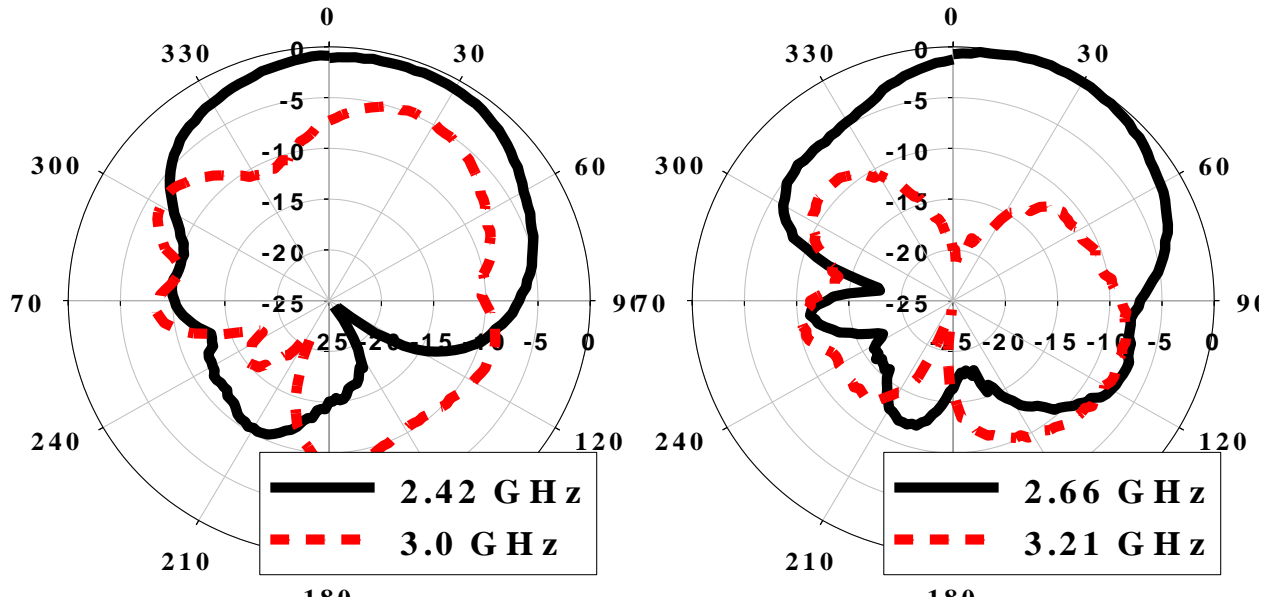
Figure 5.23: Measured E-plane radiation patterns for the antenna with bias voltage of 0 V (left) and ±50 V (right) at different frequencies.

The E-plane radiation patterns of the antenna for different bias voltages are shown in Figure 5.23. The radiation patterns of the antenna with bias voltage of 0 V and ±50 V demonstrate cancellation of back radiation at 2.42 GHz and 2.62 GHz, respectively. The patterns are rotated ~ 25° due to the presence of surface waves. The effects of surface waves are observed in the radiation pattern due to the absence of vias in the HIS. Figure 5.23 also depicts the patterns at 3.0 GHz and 3.2GHz which suggest the presence of leaky waves. The dispersion diagram of the unit cell for different capacitance values was simulated using HFSS. It shows backward/forward leaky waves at ~ 2.8 GHz for a capacitance value of 1.5 pF and at ~ 3 GHz for 1 pF. The leaky waves are supported in the fast wave region indicated to the left side of the light line shown in Figure 5.24.
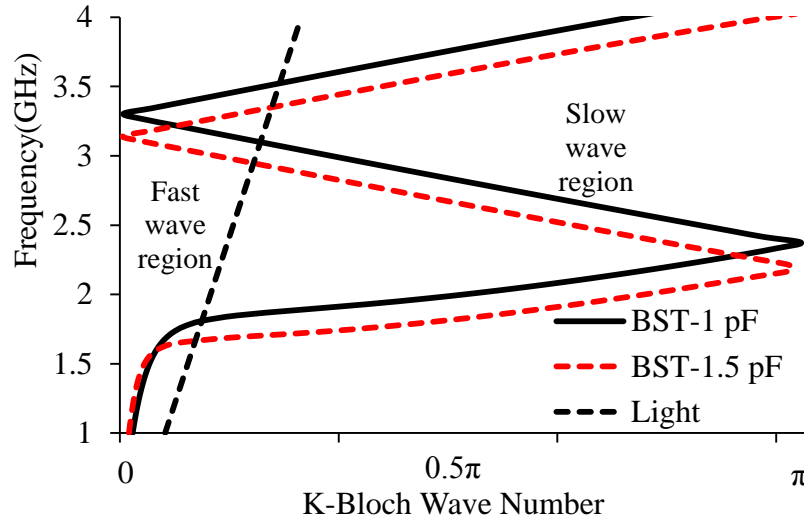
Figure 5.24: Dispersion diagram obtained by cascading 6 unit cells with periodicity of 9.9 mm for C=1 pF and C=1.5 pF.

The gain of the antenna backed with an FSS using a continuous and a fish scale ground plane were compared to each other. The continuous ground plane case was measured by covering the fish scales with adhesive copper tape. The measured gain for the fish scale case was -0.86 dBi at 2.4 GHz for a 0V input bias and for the continuous case was 0.4 dBi. This represents a ~1.3 dB gain reduction with respect to that when using the fish-scale metal layer for a continuous one. The low gain in both cases may be attributed to the material losses and variations on the FSS height. The simulated antenna gain at broadside obtained with Ansoft HFSS using a continuous ground plane is approximately 1.6 dBi at 2.4 GHz; however the 0.04 loss tangent of the SU8-5 bond layer and possible variations of the substrate height were not included in the model to reduce the computational load requirements.
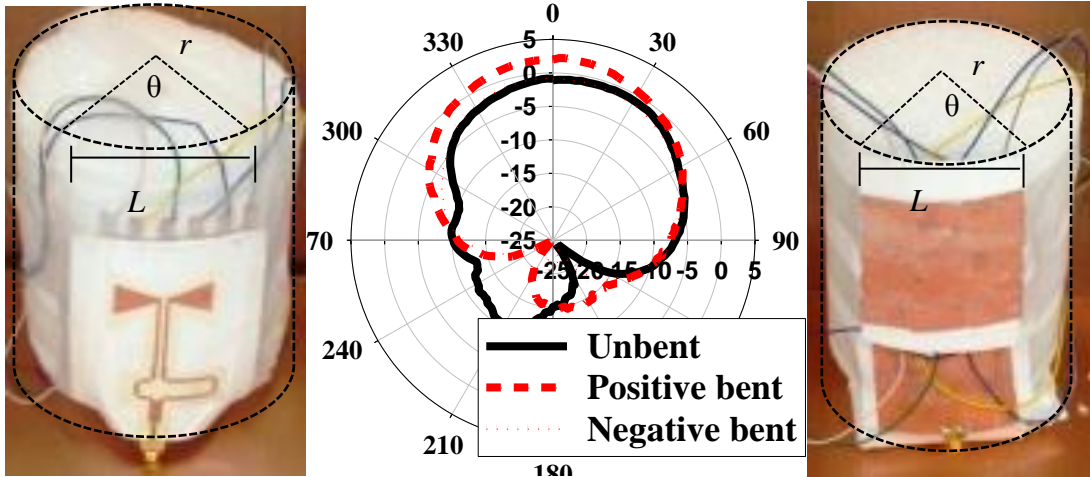
Figure 5.25: Measured E-plane radiation patterns for the antenna with bias voltage of 0 V bent with negative (left) and positive (right) radius of curvatures for θ=77°.
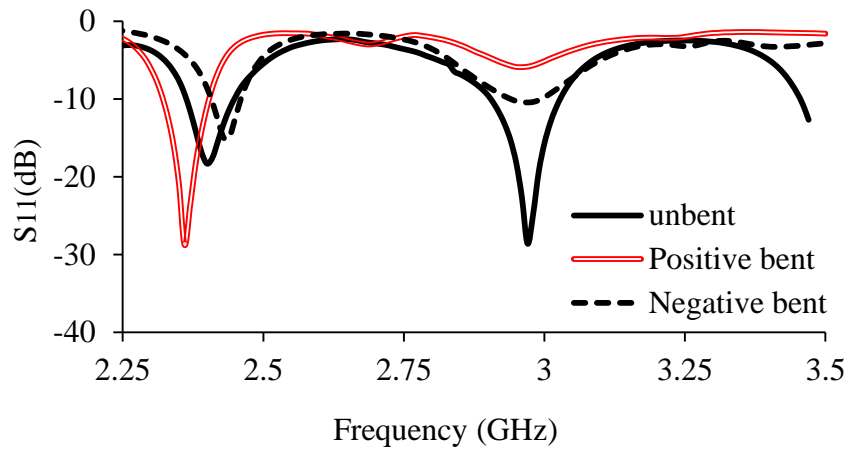
Figure 5.26: Measured S_{11} of the bowtie dipole antenna backed with an FSS unbent, bent with positive radius of curvature and negative radius of curvature for θ=77°.

A styrofoam cylinder of 50 mm radius *r* was used to perform the bending tests. The angle of curvature *θ* was determined using the formula which defines the central angle whose vertex is the center of a circle (*L* = 64mm) (5.1). Figure 5.25 and Figure 5.26 show the radiation pattern and S_{11} data when the antenna is unbent and bent (positive and negative). The results show that when the antenna is bent in positive radius of curvature the frequency shifts up 40 MHz (1.6%) and the gain at 2.36 GHz increases by 3.1 dB for an angle of 77° for V = 0 V with

130

respect the unbent case. This gain increases because of the reduction of back radiation as the ground plane curves toward the front direction of the dipole. For the negative bending case the frequency shifts up 20 MHz (0.86%) and the gain mantains similar values as the unbent antenna (~-0.7dB), but there is less back radiation as consequence of the curvature of the ground plane.

5.4. Conclusion

The development of a flexible PDMS/LCP based antenna has been presented. The use of SU8-5/APTES as an intermediate layer along with the slotted ground structure has been demonstrated to be a promising method to fabricate flexible antennas. By placing cuts in the ground plane the radius of curvature can be increased and the stress produced by bending the copper can be reduced. This approach also opens the possibility of using a defected ground structure (DGS) to enhance the performance of the antenna and improve its flexibility.

The fish-scale ground plane was demonstrated specifically for flexible microwave antennas. The approach represents a significant advance in the combined thickness and flexibility that can be achieved, especially when using relatively thick substrates which are important for optimum antenna performance. Furthermore, the demonstrations presented here using a hybrid manufacturing approach could be transitioned to thin-film microelectronics.

The antennas developed are tunable, robust, and flexible and they have less mass than typically used alternative technologies. The antennas also incorporated a ground plane which minimizes the back lobes. They exhibit an increment on gain when bent in a positive radius of curvature and further reduction of back radiation. All these features are highly desired for antennas in radiometric applications. Despite the antennas have not met yet the efficiency requirements to be integrated with the radiometer, the design and techniques herein presented can be used when high quality thin films and lower loss flexible materials are developed.

131

CHAPTER 6: SUMMARY AND RECOMMENDATIONS FOR FUTURE WORK

6.1.   Summary of New Contributions to the Field

This research has presented an investigation on reconfigurable low profile antennas using high impedance surfaces (HIS). A series of antenna architectures have been designed, built and compared against each other. The antenna designs were based on broadband dipole antennas over tunable frequency selective surfaces (FSS) to extend the usable frequency range. In chapter 3 a comparison of the first generation (Jerusalem Cross) and second generation (Square Patches) of the non-tunable symmetrical antennas showed that the SP-based antenna is better suited for applications where bandwidth was required. Results showed an increase in the fractional bandwidth from 1.4% to 2.68% when a SP-FSS (non-tunable symmetrical HIS) was used as the cell structure. The third generation using discrete capacitors (non-tunable asymmetrical HIS) demonstrated comparable performance between a non-loaded and a capacitively-loaded FSS with a significant reduction in the number of cells and/or cell geometry size. The total antenna area was reduced by 12%. The tunable low profile antennas in chapter 4 (fourth and fifth generations) showed frequency tunability from 2.2 GHz to 2.6 GHz, high from back-to-back radiation and frequency adjustment in response to adverse environmental loading. Finally, the flexible low profile antennas in chapter five demonstrated tunability from 2.42 GHz to 2.66 GHz and 1.3 dB gain drop when using overlapping metallic plates instead of a continuous ground plane. As a result of these findings, reconfigurable low profiles tunable antennas using HIS can potentially be used to realize conformal, self-compensating radiating surfaces towards improvements in radiometric (passive) biomedical sensing applications.

132

The following are original contributions to the antenna field and/or electromagnetics:

- Demonstration that 1-D HIS has simplified bias and similar tunability performance as 2-D HIS when placed over linearly polarized dipoles.

- Development of a methodology to design low profile antennas using tunable HIS

- Development of an approach to select the unit cell geometry, varactor dimensions and specifications, and substrate thickness for a tunable HIS. The approach shows the importance, functionality and impact of these parameters on the size reduction and the performance of a low profile end loaded planar open sleeve dipole (ELPOSD) antenna using an HIS

- Demonstration of how the effects of the coupling between the antenna and HIS, as well as the varactors losses, impact the antenna performance. This dissertation also defines an approach to compensate for these effects

- Implementation of a quasi-static circuit model for a 1-D varactor based tunable cell FSS that allows understanding the current edge effects on tunable unit cells. The model proposed an alternative way to analyze tunable HIS unit cells

- Development of an approach to select materials to design flexible robust antennas. The approach shows how the mechanical and electrical properties of the material affect the performance of flexible antennas and it also shows new methods to achieve flexibility.

These contributions have allowed developing low profile ELPOSD antennas using HISs with one dimensional (1-D) varactor tuning and no vias to ground that could be dynamically tuned in center frequency and impedance match to create broadband or multi-resonance responses in free space or in close proximity to a Human Core Model (HCM) phantom. These antennas can also be dynamically tuned to optimize their radiation patterns. In addition, the use

of thin film ferroelectric Barium Strontium Titanate (BST) varactors in the FSS layer, flexible materials and processes to produce electrically thick flexible substrate enabled an antenna with a smaller size, lower cost, robust and less weight compared to the commercially available options. All these features are highly desirable for antennas to be used for conformal portable radiometric sensing applications.

6.2.   Recommendations for Future Work

Suggestions for future work that will add improvement to the designs presented here are:

- Integrate a 2.4 GHz low profile ELPOSD antenna using a HIS with 1-D varactor tuning into a radiometer to verify performance.

- Develop high quality thin films and lower loss flexible materials to improve the electrical performance of flexible low profile antennas using HIS with 1-D varactors tuning

- Study of alternative unit cell geometries (i.e. hexagon, asymmetric cells, etc.) and defected ground structures (DGS). Measured results of ELPOSD antennas over asymmetric HIS and simulation of unit cells with DGS in Appendix F have demonstrated the viability of this design for dual band antennas

- Develop a flexible low profile ELPOSD antenna using a HIS with 1-D varactor tuning at 700 MHz where the loss tangent of PDMS is at least one order of magnitude lower than the loss tangent at 2.5 GHz

- Develop low profile antennas using alternate substrates such as magnetodielectric substrates. Simulations of unit cells performed by the author using SMMDF$^{®}$ (ε=7, μ=7) from Spectrum Magnetics have demonstrated fractional bandwidth of up to 40% at 300 MHz

- Study the potential extension of using HIS with 1-D varactor tuning in three-dimensional antennas to achieve frequency tunability and miniaturization.

REFERENCES

[1] Q. Bonds.” A Microwave Radiometer for Close Core Body Temperature Monitoring: Design, Development, and Experimentation” PhD dissertation, Dept. Elect. University of South Florida, Tampa, FL, 2011

[2] C. A. Balanis “*Antenna Theory, Analysis and Design*”, 3rd ed., Wiley, New Jersey, 2005, pp. 17–20

[3] S. Baylis, S. Presas, and T. Weller, “Wide Bandwidth Varactor-Tuned Patch Antenna,” *IEEE Electronics Letters*, Vol. 45, Issue 16, pp. 816-818, July 2009.

[4] C.K.Wu and K.L Wong “A broadband Microstrip antenna with directly coupled and gap-coupled parasitic patches,” *Microwave Opt. Technol. Lett.* 22, 348-349, Sept 5 1999.

[5] M Haridim, D. Shukrun, and H. Matzner, “A novel broadband Triple-Layer triangular patch antenna”, *Microwave Opt. Technol. Letters*, Vol. 40 No. 1, 66-71, Jan 5 2004.

[6] D. Sievenpiper, L. Zhang, R. Broas, N. Alexopolous, and E. Yablonovitch, “High-impedance electromagnetic surface with a forbidden frequency band,” *IEEE Trans. Microwave Theory Tech.* vol. 47, pp. 2059-2074, Nov. 1999.

[7] L. Li, B. Li, H.X. Liu, and C.H. Liang, “Locally resonant cavity cell model for electromagnetic band gap structures,” *IEEE. Tans. Antennas Propag*. vol. 54, no. 1, pp. 90-100, Jan. 2006.

[8] F. Yang, and Y. Rahmat-Samii, “Reflection Phase Characterizations of the EBG Ground Plane for Low Profile Wire Antenna Applications,” *IEEE Trans. Antennas Propagat*., vol. 51, no. 10, pp. 2939-2949, Oct. 2003.

[9] N. Engheta and R. W. Ziolkowski, (editors), “*Metamaterials: Physics and Engineering Explorations*”, Wiley-IEEE Press, 414 pages, June 2006.

[10] D. Cure, S. Melais , T. Weller, P. Herzig and . Roeder “2.45 GHz end-loaded dipole backed by a high impedance surface,” *IEEE Antennas Propagation Symposium*, Toronto, Canada, July 2010.

[11] D. Sievenpiper, et al., “Electronic Beam Steering Using a Varactor-Tuned Impedance Surface*,” Proc. IEEE Antennas and Propagation Society Int. Symp.*,vol. 1, Boston, MA, 2001, pp 174-177.

[12] V. C. Sanchez, R. E. Diaz, and W. E. McKinzie, "Broadband Antennas Over Electronically Reconfigurable Artificial Magnetic Conductor Surfaces," *Proceedings of the Antenna Applications Symposium,* Robert Allerton Park, Monticello, IL, Sept. 19-21, 2001.

[13] M. G. Bray and D. H. Werner, "A Broadband Open-Sleeve Dipole Antenna Mounted Above a Tunable EBG AMC Ground Plane," *Proceedings of the 2004 IEEE Antennas and Propagation International Symposium.* Monterey, CA. June 21-26, 2004. Vol. II, pp. 1147 – 1150

[14] F. Costa, A. Monorchio, S. Talarico, and F. M. Valeri, "An active high impedance surface for low profile tunable and steerable antennas," *IEEE Antennas Wireless Propag. Letters*, vol. 7, pp. 676–680, 2008.

[15] P. Bhartia and I. J. Bahl, "Frequency agile microstrip antennas," Microwave Journal, vol. 25, Oct. 1982, p. 67-70.)

[16] J. M. Carrere, R. Staraj, and G. Kossiavas, "Small frequency agile antennas", *Inst. Elect. Eng. Electron. Lett.*, vol. 37, pp.728 -729 2001

[17] A.K. Gautam, B.R. Vishvakarma, "Frequency Agile Microstrip Antenna Symmetrically Loaded With Tunnel Diodes*", Microwave and Optical Technology Letters*, Vol.48,n°9, Sept 2006.

[18] J.A. Zammit and A. Muscat, "Tunable microstrip antenna using switchable patches," *The 2008 Antennas and Propagation Conference (LAPC 2008)*, 233-236, March 17-18, 2008.

[19] S. V. Hum, "Analysis of varactor diode-tuned frequency agile antennas," in *Proc. IEEE Antennas and Propagation (EuCAP*), Barcelona, Spain, Apr. 2010, pp. 1-5.

[20] D. Sievenpiper, J. Schaffner, H.J. Song, R. Loo, and G. Tangonan, "Two-dimensional beam steering reflector using an electrically tunable impedance surface," *IEEE Trans. Antennas Propag*., Vol.51, no. 10, pp.2713-2722, Oct. 2003.

[21] D. Cure, T. Weller and F.A. Miranda "Study of a Low Profile 2.4 GHz Planar Dipole Antenna Using a High Impedance Surface with 1-D Varactor Tuning," Submitted for *IEEE Antennas Propagation Transaction*.

[22] D. Cure, T. Weller and F.A. Miranda "Non-Uniform Bias Enhancement of a Varactor-Tuned FSS used with a Low Profile 2.4 GHz Dipole Antenna," Submitted for IEEE Antennas and propagation Society Int. Symp, Chicago, IL, USA, July 2012.

[23] A. Tronquo, H. Rogier, and C. Hertleer, "Robust planar textile antenna for wireless body LANs operating in 2.45GHZ ISM band," *Electronics Letter*, vol. 42, no.3, pp. 142-143, February 2006.

[24] X. Zhang, A. Zhao, and J. Wang, "Research on the characteristics of flexible antennas for general applications," *in Microw. and Millimeter Wave Technol. Int. Conf.*, Apr. 21–24, 2008, vol. 4, pp. 1814–1817

[25] D.E. Anagnostou, A.A. Gheethan, A.K. Amert, and K.W. Whites, A direct-write printed antenna on paper-based organic substrate for flexible displays and WLAN applications, *IEEE J Display Technol* 6 (2010), 558–564.

[26] A. Tronquo, H. Rogier, and C. Hertleer, "Robust planar textile antenna for wireless body LANs operating in 2.45GHZ ISM band," *Electronics Letter*, vol. 42, no.3, pp. 142-143, February 2006.

[27] S.L. Peterson, A. McDonald, P.L Gourley, D.Y. Sasaki, "Poly(dimethylsiloxane) thin films as biocompatible coatings for microfluidic devices: Cell culture and flow studies with glial cells Biomed," *Mater. Res*. A 2005, 72A, 10–18.

[28] C.-P. Lin, C.-H. Chang, Y.T. Cheng, C.F. Jou, "Development of a flexible SU-8/PDMS-based antenna", *IEEE Antennas Wirel. Propag. Lett.*, 10 1108–1111 (2011).

[29] C. Cibin, P. Leuchtmann, and M. Gimersky, "A flexible wearable antenna," 2004 *IEEE Antenna and Propagation Society International Symposium*, vol.4, pp. 3589-3592, August 2004.

[30] Courreges, S.; Yuan Li; Zhiyong Zhao; Kwang Choi; Hunt, A.; Horst, S.; Cressler, J.D.; *Papapolymerou, J.; , "A Ka-Band Electronically Tunable Ferroelectric Filter," Microwave and Wireless Components Letters, IEEE* , vol.19, no.6, pp.356-358, June 2009

[31] Furuya, N. GUAN, and K. Himeno, "Characteristics of a deformed antenna made of flexible printed circuit," *IEICE Transactions on Communications*, vol. E90-B, pp. 2225-2229, April 2007.

[32] D. Depret, H. Rogier, K. Dhaenens, and J. Vanfleteren, "Flexible substrate low-cost construction of a coplanar-waveguide aperture coupled microstrip patch antenna," *Microwave and Optical Technology Letters*, vol. 49, pp. 1071-1074, May 2007

[33] X. Zhang, A. Zhao, and J. Wang, "Research on the characteristics of flexible antennas for general applications," in *Microw. and Millimeter Wave Technol. Int. Conf.*, Apr. 21–24, 2008, vol. 4, pp. 1814–1817

[34] J. M. Gere, S. P. Timoshenko "Mechanics of Materials", 4th ed, PWS Pub. Co, MA, 1998, pp. 314–317.

[35] S. Koulouridis, G. Kiziltas, Y. Zhou, J L. Hansford, and D. J. Volakis, "Polymer–Ceramic Composites for Microwave Applications: Fabrication and Performance Assessment," *IEEE Trans. Microw. Theory Tech.*, 54 4202–4208 (2006).

[36] C. Morales, "Magneto-Dielectric Polymer Nanocomposite Engineered Substrate for RF and Microwave Antennas" Ph.D. Thesis, Dept. Elect. University of South Florida, Tampa, FL, 2011.

[37] F. Costa, A. Monorchio, and G. P. Vastante, "Tunable High-Impedance Surface With a Reduced Number of Varactors," *IEEE Antennas and Wireless Propagation Letters*, vol. 10, pp. 11–13, 2011.

[38] S. Hage-Ali, N. Tiercelin, P. Coquet, R. Sauleau, V. Preobrazhensky & P. Pernod, "Millimeter-wave patch array on ultra-flexible micromachined polydimethylsiloxane (PDMS) substrate", *IEEE APS/URSI International Symposium*, pp. 1-4, June 2009.

[39] D. Armani, C. Liu N. Aluru, "Re-configurable fluid circuits by PDMS elastomer micromachining," *Micro Electro Mechanical Systems, 1999. MEMS '99.* Twelfth IEEE International Conference on , vol., no., pp.222-227, 17-21 Jan 1999

[40] M.Couty, S. Nazeer, C.Jelita, E. Martincic, M. Woytasik, J.C Ginefri, L. Darrasse, M. Tatoulian, and E. Dufour-Gergam, "Ultra-flexible micro-antennas on PDMS substrate for MRI applications", *Symposium on Design, Test, Integration and Packaging of MEMS/MOEMS (DTIP),* 2012, pp. 126- 131, April 2012.

[41] S. Talaei, O, Frey, P.D. van der Wal, N.F. de Rooij and M. Koudelka-Hep, "Hybrid microfluidic cartridge formed by irreversible bonding of SU-8 and PDMS for multi-layer flow applications", *Procedia Chemistry 1*, 381–384 (2009).

[42] N. Tiercelin, P. Coquet, R. Sauleau, V. Senez, and H. Fujita, "PolyDiMethylSiloxane membranes for millimeter-wave planar ultra flexible antennas," *J. Micromech. Microeng.*, vol. 16, pp. 2389–2395, 2006

[43] D. Cure, T. Weller and F.A. Miranda "A comparison between Jerusalem Cross and Square Patch Frequency Selective Surfaces for low profile antenna applications," in *Proc. IEEE Int. Conf. Electromagnetics in Advanced Applications (ICEAA)*, Torino, Italy, Sep. 2011, pp. 1019 – 1022.

[44] S. Melais, D. Cure and T. Weller, "A Quasi-Yagi Antenna Backed by a Jerusalem Cross Frequency Selective Surface*," International Journal of Microwave Science and Technology*, vol. 2013, Article ID 354789, 8 pages, 2013. doi:10.1155/2013/354789

[45] D. Cure, T. Weller, F.A. Miranda and P. Herzig "One dimensional capactive loading for low profile antenna applications," in *Proc. IEEE Antennas and Propagation Society Int. Symp*, Spokane,WA, USA, July 2011, pp 2258 - 2261.

[46] D. Cure, T.Price, T. Weller, F.A. Miranda and F. Van keuls "Low Profile Tunable Antenna Using Barium Strontium Titanate Varactors ," Under review at IEEE *Antennas Propagation Transaction*.

[47] D. Cure, T. Weller, T.Price and F.A. Miranda "Low Profile Tunable Dipole Antenna Using BST Varactors for Biomedical Applications," Accepted for publication for *IEEE Antennas and propagation Society Int. Symp*, Orlando, FL, USA, July 2013.

[48] D. Cure, M.F. Cordoba, T. Weller and F.A. Miranda "Study of a Flexible Low Profile Tunable Dipole Antenna Using Barium Strontium Titanate Varactors", under review at *IEEE Antennas Propagation letters*.

[49] D. Cure, A. Dey, E. Rojas-Nastrucci, T. Weller, N. Crane and F.A. Miranda "Development of a Flexible Electrically-Thick PDMS/LCP Microstrip Antenna", under review at for *IEEE Antennas Propagation Transaction*.

[50] S.S Gevorgian, T. Martinsson, P.L.J Linner, and E.L Kollberg, "CAD models for multilayered substrate interdigital capacitors," *Microwave Theory and Techniques, IEEE Transactions on* , vol.44, no.6, pp.896-904, Jun 1996.

[51] F. Yang, Y. Rahmat-Samii "Electromagnetic band gap (EBG) structures in Antenna Engineering" The Cambridge RF and Microwave Engineering, 2008, pp. 14–58.

[52] D. Sievenpiper, "High-impedance electromagnetic surfaces," Ph.D. dissertation, Dept. Elect. Eng., Univ. California at Los Angeles, Los Angeles, CA, 1999.

[53] D. M. Pozar, " *Microwave Engineering*", Addison-Wesley, 2004, pp. 49–90.

[54] Kraus, J.D. and Marhefka, R.J. *Antennas for All Applications*, 3rd edition of Antennas. New York, McGraw-Hill, 2002.

[55] F. Costa, O. Luukkonen, C.R. Simovski, A. Monorchio, P. de Maagt and S.A. Tetryakov, "TE Surface Wave Resonances on High-Impedance Surface Based Antennas: Analysis and Modeling," *IEEE Trans. Antennas Propagat.*, vol. 59, no. 10, pp. 3588-3596, Oct. 2011.

[56] D.M Pozar and D.H Schaubert, Microstrip antennas, Wiley, New York, 1995.

[57] K.L Wong, "Compact and Broadband Microstrip Antennas", Wiley, New York, 2002.

[58] F. Yang, X. X. Zhang, X. N. Ye, and R. Samii, "Wide-band E-shaped patch antennas for wireless communications", *Antennas and Propagation, IEEE Transactions on* Volume 49, Issue 7, July 2001 Page(s):1094 – 1100

[59] K.L. Wong, and W.H. Hsu, "A broadband rectangular patch antenna with a pair of wide slits", *Antennas and Propagation, IEEE Transactions on* Volume 49, Issue 9, Sept 2001 Page(s): 1344- 1347.

[60] Lin Peng, Cheng-li Ruan, and Yun Zhang, "A Novel Compact Broadband Microstrip Antenna" *Antennas and Propagation, IEEE Transactions on* Volume 49, Issue 7, July 2001 Page(s):1094 – 1100

[61] Werner D.H and Spence T.G "A Novel Miniature Broadband/Multiband Antenna Based on an End-Loaded Planar Open-Sleeve Dipole" *IEEE Trans. Antennas Propag.*, vol. 54, no. 12, pp.3014–3020, Dec. 2006

[62] S. Melais, "Design and optimization of broadband planar baluns and dipole antennas" M.S. Thesis, Dept. Elect. University of South Florida, Tampa, FL, 2005.

[63] Y.Qian and T.Itoh, "A broadband uniplanar microstrip-to-CPS transition," *Asia-Pacific Microwave Conf. Dig.,* pp. 609-612, Dec. 1997.

[64] H.E. King and J. L.Wong, "An experimental study of a balun-fed open-sleeve dipole in front of a metallic reflector," *IEEE Trans. Antennas Propag.*, vol. 20, pp. 201–204, Mar. 1972

[65] L.Akhoondzadeh-Asl, D J. Kern, P S. Hall,D. H. Werner "Wideband Dipoles on Electromagnetic Bandgap Ground Planes" *IEEE Trans. Antennas Propag.,* vol. 55, no. 9, pp.2426–2434, Sep 2007.

[66] M. Hosseini and M. Hakkak, "Characteristic estimation for Jerusalem Cross based artificial magnetic conductors," *IEEE Antennas and Wireless Propag. Letters*, Vol. 7, 2008.

[67] C.R. Simovski, P. de Maagt, S.A. Tetryakov, M. Paquay, and A. A. Sochava, "Angular stabilization of resonant frequency of artificial magnetic conductors for TE-incidence," *Electron. Lett.*, vol.40, no. 2, pp. 92-93, 2004

[68] Q. Bonds, T. Weller, B. Roeder and P. Herzig, "A tunable Cavity Backed Slot Antenna (CBSA) for close proximity biomedical sensing applications," in *IEEE Microwaves, Communications, Antennas and Electronics Systems*, 2009

[69] Q. Bonds, T. Weller, B. Roeder and P. Herzig, "A Total Power Radiometer (TPR) and Measurement Test Bed for Non Contact Biomedical Sensing Applications", *IEEE Wireless and Microwave Technology Conference (WAMICONN),*Clearwater, Florida 2009

[70] R. Pethig "Dielectric Properties of Biological Materials: Biophysical and Medical Applications," *IEEE Trans. Elect. Insulation*, Vol. EI-19, No. 5, October 1984.

[71] H.P Schwan "Electrical Properties of Tissue and Cell Suspensions: Mechanisms and Models," in *The 16th Annual International Conference of the IEEE Engineering Advances: New Opportunities for Biomedical Engineers*. 1994. Baltimore, MD, USA: IEEE.

[72] J.L Santos, D. Garcia and J.A Eiras "Dielectric Characterization of Materials at Microwave Frequency Range". *Materials Research*, 2002. 6(1): p. 97-101.

[73] C. Gabriel and S. Gabriel "Compilation of the Dielectric Properties of Body Tissues at RF and Microwave Frequencies", Brooks AFB report number AL/OE-TR-1996-0037.

[74] C.R. Simovski, P. de Maagt, S.A. Tetryakov, M. Paquay, and A. A. Sochava, "Angular stabilisation of resonant frequency of artificial magnetic conductors for TE-incidence," *Electron. Lett.,* vol.40, no. 2, pp. 92-93, Jan. 2004

[75] S. V. Hum, M. Okoniewski, and R. J. Davies, "Modeling and design of electronically tunable reflectarrays," *IEEE Trans. Antennas Propagat.,* vol. 55, no. 8, pp. 2200–2210, August 2007.

[76] J. Perruisseau-Carrier, "Dual-Polarized and Polarization-Flexible Reflective Cells with Dynamic Phase Control," *IEEE Trans. Antennas Propagat.,* vol. 58, no. 5, 2010.

[77] S. V. Hum, M. Okoniewski, and R. J. Davies, "Realizing an electronically tunable reflectarray using varactor diode-tuned elements," *IEEE Microw. Wireless Compon. Lett.,* vol. 15, no. 6, pp. 422-424, June 2005.

[78] C. Caloz, T. Itoh "Electromagnetic Metamaterials: Transmission Line Theory and Microwave Applications: The Engineering Approach" Wiley, Hoboken, NJ, USA, 2005, pp. 59–130.

[79] A. J. Baden, "*Microwaves: An Introduction to Microwave Theory and Techniques*", Pergamon Press, 1990, pp. 35–56.

[80] T. Price and T. Weller "Comparison of barium strontium titanate varactors on magnesium oxide and alumina substrates," in *Wireless and Microwave Technology Conference (WAMICON),* Clearwater Beach, FL, USA, April 2011.

[81] B. C. Wadell, *Transmission Line Design Handbook*. Norwood, MA: Artech Print, 1991, pp. 418–419.

[82] I. Bahl, *Lumped Elements for RF and Microwave Circuits*. Norwood, MA: Artech House, 2003, pp. 176–177.

[83] S. Best, and D. Hanna, "Design of a broadband dipole in close proximity to an EBG ground plane," IEEE Antennas and Propagation Magazine, vol. 50, no. 6,Dec. 2008, pp. 52–64

[84] Q. Bonds, J. Gerig, T. Weller, and B. Roeder, "Towards Core Body Temperature Measurement via Close Proximity Radiometric Sensing," *IEEE Sensors Journal, Special Issue on Non-Invasive Physiological Monitoring*, vol. 12, no. 3, pp. 519–526, March 12. 2012

[85] J. Modelsky, Y. Yashchyshyn, "Microwave ferroelectric antenna arrays," *Microwave and Optoelectronics Conference, 2001. IMOC 2001.Proceedings of the 2001 SBMO/IEEE MTT-S International* , vol.2, no., pp. 39- 42 vol.2, 2001

[86] W, Gautier, A. Stehle, C. Siegel, B. Schoenlinner, V. Ziegler, U. Prechtel, W. Menzel, "Hybrid Integrated RF-MEMS Phased Array Antenna at 10GHz," *Microwave Conference, 2008. EuMC 2008. 38th European* , vol., no., pp.139-142, 27-31 Oct. 2008

[87] H. A. Wheeler, "Transmission Line Properties of Parallel Strips Separated by a Dielectric Sheet," *IEEE Transactions on Microwave Theory and Techniques*, MTT-13, 1965, pp. 172-185.

[88] Y.-K. Yoon, M. G. Allen, and A. T. Hunt, "Tunable ferroelectric capacitor with low-loss electrodes fabricated using reverse side exposure," *Proc. 53rd Electron. Compon. Technol. Conf.*, 2003, pp. 1534–1540.

[89] J. Nath , D. Ghosh , J. Maria , M. Steer , A. Kingon and G. Stauf "Microwave properties of BST thin film interdigital capacitors on low cost alumina substrates", *Proc. 34th Eur. Microw. Conf.*, pp.1497 2004

[90] J. Zhang, H. Zhang, K. J. Chen, S. G. Lu; Z. Xu, "Microwave Performance Dependence of BST Thin Film Planar Interdigitated Varactors on Different substrates," *Nano/Micro Engineered and Molecular Systems, 2007. NEMS '07. 2nd IEEE International Conference on* , vol., no., pp.678-682, 16-19 Jan. 2007.

[91] "IEEE Standard Test Procedures for Antennas*," ANSI/IEEE Std 149-1979*, 1979.

[92] N. McN. Alford, J. Breeze, X. Wang, S. J. Penn, S. Dalla, S. J. Webb, N. Ljepojevic and X. Aupi. "Dielectric loss of oxide single crystals and polycrystalline analogues from 10 to 320 K", *Journal of the European Ceramic Society 21* (2001) pp. 2605-2611.

[93] X. Aupi, J. Breeze, N. Ljepojevic, L.J. Dunne, N. Malde, A. Axelsson, N. Mc. Alford, "Microwave dielectric loss in oxides: Theory and experiment," *Journal of Applied Physics*, vol.95, no.5, pp.2639-2645, Mar 2004

[94] A Volkov, V Pavelyev, O Moiseev, V Eropolov, B Volodkin and K Tukmakov, "Thin copper film for plasma etching of quartz," *Optical Memory and Neural Networks (Information Optics)*, 18(1):40-43 (2009).

[95] Z. Zhang, "The fabrication of polymer microfluidic devices using a solid-to-solid interfacial polyaddition," *Polymer.*, vol. 50(23), pp5358-5361, Nov. 2009

[96] H. Boudaghi, M. Azarmanesh, M. Mehranpour, "A Frequency-Reconfigurable Monopole Antenna Using Switchable Slotted Ground Structure," *Antennas and Wireless Propagation Letters,* IEEE , vol.11, no., pp.655-658, 2012

[97] Chen, Z, Ban, Y-L, Chen, J-H, Li, JL-W and Wu, Y-J. 2012. Bandwidth enhancement of LTE/WWAN printed mobile phone antenna using slotted ground structure. *Prog. Electromagn.* Res., 129: 469–483.

[98] K. L. Wong, *Compact and Broadband Microstrip Antennas*. New York: John Wiley & Sons, Inc., 2002, pp. 79–85.

[99] P.H. Pathak, R.G. Kouyoumjian, "An analysis of the radiation from apertures in curved surfaces by the geometrical theory of diffraction," *Proceedings of the IEEE* , vol.62, no.11, pp. 1438- 1447, Nov. 1974.

[100] Zhenhai, S. and M. Fujise, "Bandpass filter design based on LTCC and DGS," Asia Pacific Microwave Conf. Proc. APMC, Vol. 1, 2-3, 2005

[101] Choi, H.-J., et al., "Doherty amplifier using load modulation and phase compensation DGS microstrip line," 36th European Microwave Conf., 352-355, 2006.

[102] Hosseini, S. A., Z. Atlasbaf, and K. Forooraghi, "Two new loaded compact palnar ultra-wideband antennas using defected ground structures," Progress In Electromagnetics Research B, Vol. 2, 165-176, 2008

[103] Zainud-Deen, S. H., et al., "Microstrip antenna with defected ground plane structure as a sensor for landmines detection," Progress In Electromagnetics Research B, Vol. 4, 27-39, 2008.

APPENDICES

Appendix A: Quasi-Static Circuit Model for the Square Patch

This appendix shows the derivation of the close-form equations for square patch geometry.
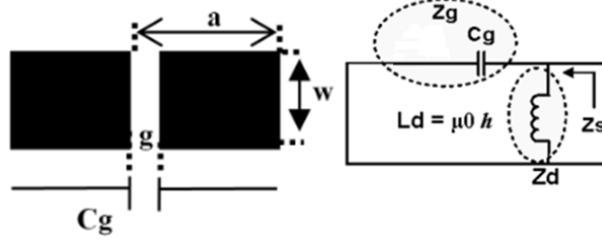
Figure A.1: Equivalent circuit for the self-resonant grid (left) and series combination of the self-resonant grid with the dielectric slab impedance (right) for a SP-FSS unit cell.

$$Z_g = \frac{1}{j\omega C_g} \tag{A.1}$$

$$Z_d = j\omega L_d \tag{A.2}$$

$$Z_s(\omega) = Z_g \parallel Z_d \tag{A.3}$$

$$Z_s(\omega) = \frac{j\omega L_d}{1 - \omega^2 C_g L_d} \tag{A.4}$$

By equating denominator to zero we can find:

$$\omega_r = \frac{1}{\sqrt{C_g L_d}} \tag{A.5}$$

The following equation can be used to obtain the reflection coefficient (Γ) of the plane wave impinging SP-based AMC

$$\Gamma(\omega) = \left[\frac{Z_s(\omega) - \eta_0}{Z_s(\omega) + \eta_0} \right] \tag{A.6}$$

146

Appendix A (Continued)

From studies and results it can be deduced the phase reflection diagram, which is $\Gamma(\omega)$, is nearly lineal around the resonance. Therefore, we can expand $\Gamma(\omega)$, using Taylor series, just taking into account the first two terms which are linear

$$\Gamma(\omega)|_{around\ \omega_r} = \Gamma(\omega)|_{\omega_r} + (\omega - \omega_r)\frac{d\Gamma(\omega)}{d\omega}\bigg|_{\omega_r} \qquad (A.7)$$

where the first term is always zero for an AMC.

$$\Gamma(\omega)|_{around\ \omega_r} = (\omega - \omega_r)\frac{d\Gamma(\omega)}{d\omega}\bigg|_{\omega_r} \qquad (A.8)$$

Therefore using the following equation can be used to extract the bandwidth (BW)

$$BW = \frac{\omega_2 - \omega_1}{\omega_r} \qquad (A.9)$$

Formula derivation:

$$\Gamma(\omega) = \left[\frac{Z_s(\omega) - \eta_0}{Z_s(\omega) + \eta_0}\right] \qquad (A.10)$$

$$\Gamma(\omega) = \left[\frac{\frac{j\omega L_d}{1 - \omega^2 C_g L_d} - \eta_0}{\frac{j\omega L_d}{1 - \omega^2 C_g L_d} + \eta_0}\right] \qquad (A.11)$$

$$\Gamma(\omega) = \left[\frac{j\omega L_d - \eta_0\left(1 - \omega^2 C_g L_d\right)}{j\omega L_d + \eta_0\left(1 - \omega^2 C_g L_d\right)}\right] \qquad (A.12)$$

147

Appendix A (Continued)

Multiplying by its complex conjugate in the numerator and denominator

$$\Gamma(\omega) = \left[\left(\frac{j\omega L_d - \eta_0(1 - \omega^2 C_g L_d)}{j\omega L_d + \eta_0(1 - \omega^2 C_g L_d)} \right) \left(\frac{j\omega L_d - \eta_0(1 - \omega^2 C_g L_d)}{j\omega L_d - \eta_0(1 - \omega^2 C_g L_d)} \right) \right] \tag{A.13}$$

$$\Gamma(\omega) = \left[\left\{ \frac{\left[\eta_0^2 (1 - \omega^2 C_g L_d)^2 - (\omega L_d)^2 - 2\eta_0 j\omega L_d (1 - \omega^2 C_g L_d) \right]}{(j\omega L_d)^2 - \left(\eta_0 (1 - \omega^2 C_g L_d) \right)^2} \right\} \right] \tag{A.14}$$

The argument of a complex number $x + jy$ is $\tan^{-1}\left(\frac{y}{x} \right)$

$$\Gamma(\omega) = \tan^{-1}\left(\frac{2\eta_0 \omega L_d (1 - \omega^2 C_g L_d)}{\eta_0^2 (1 - \omega^2 C_g L_d)^2 - (\omega L_d)^2} \right) \tag{A.15}$$

To find $\Gamma(\omega)|_{around\ \omega_r}$ we need use the formula derived before

$$\Gamma(\omega)|_{around\ \omega_r} = (\omega - \omega_r) \frac{d\Gamma(\omega)}{d\omega} \bigg|_{\omega_r} \tag{A.16}$$

The derivative of the inverse tangent is

$$\frac{d(\tan^{-1}x)}{d\omega} = \frac{1}{1 + x^2} \frac{dx}{d\omega} \tag{A.17}$$

$$\Gamma(\omega)|_{around\ \omega_r} = (\omega - \omega_r)(4\eta_0 C_g) \tag{A.18}$$

Appendix A (Continued)

If $\pm 45^0$ criterion is used then the bandwidth is

$$-\frac{\pi}{4} = (\omega_1 - \omega_r)(4\eta_0 C_g) \tag{A.19}$$

$$\omega_1 = \omega_r - \frac{\pi}{16\eta_0 C_g} \tag{A.20}$$

$$\frac{\pi}{4} = (\omega_2 - \omega_r)(4\eta_0 C_g) \tag{A.21}$$

$$\omega_2 = \omega_r + \frac{\pi}{16\eta_0 C_g} \tag{A.22}$$

$$BW = \frac{\omega_2 - \omega_1}{\omega_r} \tag{A.23}$$

$$BW = \frac{\omega_r + \frac{\pi}{16\eta_0 C_g} - \omega_r - \frac{\pi}{16\eta_0 C_g}}{\frac{1}{\sqrt{C_g L_d}}} \tag{A.24}$$

$$BW = \frac{\pi}{8\eta_0}\sqrt{\frac{L_d}{C_g}} \tag{A.25}$$

If $\pm 90^0$ criterion is used then the bandwidth is given by

$$BW = \frac{\pi}{4\eta_0}\sqrt{\frac{L_d}{C_g}} \tag{A.26}$$

If a superstrate is taken into account then the bandwidth is given by

$$BW = \frac{\pi\sqrt{\varepsilon_r}}{4\eta_0}\sqrt{\frac{L_d}{C_g}} \tag{A.27}$$

149

Appendix B: Quasi-Static Circuit Model for the Jerusalem Cross

This appendix shows the derivation of the close-form equations for Jerusalem cross geometry.
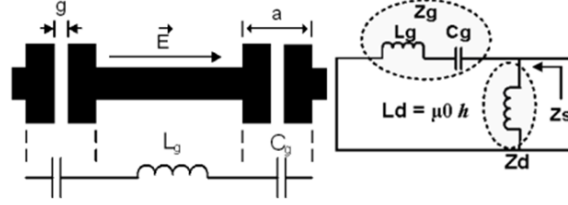

Figure B.1: Equivalent circuit for the self-resonant grid (left) and series combination of the self-resonant grid with the dielectric slab impedance (right) for a JC-FSS unit cell.

$$Z_g = j\omega L_g + \frac{1}{j\omega C_g} \tag{B.1}$$

$$Z_d = j\omega L_d \tag{B.2}$$

$$Z_s(\omega) = Z_g \parallel Z_d \tag{B.3}$$

$$Z_s(\omega) = j\omega L_d \frac{1 - \omega^2 L_g C_g}{1 - \omega^2 (L_d + L_g) C_g} \tag{B.4}$$

By equating denominator to zero we can find:

$$\omega_r = \frac{1}{\sqrt{(L_d + L_g) C_g}} \tag{B.5}$$

The following equation can be used to obtain the reflection coefficient (Γ) of the plane wave impinging JC-based AMC

$$\Gamma(\omega) = \left[\frac{Z_s(\omega) - \eta_0}{Z_s(\omega) + \eta_0} \right] \tag{B.6}$$

Appendix B (Continued)

From studies and results it can be deduced the phase reflection diagram, which is $\angle\Gamma(\omega)$, is nearly lineal around the resonance. Therefore, we can expand $\angle\Gamma(\omega)$, using Taylor series, just taking into account the first two terms which are linear

$$\Gamma(\omega)|_{around\ \omega_r} = \angle\Gamma(\omega)|_{\omega_r} + (\omega - \omega_r)\frac{d\Gamma(\omega)}{d\omega}\bigg|_{\omega_r} \qquad (B.7)$$

where the first term is always zero for an AMC.

$$\Gamma(\omega)|_{around\ \omega_r} = (\omega - \omega_r)\frac{d\Gamma(\omega)}{d\omega}\bigg|_{\omega_r} \qquad (B.8)$$

Therefore using the following equation can be used to extract the bandwidth (BW)

$$BW = \frac{\omega_2 - \omega_1}{\omega_r} \qquad (B.9)$$

Formula derivation:

$$\Gamma(\omega) = \left[\frac{Z_s(\omega) - \eta_0}{Z_s(\omega) + \eta_0}\right] \qquad (B.10)$$

$$\Gamma(\omega) = \left[\frac{j\omega L_d \frac{1 - \omega^2 L_g C_g}{1 - \omega^2(L_d + L_g)C_g} - \eta_0}{j\omega L_d \frac{1 - \omega^2 L_g C_g}{1 - \omega^2(L_d + L_g)C_g} + \eta_0}\right] \qquad (B.11)$$

$$\Gamma(\omega) = \left[\frac{j\omega L_d(1 - \omega^2 L_g C_g) - \eta_0(1 - \omega^2(L_d + L_g)C_g)}{j\omega L_d(1 - \omega^2 L_g C_g) + \eta_0(1 - \omega^2(L_d + L_g)C_g)}\right] \qquad (B.12)$$

Appendix B (Continued)

Multiplying by its complex conjugate in the numerator and denominator

$$\Gamma(\omega) = \left[\left(\frac{j\omega L_d\left(1 - \omega^2 L_g C_g\right) - \eta_0\left(1 - \omega^2\left(L_d + L_g\right)C_g\right)}{j\omega L_d\left(1 - \omega^2 L_g C_g\right) + \eta_0\left(1 - \omega^2\left(L_d + L_g\right)C_g\right)}\right)\left(\frac{j\omega L_d\left(1 - \omega^2 L_g C_g\right) - \eta_0\left(1 - \omega^2\left(L_d + L_g\right)C_g\right)}{j\omega L_d\left(1 - \omega^2 L_g C_g\right) - \eta_0\left(1 - \omega^2\left(L_d + L_g\right)C_g\right)}\right)\right]$$ (B.13)

$$\Gamma(\omega) = \angle\left[\left\{\frac{\left[\eta_0^2\left(1 - \omega^2\left(L_d + L_g\right)C_g\right)^2 - (\omega L_d)^2\right] - \left[2j\omega L_d\eta_0\left(1 - \omega^2\left(L_d + L_g\right)C_g\right)\right]}{\left(j\omega L_d\left(1 - \omega^2 L_g C_g\right)\right)^2 - \left(\eta_0\left(1 - \omega^2\left(L_d + L_g\right)C_g\right)\right)^2}\right\}\right]$$ (B.14)

The argument of a complex number $x + jy$ is $\tan^{-1}\left(\frac{y}{x}\right)$

$$\Gamma(\omega) = \tan^{-1}\left(\frac{2\omega L_d\eta_0\left(1 - \omega^2\left(L_d + L_g\right)C_g\right)}{\eta_0^2\left(1 - \omega^2\left(L_d + L_g\right)C_g\right)^2 - (\omega L_d)^2}\right)$$ (B.15)

To find $\angle\Gamma(\omega)|_{around\ \omega_r}$ we need use the formula derived before

$$\Gamma(\omega)|_{around\ \omega_r} = (\omega - \omega_r)\frac{d\Gamma(\omega)}{d\omega}\bigg|_{\omega_r}$$ (B.16)

The derivative of the inverse tangent is

$$\frac{d(\tan^{-1}x)}{d\omega} = \frac{1}{1 + x^2}\frac{dx}{d\omega}$$ (B.17)

$$\Gamma(\omega)|_{around\ \omega_r} = (\omega - \omega_r)\left(-4\eta_0 C_g\right)\left(\frac{L_d}{L_d + L_g}\right)^2$$ (B.18)

152

Appendix B (Continued)

If $\pm 45^0$ criterion is used then the bandwidth is

$$-\frac{\pi}{4} = (\omega_1 - \omega_r)(-4\eta_0 C_g)\left(\frac{L_d}{L_d + L_g}\right)^2 \qquad \text{(B.19)}$$

$$\omega_1 = \omega_r - \frac{\pi}{16\eta_0 C_g}\left(\frac{L_d}{L_d + L_g}\right)^2 \qquad \text{(B.20)}$$

$$\frac{\pi}{4} = (\omega_2 - \omega_r)(-4\eta_0 C_g)\left(\frac{L_d}{L_d + L_g}\right)^2 \qquad \text{(B.21)}$$

$$\omega_2 = \omega_r + \frac{\pi}{16\eta_0 C_g}\left(\frac{L_d}{L_d + L_g}\right)^2 \qquad \text{(B.22)}$$

$$BW = \frac{\omega_2 - \omega_1}{\omega_r} \qquad \text{(B.23)}$$

$$BW = \frac{\omega_r + \frac{\pi}{16\eta_0 C_g}\left(\frac{L_d}{L_d + L_g}\right)^2 - \omega_r - \frac{\pi}{16\eta_0 C_g}\left(\frac{L_d}{L_d + L_g}\right)^2}{\frac{1}{\sqrt{(L_d + L_g)C_g}}} \qquad \text{(B.24)}$$

$$BW = \frac{\pi}{8\eta_0}\left(\frac{L_d}{L_d + L_g}\right)^2 \times \frac{\sqrt{(L_d + L_g)C_g}}{C_g} \qquad \text{(B.25)}$$

$$BW = \frac{\pi}{8\eta_0}\sqrt{\frac{(L_d + L_g)}{C_g}} \times \left(\frac{L_d}{L_d + L_g}\right)^2 \qquad \text{(B.26)}$$

If $\pm 90^0$ criterion is used then

$$BW = \frac{\pi}{4\eta_0}\sqrt{\frac{(L_d + L_g)}{C_g}} \times \left(\frac{L_d}{L_d + L_g}\right)^2 \qquad \text{(B.27)}$$

If a superstrate is taken into account then the bandwidth is given by

$$BW = \frac{\pi\sqrt{\varepsilon_r}}{4\eta_0}\sqrt{\frac{(L_d + L_g)}{C_g}} \times \left(\frac{L_d}{L_d + L_g}\right)^2 \qquad \text{(B.28)}$$

153

Appendix C: Quasi-Static Circuit Model for the Tunable Patch

This appendix shows the derivation of the close-form equations for the tunable SP based geometry.
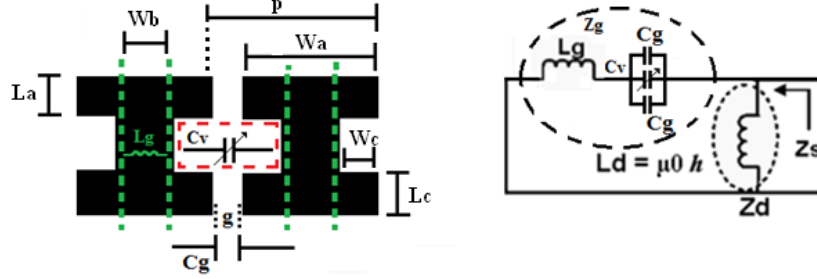

Figure C.1: Equivalent circuit for the self-resonant grid (left) and series combination of the self-resonant grid with the dielectric slab impedance (right) for a tunable unit cell.

$$Z_g = j\omega L_g + \frac{1}{j\omega(2C_g + \hat{C}_v)} \tag{C.1}$$

$$Z_d = j\omega L_d \tag{C.2}$$

$$Z_s(\omega) = Z_g \parallel Z_d \tag{C.3}$$

$$Z_s(\omega) = j\omega L_d \frac{1 - \omega^2 L_g(2C_g + \hat{C}_v)}{1 - \omega^2(L_d + L_g)(2C_g + \hat{C}_v)} \tag{C.4}$$

By equating denominator to zero we can find:

$$\omega_r = \frac{1}{\sqrt{(L_d + L_g)(2C_g + \hat{C}_v)}} \tag{C.5}$$

The following equation can be used to obtain the reflection coefficient (Γ) of the plane wave impinging JC-based AMC

$$\Gamma(\omega) = \left[\frac{Z_s(\omega) - \eta_0}{Z_s(\omega) + \eta_0}\right] \tag{C.6}$$

154

Appendix C (Continued)

From studies and results it can be deduced the phase reflection diagram, which is $\angle\Gamma(\omega)$, is nearly lineal around the resonance. Therefore, we can expand $\angle\Gamma(\omega)$, using Taylor series, just taking into account the first two terms which are linear

$$\Gamma(\omega)|_{around \; \omega_r} = \Gamma(\omega)|_{\omega_r} + (\omega - \omega_r)\frac{d\Gamma(\omega)}{d\omega}\bigg|_{\omega_r} \tag{C.7}$$

where the first term is always zero for an AMC.

$$\Gamma(\omega)|_{around \; \omega_r} = (\omega - \omega_r)\frac{d\Gamma(\omega)}{d\omega}\bigg|_{\omega_r} \tag{C.8}$$

Therefore using the following equation can be used to extract the bandwidth (BW)

$$BW = \frac{\omega_2 - \omega_1}{\omega_r} \tag{C.9}$$

Formula derivation:

$$\Gamma(\omega) = \left[\frac{Z_s(\omega) - \eta_0}{Z_s(\omega) + \eta_0}\right] \tag{C.10}$$

$$\Gamma(\omega) = \left[\frac{j\omega L_d \frac{1-\omega^2 L_g(2C_g+\hat{C}_v)}{1-\omega^2(L_d+L_g)(2C_g+\hat{C}_v)} - \eta_0}{j\omega L_d \frac{1-\omega^2 L_g(2C_g+\hat{C}_v)}{1-\omega^2(L_d+L_g)(2C_g+\hat{C}_v)} + \eta_0}\right] \tag{C.11}$$

$$\Gamma(\omega) = \left[\frac{j\omega L_d\big(1 - \omega^2 L_g(2C_g + \hat{C}_v)\big) - \eta_0\big(1 - \omega^2(L_d + L_g)(2C_g + \hat{C}_v)\big)}{j\omega L_d\big(1 - \omega^2 L_g(2C_g + \hat{C}_v)\big) + \eta_0\big(1 - \omega^2(L_d + L_g)(2C_g + \hat{C}_v)\big)}\right] \tag{C.12}$$

Appendix C (Continued)

Multiplying by its complex conjugate in the numerator and denominator

$$\Gamma(\omega) = [A * B] \tag{C.13}$$

$$A = \left[\left(\frac{j\omega L_d\left(1 - \omega^2 L_g(2C_g + \hat{C}_v)\right) - \eta_0\left(1 - \omega^2(L_d + L_g)(2C_g + \hat{C}_v)\right)}{j\omega L_d\left(1 - \omega^2 L_g(2C_g + \hat{C}_v)\right) + \eta_0\left(1 - \omega^2(L_d + L_g)(2C_g + \hat{C}_v)\right)} \right) \right] \tag{C.14a}$$

$$B = \left[\left(\frac{j\omega L_d\left(1 - \omega^2 L_g(2C_g + \hat{C}_v)\right) - \eta_0\left(1 - \omega^2(L_d + L_g)(2C_g + \hat{C}_v)\right)}{j\omega L_d\left(1 - \omega^2 L_g(2C_g + \hat{C}_v)\right) - \eta_0\left(1 - \omega^2(L_d + L_g)(2C_g + \hat{C}_v)\right)} \right) \right] \tag{C.14b}$$

$$\Gamma(\omega) = \left[\left\{ \frac{\left[\eta_0^2\left(1 - \omega^2(L_d + L_g)(2C_g + \hat{C}_v)\right)^2 - (\omega L_d)^2\right] - \left[2j\omega L_d\eta_0\left(1 - (L_d + L_g)(2C_g + \hat{C}_v)\right)\right]}{\left(j\omega L_d\left(1 - \omega^2 L_g(2C_g + \hat{C}_v)\right)\right)^2 - \left(\eta_0\left(1 - \omega^2(L_d + L_g)(2C_g + \hat{C}_v)\right)\right)^2} \right\} \right] \tag{C.15}$$

The argument of a complex number $x + jy$ is $\tan^{-1}\left(\frac{y}{x}\right)$

$$\Gamma(\omega) = \tan^{-1}\left(\frac{2\omega L_d\eta_0\left(1 - \omega^2(L_d + L_g)(2C_g + \hat{C}_v)\right)}{\eta_0^2\left(1 - \omega^2(L_d + L_g)(2C_g + \hat{C}_v)\right)^2 - (\omega L_d)^2} \right) \tag{C.16}$$

To find $\Gamma(\omega)|_{around\ \omega_r}$ we need use the formula derived before

$$\Gamma(\omega)|_{around\ \omega_r} = (\omega - \omega_r)\frac{d\Gamma(\omega)}{d\omega}\bigg|_{\omega_r} \tag{C.17}$$

The derivative of the inverse tangent is

$$\frac{d(\tan^{-1}x)}{d\omega} = \frac{1}{1 + x^2}\frac{dx}{d\omega} \tag{C.18}$$

$$\Gamma(\omega)|_{around\ \omega_r} = (\omega - \omega_r)\left(-4\eta_0(2C_g + \hat{C}_v)\left(\frac{L_d}{L_d + L_g}\right)^2\right) \tag{C.19}$$

156

Appendix C (Continued)

If $\pm 45^0$ criterion is used then the bandwidth is

$$-\frac{\pi}{4} = (\omega_1 - \omega_r)\left(-4\eta_0(2C_g + \hat{C}_v)\right)\left(\frac{L_d}{L_d + L_g}\right)^2 \tag{C.20}$$

$$\omega_1 = \omega_r - \frac{\pi}{16\eta_0(2C_g + \hat{C}_v)}\left(\frac{L_d}{L_d + L_g}\right)^2 \tag{C.21}$$

$$\frac{\pi}{4} = (\omega_2 - \omega_r)\left(-4\eta_0(2C_g + \hat{C}_v)\right)\left(\frac{L_d}{L_d + L_g}\right)^2 \tag{C.22}$$

$$\omega_2 = \omega_r + \frac{\pi}{16\eta_0(2C_g + \hat{C}_v)}\left(\frac{L_d}{L_d + L_g}\right)^2 \tag{C.23}$$

$$BW = \frac{\omega_2 - \omega_1}{\omega_r} \tag{C.24}$$

$$BW = \frac{\omega_r + \frac{\pi}{16\eta_0(2C_g+\hat{C}_v)}\left(\frac{L_d}{L_d+L_g}\right)^2 - \omega_r - \frac{\pi}{16\eta_0(2C_g+\hat{C}_v)}\left(\frac{L_d}{L_d+L_g}\right)^2}{\frac{1}{\sqrt{(L_d+L_g)C_g}}} \tag{C.25}$$

$$BW = \frac{\pi}{8\eta_0}\left(\frac{L_d}{L_d + L_g}\right)^2 \times \frac{\sqrt{(L_d + L_g)(2C_g + \hat{C}_v)}}{C_g} \tag{C.26}$$

$$BW = \frac{\pi}{8\eta_0}\sqrt{\frac{(L_d + L_g)}{(2C_g + \hat{C}_v)}} \times \left(\frac{L_d}{L_d + L_g}\right)^2 \tag{C.27}$$

If $\pm 90^0$ criterion is used then bandwidth is

$$BW = \frac{\pi}{4\eta_0}\sqrt{\frac{(L_d + L_g)}{(2C_g + \hat{C}_v)}} \times \left(\frac{L_d}{L_d + L_g}\right)^2 \tag{C.28}$$

Appendix C (Continued)

If a superstrate is taken into account then bandwidth is given by

$$BW = \frac{\pi\sqrt{\varepsilon_r}}{4\eta_0}\sqrt{\frac{(L_d + L_g)}{(2C_g + \hat{C}_v)}} \times \left(\frac{L_d}{L_d + L_g}\right)^2 \tag{C.29}$$

Appendix D: Displacement vs. Force Tests on Rigid Boards

Prepared by Dr. Nathan Crane and Ni Qi from the Department of Mechanical Engineering at University of South Florida.

As stated in Chapter 3 and 4 of the dissertation, antenna performance will degrade with decreasing thickness; but the flexibility is inversely related to the same thickness parameter. To increase the flexibility of the antenna without sacrifice the electrical performance, grooved configuration was proposed because of the minimum amount of material removed.

As shown in Figure D.1, twenty grooves were cut across the samples which closely represent the actual set up (3 pieces of Rogers® 6010 and one layer of copper sandwiched in between). All three pieces were bonded using super glue. Groove width, depth and spacing were chosen based on the thickness of a single Rogers® 6010 (1.27mm).
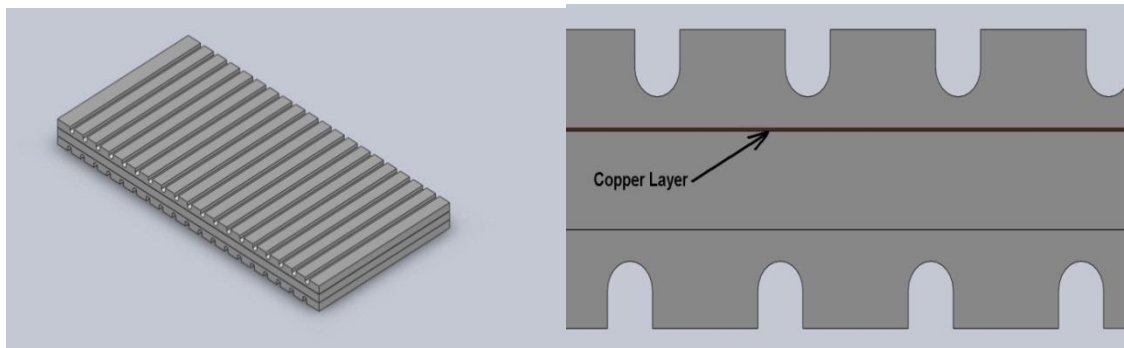
Figure D.1: Illustrations of sample being tested.

- Sample dimension: 50.8 mm x 25.4 mm(2 in x 1 in)

- Thickness: 3.54mm (stacking 3 pieces-1.27mm each)

- Groove dimension: 0.635mm (depth) x 0.762mm (Width)

- Grooves are 2.54mm apart (center to center)

Appendix D (Continued)

Three sets of each non-grooved and grooved sample were tested to compare the stiffness and maximum deflection. All testing were done according to ASTM Standard D-740 (Three force bending). Figure D.2 shows one of the deformed samples after testing.
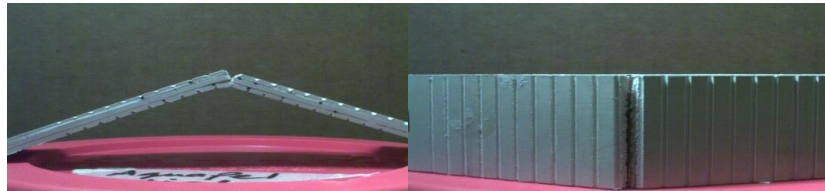

Figure D.2: Grooved sample after testing.

The plot of the displacement versus the force of different boards is shown in Figure D.3 and the results can be interpreted as follows:

- The Linear slope describes the stiffness of the material within the elastic region (no permanent deformation).

- The vertical lines show the maximum deflection the material can sustain before fracture (The outer layer started to have cracks)

Trade-off between the flexibility and the maximum deflection before fracture can be found in the Table D.1.

Table D.1: Stiffness and maximum deflection.

	No Groove	Grooved	(No Groove – Groove) / No Groove (%)
Stiffness(lb/in)	3533	1696	52.00 %
Max Deflection(in)	0.335	0.14	58.2 %

Some important results are:

- Over 50% improvement inflexibility --- less stiff = easier to bend

- Max deflection is reduced by 58% --- less curvature
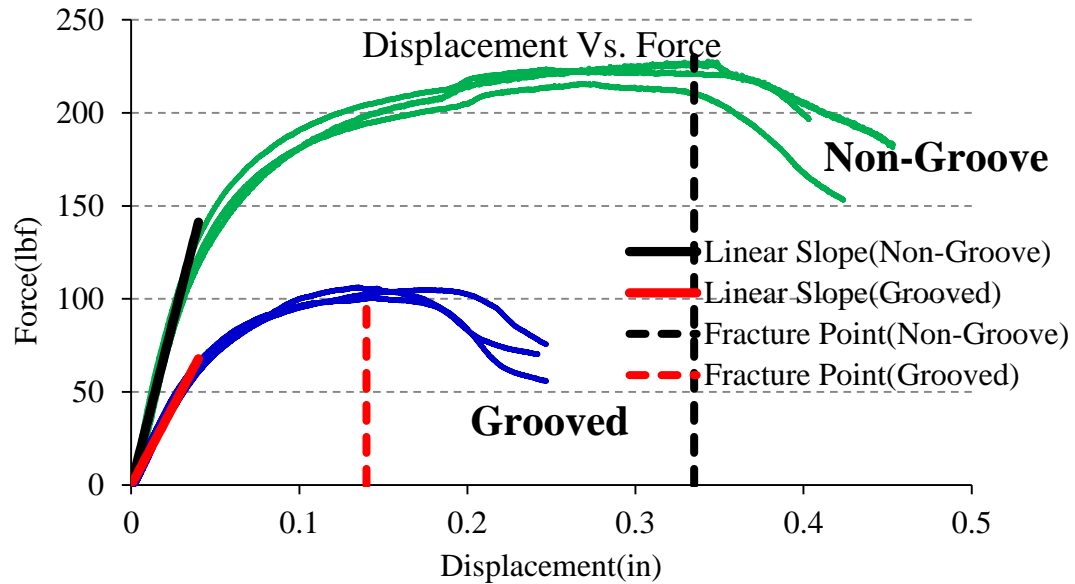
Figure D.3: Data from testing.

The test results indicate that the grooves can decrease the stiffness significantly. However, they also reduce the total deflection that can be achieved. If both low stiffness (ease of bending to desired shape) and large deflection (small radius of curvature) are required, then a different method of increasing the flexibility of the system is required.

However, actual sized antenna will have better results on both the flexibility and maximum deflection due to the width difference.

During testing, the groove gap on the outside closed up because of bending force. It caused the max deflection result to be very poor. If the same ratio (the width of the groove and the width of the sample) are maintained, the width of the groove will increase for prototype (actual antenna is wider). More deflection can be achieved.

Appendix E: Flexural Rigidity Calculations

This appendix shows the calculation of the flexural rigidity of different case scenarios.

Case I: double copper cladding shown in Figure E.1.
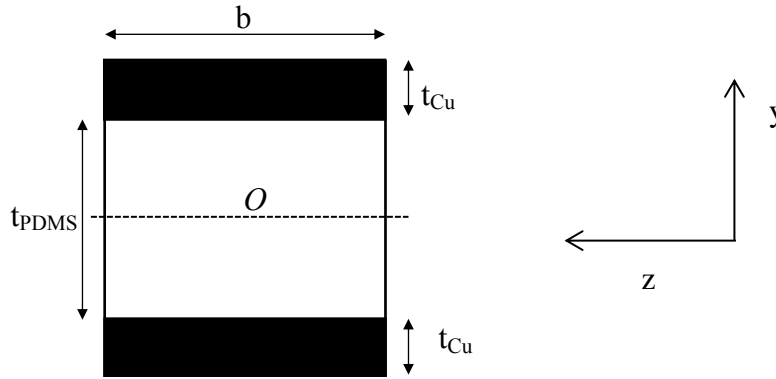
Figure E.1: Rectangular cross section of PDMS based substrate with one metal layer.

The bending stiffness or flexural rigidity of a rectangular cross section is equal to the product of the elastic modulus and the area moment of inertia of the beam cross-section around its neutral axis (E.1) [29].

$$Flexural\ rigidity_{(CASE\ I)} = E_{Cu}\frac{I_{Cu}}{b} + E_{PDMS}\frac{I_{PDMS}}{b} + E_{Cu}\frac{I_{Cu}}{b} \tag{E.1}$$

The elastic modulus of the PDMS and copper used in thes work can be found in [29] and they are estimated to be approximately E_{cu}=1.17 GPa (copper) and E_{PDMS}=800 kPa (PDMS). Thus, the moment of inertia experienced by both materials can be calculated using (E.2) and (E.3).

$$I_{PDMS} = \frac{b(t_{PDMS})^3}{12} \tag{E.2}$$

$$I_{Cu} = \frac{b(t_{Cu})^3}{12} + (bt_{Cu})\left(\frac{t_{PDMS}}{2} + \frac{t_{Cu}}{2}\right)^2 \tag{E.3}$$

162

Replacing (E.2) and (E.3) in (E.1), the flexural rigidity for case I is found (E.5)

$$Flexural\ rigidity_{(CASE\ I)} = E_{PDMS}I_{PDMS} + E_{Cu}I_{Cu} + E_{Cu}I_{Cu} \qquad \text{(E.4)}$$

$$Flexural\ rigidity_{(CASE\ I)} = E_{PDMS}\left[\frac{(t_{PDMS})^3}{12}\right] + 2E_{Cu}\left[\frac{b(t_{Cu})^3}{12} + (bt_{Cu})\left(\frac{t_{PDMS}}{2}+\frac{t_{Cu}}{2}\right)^2\right] \qquad \text{(E.5)}$$
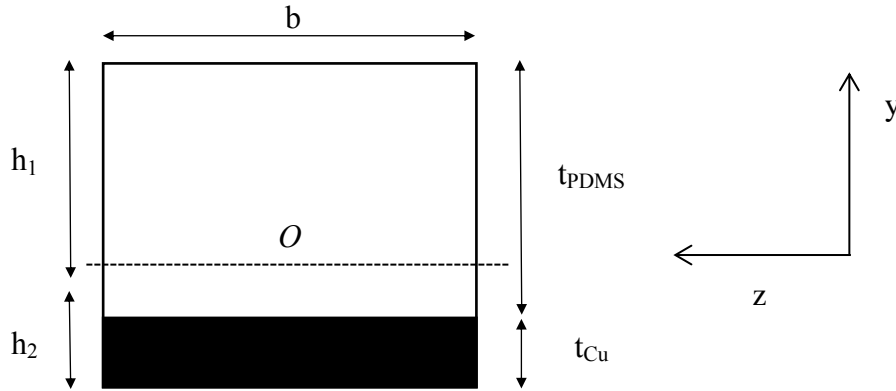
Case 2: copper one copper cladding shown in Figure E.2.

Figure E.2: Rectangular cross section of PDMS based substrate sandwiched between two metal layers.

The flexural rigidity for case II is given by (E.6)

$$Flexural\ rigidity_{(CASE\ II)} = E_{PDMS}\frac{I_{PDMS}}{b} + E_{Cu}\frac{I_{Cu}}{b} \qquad \text{(E.6)}$$

The neutral ax has to be calculated as it is not in the center anymore and the moment of inertia can be calculated using (E.7) and (E.8).

$$I_{PDMS} = \frac{b(t_{PDMS})^3}{12} + (bt_{PDMS})\left(h_1 - \frac{t_{PDMS}}{2}\right)^2 \qquad \text{(E.7)}$$

$$I_{Cu} = \frac{b(t_{Cu})^3}{12} + (bt_{Cu})\left(h_2 - \frac{t_{Cu}}{2}\right)^2 \qquad \text{(E.8)}$$

Appendix E (Continued)

where h_1 and h_2 are the distances from the top and bottom of the composite beam to the neutral axes; y_1 and y_2 represents the y coordinates of the centroids of the respective areas.

$$\int_1 ydA = y_1 A_1 = (h_1 - \frac{t_{PDMS}}{2})(bt_{PDMS}) \tag{E.8}$$

$$\int_2 ydA = y_2 A_2 = -[(t_{PDMS} + t_{Cu}) - h_1](bt_{Cu}) \tag{E.9}$$

Then using the following 2 equations h_1 and h_2 can be found.

$$E_{PDMS} \int_1 ydA + E_{Cu} \int_2 ydA = 0 \tag{E.10}$$

$$h_2 = (t_{PDMS} + t_{Cu}) - h_1 \tag{E.11}$$

Replacing (E.2) and (E.3) in (E.1), the flexural rigidity for case I is found (E.5)

$$Flexural\ rigidity_{(CASE\ I)} = E_{PDMS} I_{PDMS} + E_{Cu} I_{Cu} \tag{E.12}$$

$$F.R._{(CASE\ II)} = E_{PDMS}\left[\frac{(t_{PDMS})^3}{12} + \left\{bt_{PDMS}\left(h_1 - \frac{t_{PDMS}}{2}\right)^2\right\}\right] + E_{Cu}\left[\frac{(t_{Cu})^3}{12} + \left\{bt_{Cu}\left(h_2 - \frac{t_{Cu}}{2}\right)^2\right\}\right] \tag{E.13}$$

Case III: Multilayer triple copper cladding is shown Figure E.3.

The flexural rigidity for case III is given by (E.14), however   this case a transformed section is used (Figure E.3-right) to simplify the problem.

$$Flexural\ rigidity_{(CASE\ III)} = E_{Cu}\frac{I_{Cu}}{b} + E_{PDMS}\frac{I_{PDMS}}{b} + E_{Cu}\frac{I_{Cu}}{b} \tag{E.14}$$

Appendix E (Continued)

The flexural rigidity is given by the elastic modules multiply by the moment of inertia of the transformed section referenced to a material (E.15). Using copper as a reference material:

$$Flexural\ rigidity_{(CASE\ III)} = E_{cu} \sum_{1}^{5} I_i \qquad (E.15)$$

$$n_1 = n_3 = n_5 = \frac{E_{Cu}}{E_{Cu}} \qquad (E.16)$$

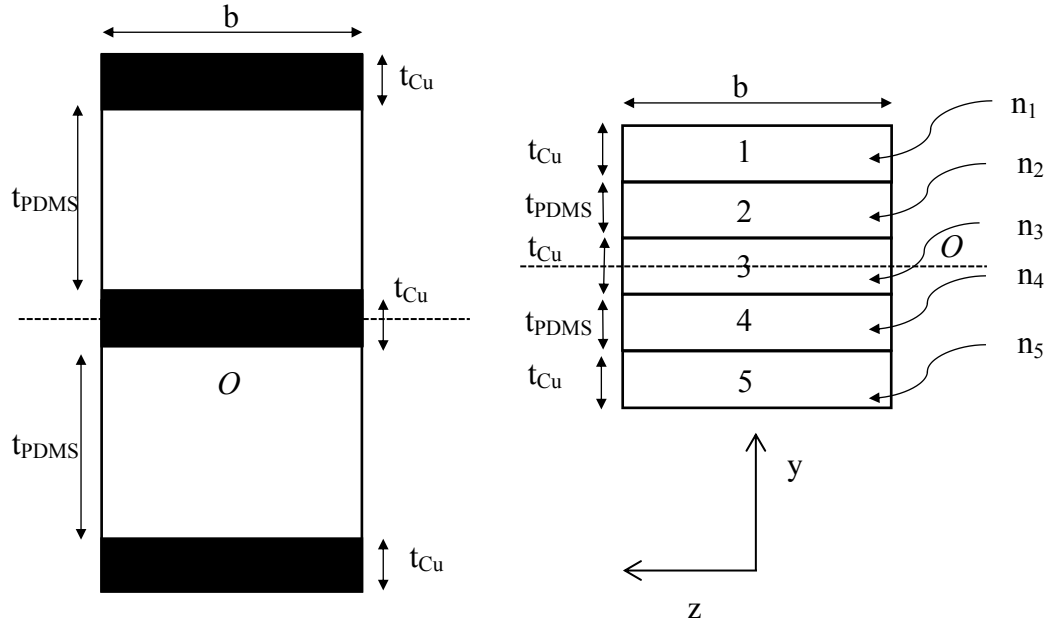$$n_2 = n_4 = \frac{E_{PDMS}}{E_{Cu}} \qquad (E.17)$$

Figure E.3: Rectangular cross section multi-material stack structure (left) and transformed section (right).

The moments of inertia for the transformed sections are:

$$I_1 = I_5 = n_1 \frac{b(t_{Cu})^3}{12} + (bt_{Cu})(t_{PDMS} + t_{Cu})^2 \qquad (E.18)$$

$$I_2 = I_4 = \frac{b(t_{PDMS})^3}{12} + (bt_{PDMS})\left(\frac{t_{PDMS}}{2} + \frac{t_{Cu}}{2}\right)^2 \qquad (E.19)$$

$$I_3 = \frac{b(t_{Cu})^3}{12} \qquad (E.20)$$

Appendix E (Continued)

The flexural rigidity is calculated substituting (E.18), (E.19) and (E.20) in (E15). The calculations for different references are shown in Table E.1.

Table E.1: Flexural rigidity for different references.

Reference	PDMS/metal thickness (mm)	Flexural rigidity (Case I- N·mm)	Flexural rigidity (Case II N·mm)	Flexural rigidity (Case III N·mm)
[38]	0.02/0.015	0.48	1.6×10^{-3}	
[40]	0.02/0.10	51	0.08	
[28]	0.5/0.005	1500	0.7	
[49]	2.5/0.025	7×10^{5}	377	
[48]	2.5/0.025			3×10^{6}

Appendix F: Asymmetric Cells and Defected Ground Structures

In this appendix, the impact of using asymmetric unit cells and defected ground structures (DGS) in a frequency selective surface (FSS) for potential use in low profile antenna applications is analyzed. Figure F1 shows the reflection coefficient phase for a symmetric unit cell with W=8.7 mm (left) and W=7 mm (right). The simulations were performed using Ansoft's High Frequency Structural Simulator (HFSS). Notice that the transverse magnetic (TMz) and transverse electric (TEz) modes both polarized in the x direction have similar phase responses. However, when using an asymmetric unit cell exited by an impinging wave (normal incidence), the reflection coefficient phase is not the same for both modes as shown in Figure F2. Thus, the frequency response of linearly polarized antenna can be shifted depending on the radiator direction with respect to the asymmetric FSS as shown in Figure F3.
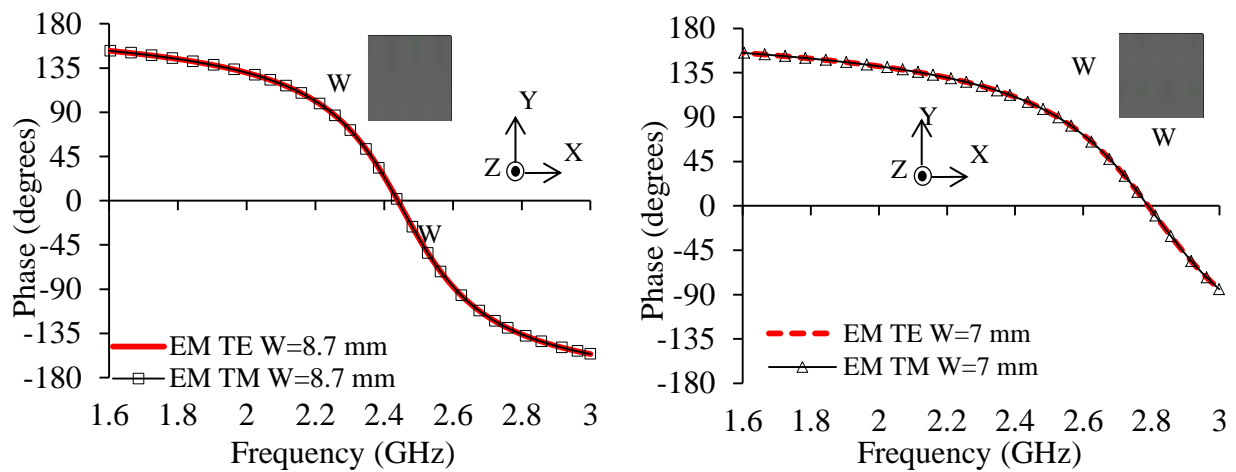
Figure F.1: Simulated reflection coefficient phase for a symmetric unit cell with W=8.7 mm (left) and W=7 mm (right).
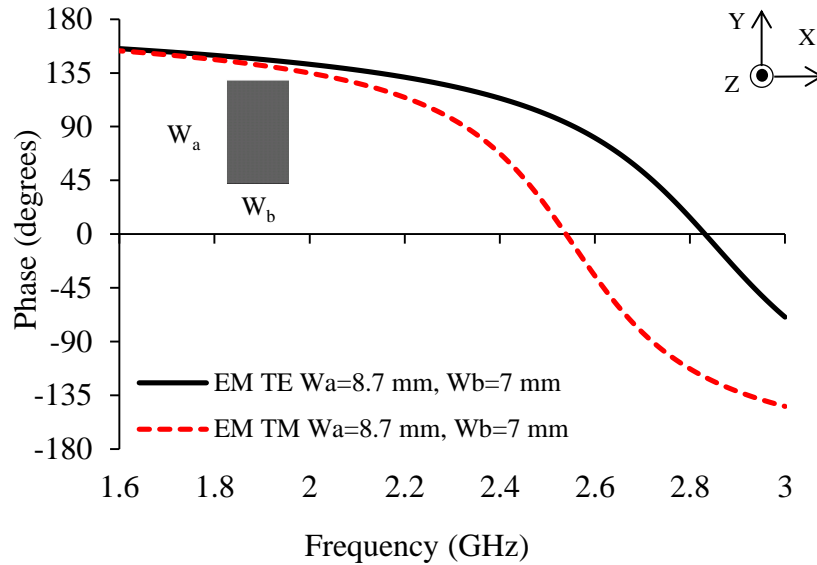
Figure F.2: Simulated reflection coefficient phase for an asymmetric x-oriented unit cell.

To validate and investigate the impact the plane wave simulation results two different antennas were fabricated. These antennas were designed and built (asymmetric 1 and asymmetric 2) using a 2.5 mm-thick Rogers® RT6010 substrate, with a dielectric constant of 10.2, that is supported by the FSS layer of the same thickness and dielectric constant. Design asymmetric 1 uses a square patches (SP) with dimensions W_a =7 mm and W_b = 8.7 mm. Design asymmetric 2 uses a square patches (SP) with dimensions W_a = 8.7 mm and W_b = 7 mm. The dipole and balun were optimized to be within the range of 2 GHz to 3 GHz, and their dimensions were kept the same for both designs. The thicknesses of the dipole and feed layer were 2.5 mm and 1.27 mm, respectively. The resulting total antenna thickness (excluding the feed layer) is ~λ/25. S_{11} in dB for the direction of the dipole's electric field relative to the larger side (W_b=8.7 mm) and to the shorter side (W_b=7 mm) of the unit cell is shown on the left and right side of this figure, respectively.

Wa =7 mm
Wb =8.6 mm
Asymmetric 2

Wa =8.6 mm
Wb =7 mm
Asymmetric 1
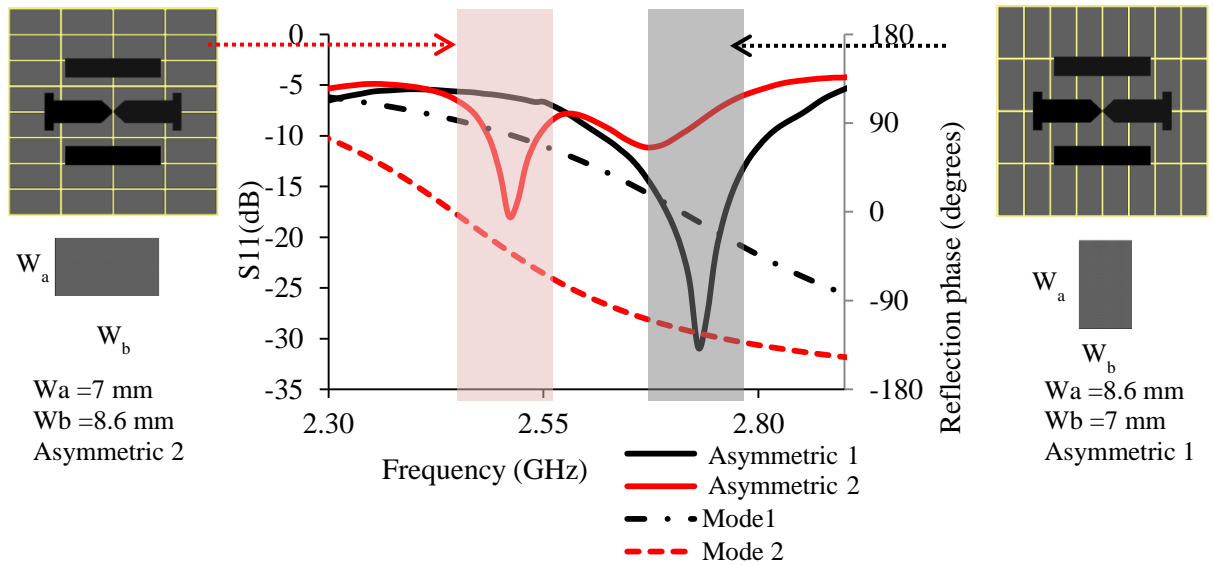
Figure F.3: Measured S_{11} when the ELPOSD is backed by an asymmetric FSS. The asymmetric unit cell has a dimension of 8.6 x 7 mm^2. The simulated coefficient phase responses for asymmetric both unit cell modes are also shown. S_{11} in dB for the direction of the dipole's electric field relative to the larger side (W_b=8.6 mm) and to the shorter side (W_b=7 mm) of the unit cell is shown on the left and right side of this figure, respectively.

Another way of potentially achieving dual, multiband or tunable low profile antennas is by the use of a defected ground structures (DGS). This technique consists on altering the ground plane with a periodic or non-periodic pattern to enhance the performance of a system. This approach has been widely used in microstrip lines, filters, antennas, circuits, etc. [100]-[103]. In the case of the symmetric unit cells without DGS (Figure F1) the reflection coefficient phase of each mode exciting the structure (TM and TE) shows a similar response. In contrast, Figure F4 shows that the reflection coefficient phase and magnitude of a symmetric unit cell using a defected ground structure has different tuning range for TE and TM modes. This type of DGS can be optimized to enhance the magnitude of the reflection coefficient which is marginal for the TM mode. These simulations were performed assuming a 1.27 mm-thick Rogers® RT6010 substrate.
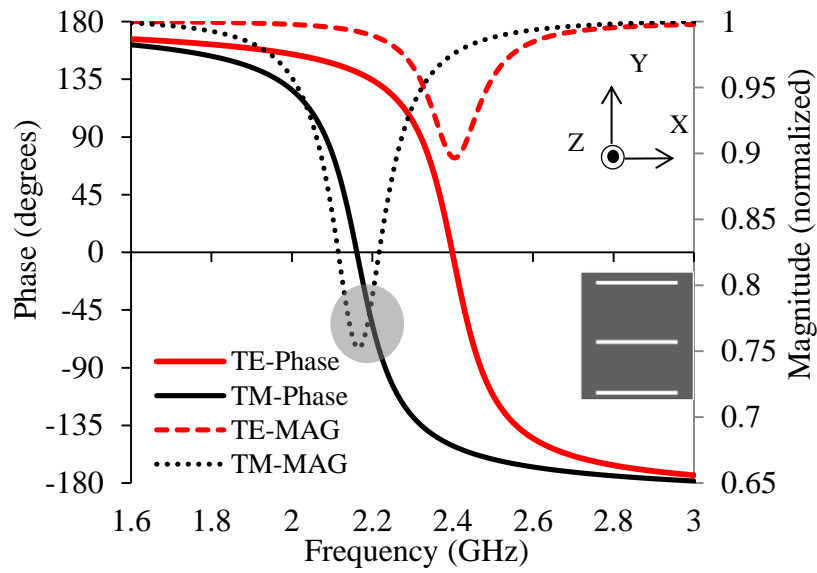
Figure F.4: Simulated reflection coefficient phase and magnitude for a symmetric unit cell using a defected ground structure.

Appendix G: Copyright Permissions

G.1. Permission to Use Figure 2.3 and Figure 2.11

Copyright Clearance Center RightsLink®

Account Info | Help

WILEY

Book: Index
Author: Nader Engheta, Richard W. Ziolkowski
Publisher: John Wiley and Sons
Date: Sep 20, 2006
Copyright © 2006, John Wiley and Sons

Logged in as:
David Cure
Account #:
3000660019

LOGOUT

Order Completed

Thank you very much for your order.

This is a License Agreement between David Cure ("You") and John Wiley and Sons ("John Wiley and Sons") The license consists of your order details, the terms and conditions provided by John Wiley and Sons, and the payment terms and conditions.

License number	Reference confirmation email for license number
License date	May 28, 2013
Licensed content publisher	John Wiley and Sons
Licensed content publication	Wiley oBooks
Licensed content title	Index
Book title	
Licensed copyright line	Copyright © 2006 the Institute of Electrical and Electronics Engineers, Inc.
Licensed content author	Nader Engheta, Richard W. Ziolkowski
Licensed content date	Sep 20, 2006
Start page	403
End page	414
Type of use	Dissertation/Thesis
Requestor type	University/Academic
Format	Electronic
Portion	Figure/table
Number of figures/tables	4
Original Wiley figure/table number(s)	Figure 11.2 and Figure 11.13
Will you be translating?	No
Billing Type	Invoice
Billing address	8132 Silent Creek Dr
	Tampa, FL 336157500
	United States
Total	0.00 USD

CLOSE WINDOW

Appendix G (Continued)

G.2. Permission to Use Figure 2.4

USF

David Cure <dcure@mail.usf.edu>

Copyright persmission

Adam Hirschberg <ahirschberg@cambridge.org>
To: David Cure <dcure@mail.usf.edu>

Fri, May 31, 2013 at 10:41 AM

Dear Mr. Cure,

Thank you for your request. Please note that the Cambridge University
Press permissions policy indicated on our website Permissions pages, allows
a single figure and/or a short extract less than 400 words to be reprinted
from a single Cambridge publication, without the need for a formal
permission request, on the following conditions:

-- the figure must not be credited in our publication to another source; if
so, you must contact the original source for permission

-- you must fully acknowledge the figure, author and Cambridge University
Press publication, and include the copyright notice followed by the phrase
"Reprinted with permission."

Thank you.

Adam

_____
Adam Hirschberg
Rights and Permissions Associate
Cambridge University Press
32 Avenue of the Americas
New York, NY 10013-2473

tel.: 212-337-5088 (direct)
tel.: 212-924-3900 (general)
fax: 212-691-3239 (general)
email: ahirschberg@cambridge.org
web: www.cambridge.org/us
_____

From: David Cure <dcure@mail.usf.edu>
To: ahirschberg@cambridge.org
Date: 05/30/2013 10:02 AM
Subject: Copyright persmission

Dear Adam,

I am currently working on the background theory chapter of my dissertation. I drew one figure myself based on a
book published by Cambridge press. I also used short prose extract (less than 400 words) to explain the basic
concepts of my research. All prose and the figure have been properly referenced on my dissertation. I would like
to request to permission to use this material for copyright purposes.

The book Is and the figure is Figure 3.2 in chapter 3

Electromagnetic Band Gap Structures in Antenna Engineering

				WorldCat
ISBN:	978-0-511-45402-8			
Author/Editor:	Yang, Fan ; Rahmat-Samii, Yahya	**Edition:**	1	
Publication type:	e-Book	**Series:**	The Cambridge RF and Microwave Engineering Series	
Publisher:	Cambridge University Press			
		Country of publication:	United States of America	
Rightsholder:	CAMBRIDGE UNIVERSITY PRESS - US - BOOKS			

--
Thank you very much for you help,

Sincerely,

David Cure

172

Appendix G (Continued)

G.3.   Permission to Use Miscellaneous Material from Previous IEEE Publications

Appendix G (Continued)

G.4.   Permission to Use Add Material as an Appendix D

Permission to add the report you prepared for us to my dissertation   Inbox   x

David Cure <dcure@mail.usf.edu>
to Qi, Nathan

Dear Dr. Crane and Ni Qi,

I need you permission to include the report you prepared for Dr. Weller and I in 2009/2010. This will be an appendix of my dissertation. The document is attached.

The formality is needed for copyright purposes.

Please let me know if is fine with you.

Best regards,

David.

Appendix D.docx
670K   View   Download

Qi Ni
to me

David
Of course---permission granted .... Congratulations!!!

Crane, Nathan
to me, Qi

Fine with me as long as you have the authorship information with it.

From: David Cure [mailto:dcure@mail.usf.edu]
Sent: Thursday, May 23, 2013 1:39 PM
To: Ni, Qi; Crane, Nathan
Subject: Permission to add the report you prepared for us to my dissertation

David Cure <dcure@mail.usf.edu>
to Nathan, Qi

Yes of course. Thanks,

David.

174

ABOUT THE AUTHOR

David Cure received the B.S.in Electronic Engineering department in 2001 at University of Norte, Barranquilla, Colombia, Master in Mobile Communications in 2002 at Polytechnic University of Madrid, Spain and M.S in Electrical Engineering in 2006 at University of South Florida, Tampa, USA. In 2007 he worked as a contractor for Chevroil at Tengiz, Kazakhstan. In 2008 he worked at Triquint Semiconductors. Since 2009 he is Ph.D. student in the Electrical Engineering department at University of South Florida. Of his most notable achievements, he received the Latino Successful award 2011 at USF, HENACC poster competition awards 2010, 2011, 2012, Research USF poster competition awards 2010, 2012 and Honorary mention paper recipient at Antennas and Propagation Conference 2011 and 2012. He was the recipient of a prestigious fellowship from the 2010 NASA Graduate Student Researchers Program (GSRP) and the NACME Alfred P. Sloan Fellowship.